

# Surface Characterization and Biocompatibility of Nanostructured TiNi Alloys Processed by High-Pressure Torsion

Dayangku Noorfazidah Binti AWANG SHRI  
Doctoral Program in Materials Science and Engineering

Submitted to the Graduate School of  
Pure and Applied Sciences  
in Partial Fulfillment of the Requirements  
for the Degree of Doctor of Philosophy in  
Engineering

at the  
University of Tsukuba



*Dedicated to my parents.*



## Acknowledgements

First and foremost, all praise to Allah S.W.T for taught the mankind what they did not know.

I am deeply grateful to my supervisor Prof. Koichi Tsuchiya, for his guidance, vision and support throughout the course of my PhD work. I could not have asked for a better one, his continuous advice and encouragement have been very valuable to me. The dedication and care he provided to me during my PhD are qualities that I hope to be able to carry with me.

I would like to extend my warmest gratitude to Dr Akiko Yamamoto from Biometals Group in National Institute for Materials Science (NIMS) for giving me the opportunity to study biomaterials and corrosion in her lab. Her guidance and constructive comments is proven to be very helpful in order for me to finish this thesis.

I would also like to thank my thesis examiner; Prof Yoshio Sakka and Prof Hee Young Kim for their time and input into this thesis.

Many thanks to members in Microstructure Design Group: Dr. Seiichiro Ii, Dr. Satoshi Emura, Dr. Xiaohua Min, Dr. Alok Singh, and Dr. Julian Rosalie and Yoshimi Toyono for their support during my experiments and encouragement whenever I was in need. My gratitude is also given to my fellow friends: Dr Fanqiang Meng, Baozhen Jiang, Tiantian Li, Haotian Ni, Xuejiao Chen and Ji Xin for making the three years of my life in Tsukuba easier. I also would like to thank members in Biometals Group: Yuko Kohyama, Akemi Kikuta and Noriko Moriguchi.

I am personally indebted to many kind souls during my journey in finishing my PhD here in University of Tsukuba. I wish to express my loving gratitude to my Japanese sister, Mrs Tomomi Utagawa, who has helped me getting through with my life since day one. I would also like to

acknowledge all my close friends that have been supporting me during my study. Thank you Mohd Muzamir Mahat, Ramli Junid, Agnieszka Witecka, Nor Akmal, Livia Lahat, Fauziana, Amir and Gaulthier for being there for me during good and bad time.

Last but not the least; I want to thank my family: my mother Hajah Aishah Abdullah and my father Hj Awang Shri Awang Putra, my brother, Awangku Nazrulddin and my sister, Dayangku Noor Zafirah for their love and support has always been the drive for me to finish my PhD. Thank you for helping me to get to where I am today.

## Table of Contents

<b>Acknowledgements .....</b>	i
<b>List of Figures .....</b>	vii
<b>List of Tables .....</b>	x
<b>Chapter 1 Introduction .....</b>	1
1.1 TiNi Alloys .....	1
1.2 Biomaterials .....	3
1.2.1 Biomaterial and surface interaction .....	4
1.2.2 Protein adsorption.....	5
1.3 Surface Characterization.....	6
1.3.1 Surface characterization.....	6
1.3.2 X-ray Photoelectron Spectroscopy .....	6
1.4 Corrosion in biomaterial.....	8
1.4.1 General concept of corrosion .....	9
1.4.2 Corrosion resistance of TiNi alloys .....	11
1.4.3 Ni ion release.....	12
1.5 Severe plastic deformation.....	12
1.5.1 Equal-channel angular pressing (ECAP) .....	13
1.5.2 Accumulative roll bonding (ARB) .....	13
1.5.3 Multi-directional forging (MDF).....	14
1.5.4 High pressure torsion.....	15

1.5.5	Parameter in estimating the strain in HPT .....	16
1.6	Research objectives .....	18
1.7	Thesis outline .....	18
1.8	References: .....	19

**Chapter 2 Phase Analysis and Mechanical Properties Characterization of TiNi Deformed by High Pressure Torsion .....** 23

2.1	Introduction.....	23
2.2	Experimental Procedures .....	24
2.2.1	Material preparation.....	24
2.2.2	Material characterization.....	24
2.3	Results .....	25
2.3.1	Structural Evolution.....	25
2.3.2	Mechanical properties.....	27
2.4	Discussion.....	27
2.5	Conclusion .....	29
2.6	References .....	30

**Chapter 3 Biocompatibility of Nanostructured TiNi Processed by High-Pressure Torsion ....** 31

3.1	Introduction.....	31
3.2	Experimental Procedures .....	32
3.2.1	Material preparation.....	32
3.2.2	Cell cultures .....	32
3.2.3	Cytocompatibility Evaluation.....	32
3.2.4	Nickel ion release .....	33
3.2.5	Protein adsorption analysis .....	33
3.3	Results .....	35

3.3.1	Colony formation and morphology .....	35
3.3.2	Ni ion release.....	37
3.3.3	Protein adsorption behavior .....	37
3.4	Discussion.....	40
3.4.1	Effect of HPT on the colony formation behavior .....	40
3.4.2	Suppression of Ni ion release by HPT deformation .....	40
3.4.3	Effect of HPT on the protein adsorption behavior.....	41
3.5	Conclusion .....	42
3.7	References: .....	43
<b>Chapter 4</b>	<b>Surface characterization of HPT deformed TiNi alloys .....</b>	<b>45</b>
4.1	Introduction.....	45
4.2	Experimental method .....	46
4.2.1	Sample preparation .....	46
4.2.2	X-ray photoelectron spectroscopy .....	46
4.3	Results .....	47
4.3.1	Surface characterization of Ti-50mol%Ni .....	47
4.3.2	Surface characterization of Ti-50.9mol%Ni .....	59
4.4	Discussion.....	67
4.4.1	Effect of HPT on the surface composition of TiNi.....	67
4.4.2	Effect of HPT on the TiNi passive film formation .....	68
4.4.3	Effect of cell culture to the passive film in TiNi .....	71
4.5	Conclusion .....	71
4.6	References: .....	72

<b>Chapter 5 Electrochemical Characterization of TiNi alloys Deformed by High Pressure Torsion .....</b>	75
5.1    Introduction.....	75
5.2    Experimental Methods.....	76
5.2.1    Sample preparation .....	76
5.2.2    Electrochemical measurements .....	76
5.3    Results .....	77
5.3.1    OCP Measurement.....	77
5.3.2    Polarization curves .....	78
5.4    Discussions .....	81
5.5    Conclusion .....	84
5.6    Reference .....	85
<b>Chapter 6 Conclusions .....</b>	87

## List of Figures

Fig. 1.1 Schematic illustration of the crystal structure of TiNi (a) B2 cubic unit cell of austenite and (b) B19' monoclinic unit cell. ....	1
Fig. 1.2 Schematic representation of the shape memory effect of TiNi alloy [2]. ....	2
Fig. 1.3 Schematic representation of the superelasticity effect of TiNi alloy [2]....	3
Fig. 1.4 Surface properties governing behavior of implanted material [8]. ....	4
Fig. 1.5 Schematic representation of the process of protein adsorption on a solid surface [14]. ....	6
Fig. 1.6 An electron energy diagram for a $\text{Ni}^{2+}$ showing the absorption of a photon and resultant expulsion of a 2p level photoelectron.....	8
Fig. 1.7 Influence of fibroblast on the corrosion of biometallic material [37]. ....	12
Fig. 1.8 Schematic of ECAP process [48] .....	13
Fig. 1.9 Schematic of ARB process [49]. ....	14
Fig. 1.10 Schematic of MDF process [50]. ....	14
Fig. 1.11 Schematic illustration of HPT processing [52].....	16
Fig. 1.12 Parameters used in estimating the total strain in HPT. ....	17
Fig. 2.1 Schematic illustration of microhardness testing along the radial of the sample. ....	24
Fig. 2.2 (a) X-ray diffraction patterns of Ti-50mol%Ni before and after HPT deformation and (b) its corresponding FWHM at $2\theta \sim 42^\circ$ .....	25
Fig. 2.3 (a) X-ray diffraction patterns of Ti-50.9mol%Ni before and after HPT deformation and (b) its corresponding FWHM at $2\theta \sim 42^\circ$ .....	26
Fig. 2.4 Micro-hardness of (a) Ti-50mol%Ni and (b) Ti-50.9mol%Ni before and after deformation with different turns as a function of distance from the disk center. ....	27

Fig. 2.5 Schematic illustration of the nanostructures of HPT deformed TiNi as observed by TEM showing the nanograins (black) and amorphous (gray) region [17].	29
Fig. 3.1 Giemsa-stained samples showing the colony on the Ti-50mol%Ni samples surfaces.	33
Fig. 3.2 SEM images of BHPT Ti-50mol% showing the negative and positive control.	34
Fig. 3.3 Representative image showing colony morphology formed on the surface of (a) BHPT (b) $N = 0.25$ (c) $N = 0.5$ , (d) $N = 1$ , (e) $N = 5$ and (f) $N = 10$ Ti-50mol%Ni samples	36
Fig. 3.4 Representative image showing colony morphology formed on the surface of (a) BHPT (b) $N = 0.25$ (c) $N = 0.5$ , (d) $N = 1$ , (e) $N = 5$ and (f) $N = 10$ Ti-50.9mol%Ni samples	36
Fig. 3.5 Plating efficiency of (a) Ti-50mol%Ni and (b) Ti-50.9mol%Ni.	37
Fig. 3.6 Ni ion release from (a) Ti-50mol% Ni and (b) Ti-50.9mol%Ni as a function of HPT rotation.	38
Fig. 3.7 (a) Albumin and (b) vitronectin adsorption on Ti-50mol%Ni as function of HPT rotation.	39
Fig. 3.8 (a) Albumin and (b) vitronectin adsorption on Ti-50.9mol%Ni as function of HPT rotation.	39
Fig. 4.1 A representative survey XPS spectrum of (a) BHPT Ti-50mol% Ni and (b) BHPT Ti-50.9mol%Ni.	48
Fig. 4.2 Deconvolution of C1s peak on Ti-50mol% BHPT sample.	50
Fig. 4.3 Series of C1s peak of Ti-50mol%Ni (a) before and (b) after cell culture.	51
Fig. 4.4 Deconvoluted spectra of Ti 2p region of Ti-50mol%Ni BHPT sample.	52
Fig. 4.5 Deconvolution spectra of O 1s region of Ti-50mol%Ni BHPT sample.	52
Fig. 4.6 Series of O1s peaks of Ti-50mol%Ni (a) before and (b) after cell culture.	53
Fig. 4.7 Series of Ni 2p peaks of Ti-50mol%Ni (a) before and (b) after cell culture.	54
Fig. 4.8 Ratio of (a) $Ti^{[Me]} / Ti^{[Ox]}$ and (b) $Ni^{[Me]} / Ni^{[Ox]}$ as function of HPT rotation of Ti-50mol%Ni	55
Fig. 4.9 Series of N 1s peaks of Ti-50mol%Ni after cell culture.	57
Fig. 4.10 Depth profile for (a) BHPT, (b) $N = 0.25$ and (c) $N = 0.25$ before cell culture.	58
Fig. 4.11 Depth profile for (a) BHPT, (b) $N = 0.25$ and (c) $N = 0.25$ after cell culture.	58
Fig. 4.12 Series of C 1s peaks of Ti-50.9mol%Ni (a) before and (b) after cell culture.	62
Fig. 4.13 Series of O1s peaks of Ti-50.9mol%Ni (a) before and (b) after cell culture.	63
Fig. 4.14 Series of Ni 2p peaks of Ti-50.9mol%Ni (a) before and (b) after cell culture.	64
Fig. 4.15 Series of N 1s peaks of Ti-50.9mol%Ni after cell culture.	66
Fig. 4.16 Depth profile of Ti-50.9 mol%Ni for (a) BHPT, (b) $N = 0.25$ and (c) $N = 0.25$ before cell culture.	67
Fig. 4.17 Ratio of proportion of the metallic Ni to metallic Ti on the film oxide of Ti-50mol%Ni as the function of HPT rotation.	68
Fig. 4.18 Schematic illustration of passive film formation.	70
Fig. 5.1 Electrochemical cell setup used in this experiment.	77

Fig. 5.2 Open circuit potential of (a) Ti-50mol%Ni and (b) Ti-50.9 mol%Ni in cell culture media.....	79
Fig. 5.3 The potentiodynamic polarization of (a) Ti-50mol%Ni and (b) Ti-50.9 mol%Ni in cell culture media .....	79
Fig. 5.4 Surface morphologies of (a) microcystalline (b) amorphous and (c) nanocrystalline Ti-50.2mol%Ni after corrosion in Hank's solution [10]......	83

## List of Tables

Table 2.1 Degree of torsional deformation with different number of revolutions (edge of sample) .....	27
Table 4.1 Chemical composition of the Ti-50 mol%Ni surface samples as measured by XPS .....	49
Table 4.2 Chemical composition of the Ti-50 mol%Ni surface samples as measured by XPS after cell culture.....	49
Table 4.3 Summary of contribution for each species from Ti-50mol% O1s and C1s spectra before and after cell culture.....	56
Table 4.4 Chemical composition of the Ti-50.9mol%Ni surface samples as measured by XPS .....	60
Table 4.5 Chemical composition of the Ti-50.9mol%Ni surface samples after cell culture as measured by XPS.....	60
Table 4.6 Summary of contribution for each species from Ti-50mol% O1s and C1s spectra before and after cell culture.....	65
Table 5.1 Corrosion parameter of Ti-50mol%Ni .....	80
Table 5.2 Corrosion parameter of Ti-50.9mol%Ni .....	80

## Chapter 1 Introduction

### 1.1 TiNi Alloys

Titanium nickel (TiNi), an intermetallic compound, was discovered by metallurgist Willian J. Buehler at the Naval Ordnance Laboratory. The unique properties of an equiatomic TiNi alloys was discovered when he observed the major change in the atomic structure of the material due to temperature change [1]. The shape memory effect and superelasticity of TiNi alloys is attributed to its ability to exist in two different temperature-dependant phases: austenite and martensite. The high temperature austenite parent phase, stable under low stress is in cubic form with B2 structure. The low temperature martensite phase, stable under suitably higher stress condition, is monoclinic with B19' structure. Fig. 1.1 illustrates the crystal structure of B2 and B19'.

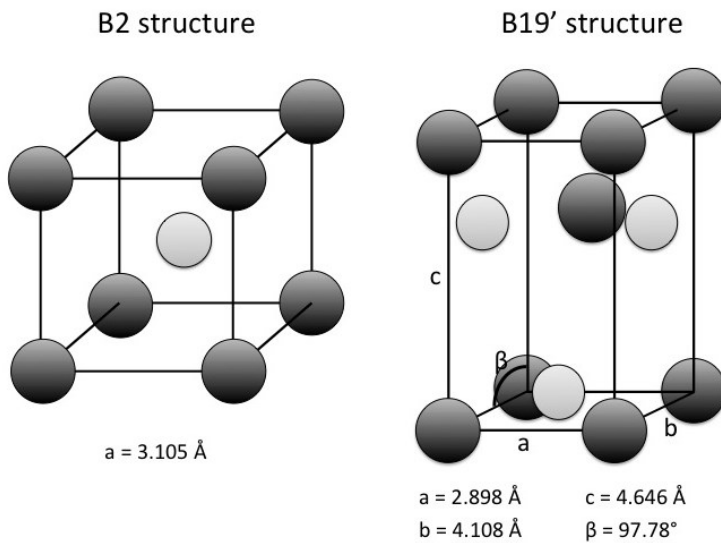


Fig. 1.1 Schematic illustration of the crystal structure of TiNi (a) B2 cubic unit cell of austenite and (b) B19' monoclinic unit cell.

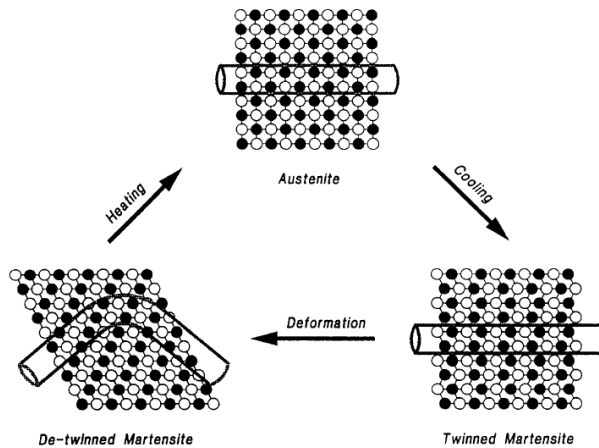


Fig. 1.2 Schematic representation of the shape memory effect of TiNi alloy [2].

The inherent ability of this alloy to alter their type of atomic bonding which causes unique and significant changes in mechanical properties and crystallographic arrangement is termed as superelasticity and shape memory effect. This changes, occurs as results of martensitic transformation, as a function of temperature and stress.

The mechanism of the shape memory effect is described as follows. Upon cooling, the austenite phase starts to transform to martensite at  $M_s$  (martensite start temperature). Since the martensite phase has lower symmetry than the austenite phase, martensites with the same structure but in different crystallographic orientations (called variants of martensite) can be formed. For example, in B2 (cubic) to B19' (monoclinic) transformation of Ni-Ti alloy, as many as 12 correspondence variants can be formed. Formation of martensite in the parent phase will cause a large strain due to the fact that the martensitic transformation is associated with a shape change. A combination of two or four variants may form in tandem to reduce this strain and this particular morphology is called self-accommodation. Variants in this morphology are twin-related to each other. Twins introduced upon martensitic transformation can act as a deformation mode if a stress is applied, since the twin boundary in Ni-Ti is mobile. This process is called detwinning as a favorably oriented variant grows at the expense of other less favorable ones. The deformation remains when the stress is released. Upon heating, the martensite variants revert to their original orientations in the austenite phase so that the original shape is restored. Ordinarily the shape memory effect is one-way as only the shape of the austenite phase is memorized.

Superelasticity at high temperatures is essentially due to a stress-induced martensitic transformation. When the SMA sample is at a temperature above  $M_s$ , in which the austenite phase is the dominant phase in a stress-free specimen, the martensite phase can be induced by application of an outer force. Once the

stress is released, the martensite is unstable at high temperature, thus the reverse transformation happens and the strain is recovered. The high elasticity of NiTi is not simply stretching the atomic bonds, but it is the result of changes in the crystal structure by stress.

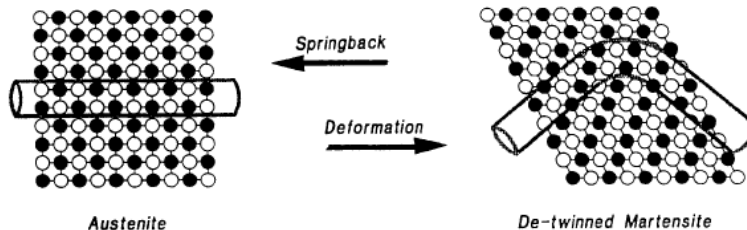


Fig. 1.3 Schematic representation of the superelasticity effect of TiNi alloy [2].

The superelasticity and shape memory effect of TiNi alloys made it one of the common metals used in the biomedical application such as orthodontic archwires, stents and guidewires. Superelasticity of TiNi alloys allows for the use as archwires as it can exert light and constant force on top of good mechanical properties and corrosion resistance [2,3]. For the usage as stent, TiNi stents are self-expanding, taking advantage of their shape memory capabilities. Their superelasticity allows for the delivery of stents to the intervention site without kinking or permanently deforming [4].

## 1.2 Biomaterials

Another consideration in the usage of TiNi alloys as medical devices is its biocompatibility. A biomaterial was defined by American National Institute of Health "as any substance (other than a drug) or combination of substances, synthetic or natural in origin, which can be used for any period of time, as a whole or as a part of a system which treats, augments, or replaces any tissue, organ, or function of the body" [5]. Since this definition excludes application such as orthodontic brackets and surgical instruments, the most appropriate definition for a biomaterials is proposed by D. F William as "material intended to interface with biological system to evaluate, treat, augment or replace any tissue, organ or function of the body" [6].

Biocompatibility is described as "the ability of a material to perform with an appropriate host response in a specific application" [6]. In order for a material to be deemed suitable for biological application, it must be fulfilled several requirements. The materials should be able to perform its biological requirement without causing any cell death, chronic inflammation or other damage of cellular or tissue function [7]. Besides the structural requirement, the biocompatibility also plays a crucial roles as the its surface is directly exposed to the living organism.

### 1.2.1 Biomaterial and surface interaction

The interaction between metal surfaces and tissues is a complex matter. In the long term, metal ions release from the surface and specific biological activity of these metal ions may affect the tissue adjacent to the metal implants. To understand the implication of the metal used as biomaterials, we have to first understand the interaction between biological environments with the material.

The outermost atomic layer of general biomaterial surface at the moment of insertion in to the tissue is a combination of inorganic or organic oxides and hydroxides with low chemical reactivity and low solubility at physiological conditions. Different surfaces possess different basic water chemistries as represented by their elemental compositions and functionalities, such as  $-\text{OH}$ ,  $-\text{CH}_3$ ,  $\text{PO}_4$ ,  $-\text{NH}_2$ ,  $-\text{COOH}$ , and  $-\text{SiOH}$  groups. This chemistry also gives rise to different free surface energies, water-retaining capacities, surface mobility, and other properties that may or may not be important for blood and tissue responses. Fig. 1.4 summarizes a few important surface chemical and physical properties believed to be relevant to in vivo behavior of biomaterials [8].

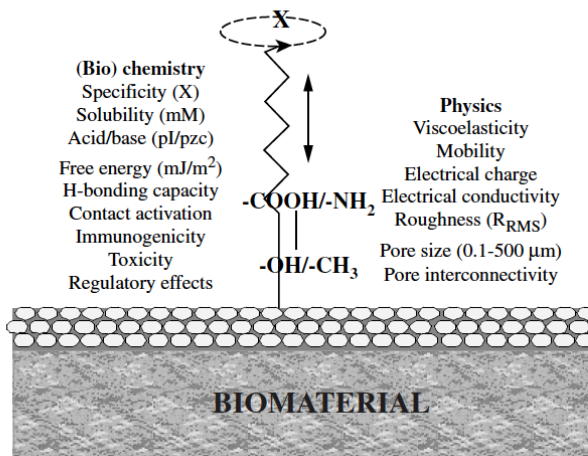


Fig. 1.4 Surface properties governing behavior of implanted material [8].

Biocompatibility of a material surface is closely related to the response of cells in contact with the surface and their adhesion. The initial response to a material placed in a biological environment is the adsorption of the water molecules. The extent and specific manner of interaction of the water molecules with the surface is dependent on the surface properties. These properties also determine the adsorption behavior of protein and other molecules. Within seconds to hours after implantation, adsorbed layer of protein covers the material surface. Then, the cells eventually reach the surface and interact with the surface through the protein layer [9]. Cellular responses are always mediated through proteins *via* their

ligands [10]. The cells can adhere, release active compounds, recruit other cells, grow in size, replicate or die depending on their interaction with the adsorbed protein [11].

### 1.2.2 Protein adsorption

Proteins are essential parts of organisms and involve in many essential processes within cells. Proteins are organic macromolecules built up from 20 different amino acids linked together by peptide bonds. Proteins are responsible for various functions such as forming part of extracellular matrix (ECM) for structural and mechanical support, cell signaling, and immune response and cell adhesion. Protein adsorption is a highly complex process. Protein adsorption can only take place if the Gibbs energy of the system decreases [12,13]. Proteins are surface-active and tend to accumulate at interfaces between the solid surface and liquid. Fig. 1.5 shows the schematic explanation of individual steps involved in the adsorption process of a protein molecule. The process and mechanism of protein adsorption and desorption can be explained as follows:

1. The protein molecules are transported from the solution towards the surface by diffusion and convection, influenced by solid surface electrostatic potential.
2. Protein attachment is driven by the decrease of the Gibbs energy in the system. The attachment of the proteins on the surface is influenced by their amino acid composition, size and their overall physical and chemical properties. The proteins also may change in structure upon adsorption
3. Interaction between the protein and surface might further alter the proteins' structure.
4. Desorption and the diffusion back into the solution might occurs although it is less probable due to high number of interaction points with the surface and a more stable binding after protein unfolding.

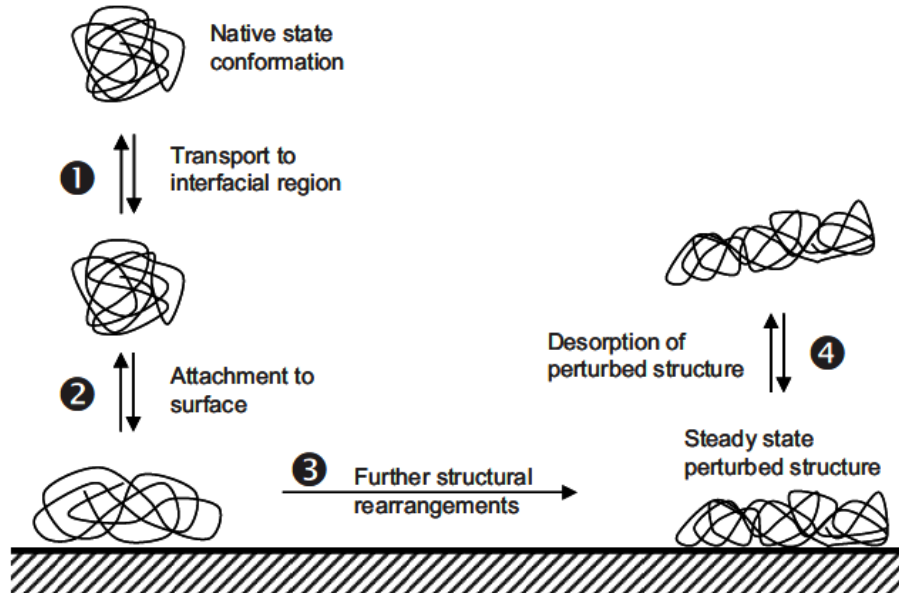


Fig. 1.5 Schematic representation of the process of protein adsorption on a solid surface [14].

Albumin is one of the most popular proteins in the human blood plasma while vitronectin is one of the key proteins for cell attachment onto the substrate surface in vitro cell culture condition. It is reported that albumin adsorption onto a material surface reduces the pro-inflammatory activity of macrophage [15] and platelet-activated thrombogenesis [16]. Vitronectin is a glycoprotein present in plasma mediating cell adhesion to a substrate surface [17] and reorganizing cytoskeleton [18].

### 1.3 Surface Characterization

#### 1.3.1 Surface characterization

Key factors in determining good compatibility between the material and the host tissue are surface wettability, roughness, chemical composition, electric charge and mobility, and corrosion resistance [19]. Atoms on the surface are mostly highly unstable leading to enhanced mobility and higher reactivity. These surface atoms can easily undergo phase transformation, segregation or even dissolution (corrosion). Thus, surface characterization of the biomaterial is important in determining its biocompatibility.

#### 1.3.2 X-ray Photoelectron Spectroscopy

X-ray photoelectron spectroscopy (XPS) is a standard tool used in characterizing the biomedical surface. XPS method is based upon the photoelectric effect in which soft X-rays are used to excite core and valence electrons within the atoms of a surface. As the X-rays are focused upon a sample, the interaction of the X-rays with the atoms in the specimen causes the emission of the core level electron. If

## *Chapter 1*

the X-ray energy is large enough photoelectrons are expelled from the material and their kinetic energies (KE) are measured by the instrument. This excitation process is known as the photoelectric effect and is illustrated in Fig. 1.6. Differences in chemical elements within the near surface region are identified on the basis of their binding energy (BE), which is measured relative to the Fermi level ( $E_{\text{Fermi}}$ ) of the individual atoms. The KE and BE of the photoelectron are related via the following equation:

$$KE = hv - BE - \phi_{\text{spectrometer}} \quad (\text{Eqn. 1.1})$$

where  $hv$  represents the energy of the absorbed photon and  $\phi_{\text{spectrometer}}$  is the work function of the spectrometer.

One of the key features of XPS is that both elemental and chemical information are easily available. This allows XPS to provide information on the oxidation state and local bonding environment of atoms within a surface layer. Due to the high elemental sensitivity of XPS, changes in oxide chemistry can be monitored. The XPS also can be used to differentiate between atoms that have different bonding arrangements to allow for the quantitative analysis of surfaces. Not only that, XPS can be used for depth analysis and as a result, the thickness or structure of oxide overlayer can be visualized.

From the XPS survey spectrum, the elemental concentration of a surface containing two or more elements (except for H and He) can be determined using the following formula:

$$X_A = (I_A/S_A)/(\sum_N(I_N/S_N)) \quad (\text{Eqn. 1.2})$$

where  $X_A$ ,  $I_A$  and  $S_A$  represent the atomic concentration (in at%), the peak area and the relative sensitivity factor (RSF) for element A in a surface having n elements, respectively. Any contributions of the energy loss background to the photoelectron peak intensities are removed using a subtraction algorithm [20].

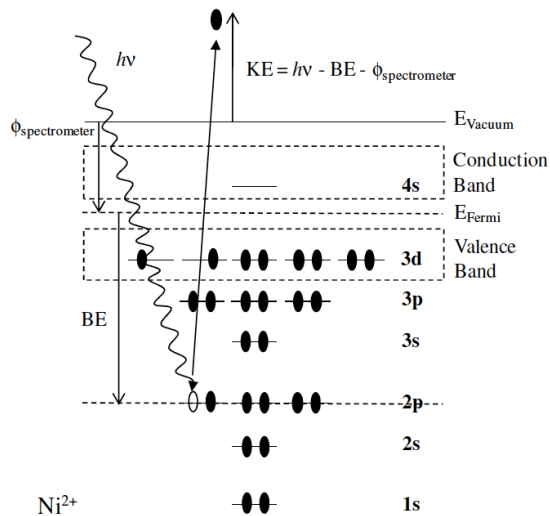


Fig. 1.6 An electron energy diagram for a  $\text{Ni}^{2+}$  showing the absorption of a photon and resultant expulsion of a 2p level photoelectron.

#### 1.4 Corrosion in biomaterial

Medical implants based on metals are mainly used in load bearing application such as joint replacement, for the fixation of bone fracture, or mechanical support for enlarged tubular organs such as arteries vessels in form of screws or stents. Also, metal is widely used in the field of oral surgery. The mechanical properties of metals such as high strength and stiffness allowed for their usage over a long time. The biocompatibility of metal is depending on its good corrosion resistance to avoid impairment of the material properties due to degradation. Corrosion and wear resistance plays a major role as the host tissue may be damaged from the leaking corrosion products or abrasive particles.

Although carcinogenesis by metal prostheses is extremely rare in humans, however there are concerns regarding the possibilities of carcinogenic hazard. Several epidemiological studies have demonstrated the carcinogenicity of several metallic alloys such as nickel, cobalt, chromium or lead compounds. Metal particles produced by mechanical wear or metal ions released by corrosion might be initiating factors for such malignancies [21]. Wear debris is not biologically inert as their accumulation in local tissue is associated with chronic inflammatory reaction, although the nature of which depends on the type or size of the particle [22], concentration and duration of exposure [23], and the surface characteristic of the implants [24].

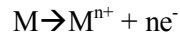
Although metal used as an implant is typically inert due to their good corrosion resistance, the complexity of biological environment might alter their corrosion behavior. Upon insertion into host, these implants encounter different environment with complex physio-chemical nature and their interaction with tissues and body fluid further complicating the corrosion behavior [25]. The corrosion of metallic biomaterials also is a multifactorial factor that depends on the geometric, metallurgic and solution-chemistry parameters [26].

#### 1.4.1 General concept of corrosion

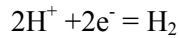
Metal implant corrosion is controlled by (1) the extent of the thermodynamic driving forces which cause corrosion (oxidation/reduction reactions) and (2) physical barriers which limit the kinetics of corrosion [27]. The two parameters will be discussed in detail as below.

##### (1) Thermodynamic consideration on metallic corrosion

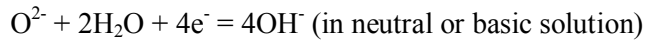
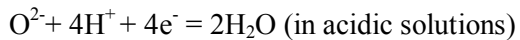
The most relevant form of corrosion related to metallic biomaterials is aqueous corrosion. The electrochemical reaction happens when the metallic biomaterials is exposed to the aqueous electrolyte. Two basic reactions that occur during corrosion are anodic reaction and cathodic reaction. Anodic reaction is the increase of the valence state of the metal atom in which the metal loses electrons during anodic reaction.



In cathodic reaction, the electron is consumed during the reaction. Depending on the nature of the electrolyte, the two most important reactions are the (1) reduction of hydrogen:



and (2) the reduction of dissolved oxygen:



For corrosion to occur, there must be a thermodynamic driving force for the oxidation of metal atoms. This driving force can be quantified thermodynamically using the Gibbs function, or free energy equation (the Gibbs function incorporates both the entropy and enthalpy changes of the above chemical reaction, or the total work to reach equilibrium).

At equilibrium, the chemical energy balances with the electrical energy, which can be quantified using the Nernst equation, which defines the electrical potential across an idealized metal–solution interface when in a solution.

$$E = E_0 + \frac{RT}{nF} \ln \frac{a_{\text{anodic}}}{a_{\text{cathodic}}} \quad (\text{Eqn. 1.3})$$

where  $E_0$  is the standard electrode potential,  $R$  is the gas constant,  $T$  is absolute temperature,  $F$  is the Faraday constant,  $n$  is the number of electrons transferred, and  $a_{\text{anodic}}$  and  $a_{\text{cathodic}}$  is the activities (concentrations) of the anodic and cathodic reactants.

At low concentrations, the activity can be approximated to the concentration. In this situation, there is a net dissolution of the metal and a current will flow. At equilibrium, the rate of the metal dissolution is equal to the rate of the cathodic reaction, and the rate of the reaction is directly proportional to the current density by Faraday's law; therefore:

$$i_{\text{anodic}} = i_{\text{cathodic}} = i_{\text{corrosion}} \quad (\text{Eqn. 1.4})$$

and the Nernst equation can be rewritten:

$$E - E_0 = \pm \beta \ln(i_{\text{corr}}/i_0) \quad (\text{Eqn. 1.5})$$

where  $\beta$  is a constant and  $i_0$  is the exchange current density, which is defined as the anodic (or cathodic) current density at the standard electrode potential. Current density is the current, measured in amperes, normalized to the surface area of the metal.

## (2) Kinetic barrier formation of oxide films

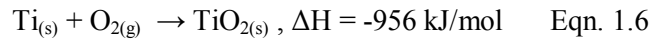
The second primary factor that influences the corrosion process of metallic biomaterials is the formation of stable surface barriers or limitations to the kinetics of corrosion. The barriers prevent corrosion by physically limiting the rate at which oxidation or reduction processes can take place. One example of kinetic limitation to corrosion is the formation of metal oxide passive film on a metal surface. In general, the passive films prevent the migration of metallic ions from the metal to the solutions, the migration of anions from solution to metal, or the migration of electrons across the metal–solution interface[28]. In order to limit oxidation, passive films must have certain characteristics. They must be non-porous and must fully cover the metal surface.

Passivating oxide films spontaneously grow on the surface of metals such as titanium alloys or stainless steels. These oxide films are generally very thin (on the order of 5 to 70 Å) and may be

amorphous or crystalline. One of the more widely accepted models, by Mott and Cabrera [29], states that oxide film growth depends on the electric field across the oxide. The film will change its thickness by growth or dissolution until the rates of both are equal, giving rise to a film thickness that is dependent on metal oxide solution potential. If the interfacial potential is made sufficiently negative or the pH of the solution is made low enough, then these oxide films will no longer be thermodynamically stable and will undergo reductive dissolution, or there will be no driving force for the formation of the oxide, and the metal surface will become unprotected.

#### 1.4.2 Corrosion resistance of TiNi alloys

The biocompatibility of TiNi alloys is derived from the passive titanium oxide ( $\text{TiO}_2$ ) layer on the surface of the alloys. This layer acts as a barrier between the bulk TiNi and the human body. The formation of  $\text{TiO}_2$  in the air is due to the low formation energy of  $\text{TiO}_2$  in comparison to  $\text{NiO}$ . Titanium has a four-fold greater affinity for oxygen than nickel [30]:



As the oxide formation is favored thermodynamically, the passive layer on the TiNi alloys were mainly consists of  $\text{TiO}_2$  despite the high nickel content [31]. The strongly adherent surface layer of 2-10 nm thickness were generally observed [32-34]. Furthermore, the oxide layer is spontaneously regenerated in milliseconds even after damage which is considered as an advantage for the biomedical application of Ti-based alloys [35].

The presence of cells is shown to have a detrimental effect to the protectiveness of the metallic biomaterial passive films. Fig. 1.7 shows a scheme of the effect of the fibroblast on the corrosion behavior of metallic biomaterial. In the study by Hiromoto et. al, they have found that the presence of fibroblasts increases the passive current density and decreases the pitting potential [36]. The pH near the cells was also found to be lower than that of the bulk medium due to the accumulated dissolved metal ions near the cells. The decrease of the pH level of the medium near the cells leading to the initiation of crevice corrosion that will affect the structural integrity of the metallic implant.

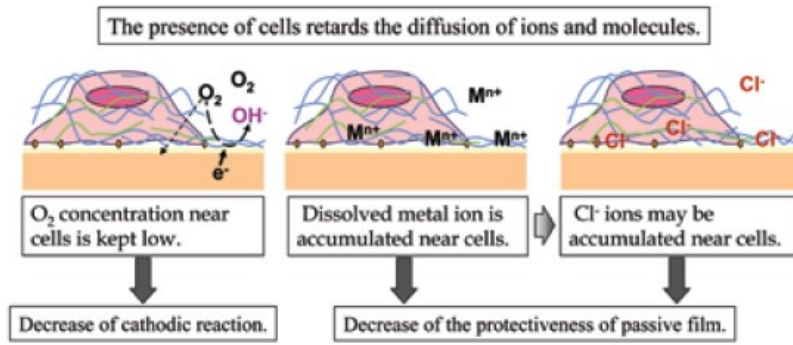


Fig. 1.7 Influence of fibroblast on the corrosion of biometalllic material [37].

#### 1.4.3 Ni ion release

Metal ion release has been often recognized as a cause of clinical failure or allergic reaction of metallic medical devices [38]. Measureable amounts of the metallic ions have been obtained in the tissues surrounding the implants as well as in the serum, body fluids, and urine [39]. For implanted Ni-containing alloys, wide variation in Ni ion release rate has been reported. The rate of Ni release range from 0.81-0.0081 mg/h per kilogram body weight totaling 5-500 mg/y for a 70 kg individual [40]. Ni ion release has been associated with carcinogenic, mutagenic, cytotoxic and allergenic reaction in the average patients [31,41]. The average percentages of metal sensitivity are approximately 10% for the general population, 22% for patients with well-functioning implants, and 60% for the patients with poorly functioning implants [42].

Although TiNi alloys are generally considered as biocompatible, nickel ion release can still be a problem. Presence of Ni within the oxide layer can lead to release of nickel ions into the surrounding media [43]. The formation of the oxide layer may result in the creation of a nickel-rich sublayer which can act as reservoirs of nickel ion release in the body as the nickel atoms are smaller than titanium and oxygen atoms, thus which allows the nickel atom to diffuse interstitially through surface oxide layers [44]. Various studies have been made to modify the surface structure of TiNi alloys to prevent Ni ion release into the surrounding such as by laser surface treatment [45], oxidation [46,47] or chemical passivation [34]. These findings emphasize the importance of controlling the nature and homogeneity of the TiNi oxide films.

#### 1.5 Severe plastic deformation

Bulk nanostructured materials have gaining more interest in recent years due to its improved mechanical properties. Bulk nanostructured metals and alloys by severe plastic deformation have been

seen as new alternative in producing nanocrystalline materials. Previously, in achieving grain refinement in metal and alloys, available techniques are mechanical alloying, inert gas condensation, and electrodeposition. However, in recent years there are growing interests in fabrication of bulk nanostructured materials by using severe plastic deformation (SPD). SPD process is currently defined as “any method of metal forming under an extensive hydrostatic pressure that may be used to impose a very high strain on a bulk solid without the introduction of any significant change in the overall dimensions of the sample and having the ability to produce exceptional grain refinement.”[48].

### 1.5.1 Equal-channel angular pressing (ECAP)

In ECAP processing, a simple shear strain is introduced when the billet passes through the plane where the two channels meet. As the cross section of the billet remains unchanged, the billet can be repetitively go through the pressing, leading to accumulation of very large strain.

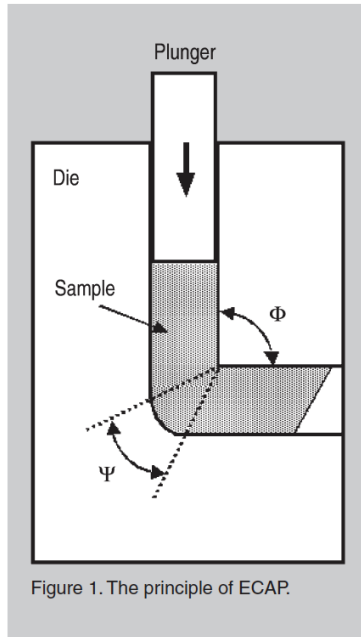


Fig. 1.8 Schematic of ECAP process [48]

### 1.5.2 Accumulative roll bonding (ARB)

In ARB process, the metal sheet is rolled to 50% thickness reduction. Then, the rolled sheet is cut into two and both halves are stacked together, thus restoring the original thickness of the sheet. The stacked sheet then were rolled together to half of the thickness. The repeating of rolling, cutting and stacking ultimately accumulated a large strain in the sheet [49].

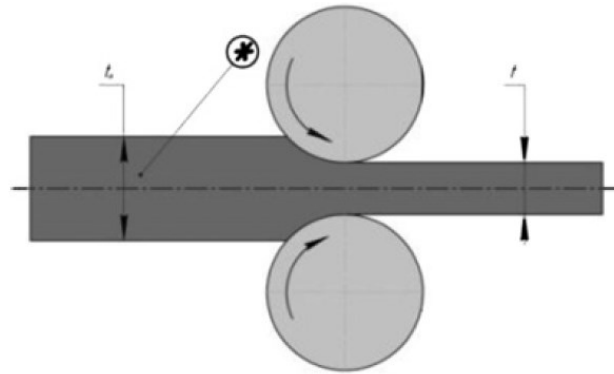


Fig. 1.9 Schematic of ARB process [49].

### 1.5.3 Multi-directional forging (MDF)

The principle of MDF is illustrated in Fig. 1.10 and it assumes multiple repeats of free-forging operations including setting and pulling with changes of the axes of the applied load. Multiple free-forging operations include repeated setting in three orthogonal directions. Since MDF is commonly performed in the temperature interval of  $0.1 - 0.5T_m$ , where  $T_m$  is the melting temperature, grain refinement during MDF is usually associated with dynamic recrystallization [50]. This method can be used to obtain a nanostructured state in rather brittle materials because processing starts at elevated temperatures and the specific loads on tooling are relatively low.

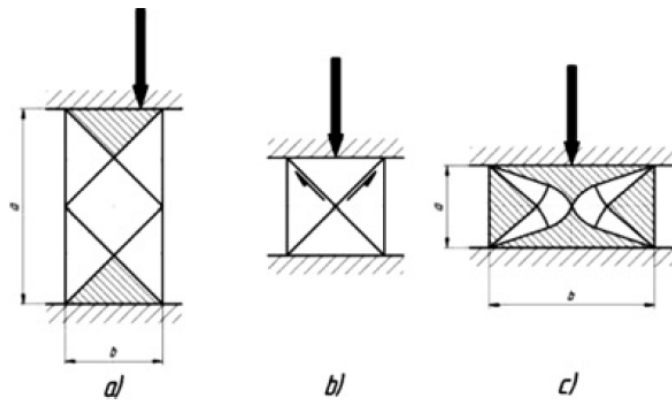


Fig. 1.10 Schematic of MDF process [50].

#### 1.5.4 High pressure torsion

High-pressure torsion (HPT) is one of the SPD methods that have been used to produce bulk amorphous and nanostructured materials. During deformation by HPT, a sample is subjected to shear straining under a high quasi-hydrostatic pressure between two anvils, leading to grain refinement and amorphization of the sample, producing nanostructured material with improved mechanical properties [51]. This technique has a limitation on the dimensions of the samples compared to other SPD technique. However, it may be useful for applications in miniaturized implants or biomedical devices. In this process, the mechanical properties of the materials can be altered by controlling the degree of deformation i.e. the number of rotation.

The principle of HPT processing is depicted schematically in Fig. 1.11. The samples is located between two anvils where it is subjected to compressive applied pressure,  $P$ , of several GPa and simultaneously it is subjected to a torsional strain which is imposed though rotation of the lower anvil. As a result of high imposed pressure, the deforming sample does not break even at high strains. Due to high shear strain imposed on the sample during HPT deformation process, HPT can be used to produced bulk samples with up to nanometer size grains (down to <30nm) which is beneficial to produce small, disc-shaped samples for fundamental studies on nanostructured materials.

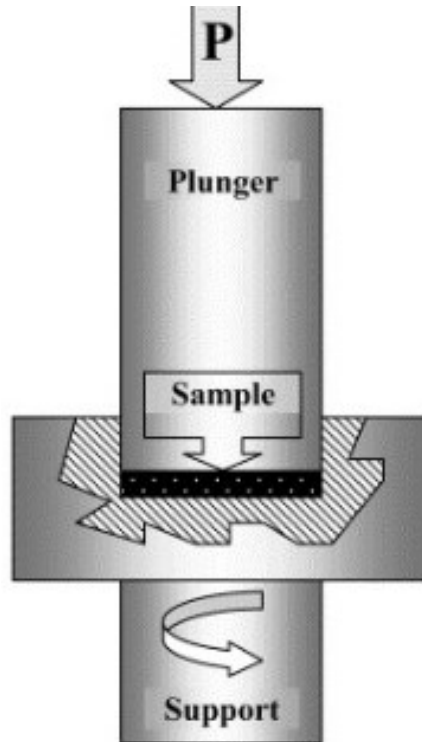


Fig. 1.11 Schematic illustration of HPT processing [52].

### 1.5.5 Parameter in estimating the strain in HPT

In earlier work, there was difficulty in calculation of the precise torsional strain. However, in 1985, a Russian research group applied the principle of HPT to achieve intense deformation in a number of various metallic alloys [53]. The true accumulated strain,  $\varepsilon$ , was estimated by

$$\varepsilon = \ln\left(1 + \frac{\varphi^2 r^2}{h^2}\right) \quad \text{Eqn. 1.8}$$

where the  $\varphi$  is the rotational angle imposed by torsion straining,  $r$  is the radius of the disk and  $h$  is the disk thickness. Since  $\varphi \cdot r/h \gg 1$  and  $\varphi = 2\pi N$  where  $N$  is the number of whole revolutions imposed on the disk, it follows that Eq 1.8 may be written as

$$\varepsilon = \ln\left(\frac{\varphi \cdot r}{h}\right) = \ln\left(\frac{2\pi N \cdot r}{h}\right) \quad \text{Eqn. 1.9}$$

Fig. 1.12 shows the parameters used to estimate the accumulated straining imposed on the sample by HPT deformation.

For an infinitely small rotation,  $d\theta$ , and the displacement,  $dl$  is given by

$$dl = rd\theta \quad (\text{Eqn. 1.10})$$

where the  $r$  is the radius of the disks, and the incremental shear strain,  $d\gamma$ , is given by

$$d\gamma = \frac{dl}{h} = \frac{rd\theta}{h} \quad (\text{Eqn. 1.11})$$

where  $h$  is the disk thickness.

By further assuming that the thickness of the disk is independent of the rotation angle,  $\theta$ , it follows from formal integration that, since  $\theta = 2\pi N$ , the shear strain,  $\gamma$ , is given by

$$\gamma = \frac{2\pi N \cdot r}{h} \quad (\text{Eqn. 1.12})$$

where  $N$  is the rotation number. Finally, in many investigations the equivalent von Mises strain is then calculated using the relationship [81-83]

$$\varepsilon = \frac{\gamma}{\sqrt{3}} = \frac{2\pi N \cdot r}{\sqrt{3}h} \quad (\text{Eqn. 1.13})$$

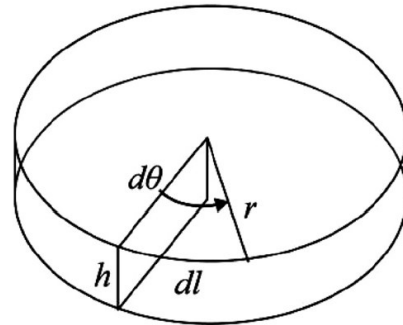


Fig. 1.12 Parameters used in estimating the total strain in HPT.

## **1.6 Research objectives**

In the recent years, nanostructured TiNi alloys produced by severe plastic deformation has garnered attentions due to enhanced mechanical properties [54-57] and corrosion resistance [58,59]. However, not much works has been done on determining the effect of SPD process to the biocompatibility of TiNi alloys. As nanostructured TiNi may be proven beneficial in the usage as biomaterial, it is important to observed the effect of its structural and surface behavior to the stability of TiNi in biological environment. The overall goal of this study is to gain better understanding about the effect of HPT deformation on the phase and microstructural changes, biocompatibility, surface properties and corrosion behavior of the TiNi alloys.

## **1.7 Thesis outline**

In this thesis detailed analysis of the effect of HPT deformation on the phase change, microstructural evolution, surface behavior and biocompatibility of TiNi alloys is presented.

In Chapter 2, detailed XRD and microhardness studies of TiNi alloys before and after HPT deformation are presented. In Chapter 3, the biocompatibility of the TiNi alloys before and after HPT deformation is analyzed. The cell growth behavior and colony morphology is shown to evaluate the impact of HPT to the cell behavior on TiNi alloys. Protein adsorption behavior analysis is also shown for two type of proteins: albumin and vitronectin.

The effect of HPT on the surface chemistry of TiNi alloy before and after cell culture is compared in Chapter 4. Detail analysis focusing on the change in major elements and also the oxide depth profile were done by analyzing the high resolution spectrum obtained from XPS. The electrochemical behavior of TiNi alloys before and after HPT is discussed in Chapter 5. Chapter 6 provides a summary of the results obtained in this work.

## 1.8 References:

- [1] Kauffman GB, Mayo I. The story of nitinol: the serendipitous discovery of the memory metal and its applications. *The Chemical Educator* 1997.
- [2] Thompson SA. An overview of nickel-titanium alloys used in dentistry. *Int Endod J* 2000;33:297–310.
- [3] Gatto E, Matarese G, Di Bella G, Nucera R, Borsellino C, Cordasco G. Load-deflection characteristics of superelastic and thermal nickel-titanium wires. *The European Journal of Orthodontics* 2013;35:115–23.
- [4] Morgan NB. Medical shape memory alloy applications—the market and its products. *Mater. Sci. Eng. A* 2004.
- [5] Clinical applications of biomaterials. National Institutes of Health Consensus Development. *Natl Inst Health Consens Dev Conf Summ* 1983;4:10p.
- [6] Williams DF. The Williams Dictionary of Biomaterials. Liverpool University Press; 1999.
- [7] Williams D. Definitions in Biomaterials. Consensus Conference of the European Society for Biomaterials 1987.
- [8] Ellingsen JE, Lyngstadaas SP. Bio-implant interface: improving biomaterials and tissue reactions 2003.
- [9] Roach P, Eglin D, Rohde K, Perry CC. Modern biomaterials: a review—bulk properties and implications of surface modifications. *Journal of Materials Science: Materials in Medicine* 2007;18:1263–77.
- [10] Yang Y, Cavin R, Ong JL. Protein adsorption on titanium surfaces and their effect on osteoblast attachment. *J. Biomed. Mater. Res.* 2003;67:344–9.
- [11] Ratner BD, Hoffman AS, Schoen FJ, Lemons JE, editors. *Biomaterials Science: An Introduction to Materials in Medicine*. 2nd ed. Elsevier Academic Press; 2004.
- [12] Norde W. Proteins at solid surfaces. *Physical Chemistry of Biological Interfaces* 2000.
- [13] Vermeer A. Conformation of adsorbed proteins. In: Hubbard AT, editor. *Encyclopedia of Surface and Colloid Science*, Usa: Marcel Dekker, Inc; 2002, pp. 1193–212.
- [14] Norde W, Haynes CA. Reversibility and the Mechanism of Protein Adsorption. *ACS Symposium Series*, vol. 602, Washington, DC: American Chemical Society; 2009, pp. 26–40.
- [15] Clarke B, Kingshott P, Hou X, Rochev Y, Gorelov A, Carroll W. Effect of nitinol wire surface properties on albumin adsorption. *Acta Biomater* 2007;3:103–11.
- [16] Martins MCL, Wang D, Ji J, Feng L, Barbosa MA. Albumin and fibrinogen adsorption on PU-PHEMA surfaces. *Biomaterials* 2003;24:2067–76.
- [17] Underwood PA, Bennett FA. A comparison of the biological activities of the cell-adhesive proteins vitronectin and fibronectin. *J. Cell. Sci.* 1989;93 ( Pt 4):641–9.
- [18] Degasne I, Basle MF, Demais V, Hure G, Lesourd M, Grolleau B, Mercier L, Chappard D. Effects of Roughness, Fibronectin and Vitronectin on Attachment, Spreading, and Proliferation of Human Osteoblast-Like Cells (Saos-2) on Titanium Surfaces. *Calcif. Tissue Int.* 1999;64:499–507.
- [19] Bauer S, Schmuki P, Mark von der K, Park J. Engineering biocompatible implant surfaces: Part I: Materials and surfaces. *Prog. Mater. Sci.* 2013.
- [20] Briggs D, Seah MP. Practical surface analysis by Auger and X-ray photoelectron spectroscopy. D. Briggs, & M. P. Seah,(Editors), John Wiley & Sons, Chichester 1983, xiv+ 533; 1983.
- [21] SUNDERMAN F. Carcinogenicity of metal alloys in orthopedic prostheses: Clinical and experimental studies\*1. *Fundamental and Applied Toxicology* 1989;13:205–16.
- [22] Lee JM, Salvati EA, Betts F, DiCarlo EF, Doty SB, Bullough PG. Size of metallic and polyethylene debris particles in failed cemented total hip replacements. *J Bone Joint Surg Br* 1992;74:380–4.
- [23] Howie DW. Tissue response in relation to type of wear particles around failed hip arthroplasties. *The Journal of Arthroplasty* 1990.

- [24] Witt JD, Swann M. Metal wear and tissue response in failed titanium alloy total hip replacements. *J Bone Joint Surg Br* 1991;73:559–63.
- [25] Manivasagam G, Dhinasekaran D, Rajamanickam A. Biomedical Implants: Corrosion and its Prevention-A Review. Recent Patents on Corrosion Science 2010.
- [26] Jacobs JJ, Gilbert JL, Urban RM. Current concepts review. Corrosion of metal orthopaedic implants. *J Bone Joint Surg Am* 1998;80:1554.
- [27] Yaszemski MJ, Trantolo DJ, Lewandrowski K-U, Hasirci V, Altobelli DE, Wise DL, editors. Biomaterials in Orthopedics. CRC Press; 2003.
- [28] Pourbaix M. Electrochemical corrosion of metallic biomaterials. *Biomaterials* 1984;5:122–34.
- [29] Cabrera N, Mott SNF. Theory of the Oxidation of Metals. *Reports on Progress in Physics* 1949;12:163–84.
- [30] Weast RC, Astle MJ, Beyer WH. CRC handbook of chemistry and physics 1988.
- [31] Eliades T, Athanasiou AE. In vivo aging of orthodontic alloys: implications for corrosion potential, nickel release, and biocompatibility. *Angle Orthod* 2002;72:222–37.
- [32] Shabalovskaya SA, Rondelli GC, Undisz AL, Anderegg JW, Burleigh TD, Rettenmayr ME. The electrochemical characteristics of native Nitinol surfaces. *Biomaterials* 2009;30:3662–71.
- [33] Trepanier C, Venugopalan R, Pelton A. Corrosion resistance and biocompatibility of passivated NiTi. In: Yahia LH, editor. Shape memory implants, Shape memory implants. Berlin: Springer; 2000, pp. 35–45.
- [34] Wever DJ, Veldhuizen AG, de Vries J, Busscher HJ, Uges DR, van Horn JR. Electrochemical and surface characterization of a nickel-titanium alloy. *Biomaterials* 1998;19:761–9.
- [35] Fleck C, Eifler D. Corrosion, fatigue and corrosion fatigue behaviour of metal implant materials, especially titanium alloys. *International Journal of Fatigue* 2010;32:929–35.
- [36] Hiromoto S, Hanawa T. Electrochemical properties of 316L stainless steel with culturing L929 fibroblasts. *Journal of the Royal Society Interface* 2005;3:495–505.
- [37] Hiromoto S. Corrosion of metallic biomaterials in cell culture environments. *The Electrochemical Society Interface* 2008;17:41.
- [38] Wapner KL. Implications of metallic corrosion in total knee arthroplasty. *Clin. Orthop. Relat. Res.* 1991;12–20.
- [39] DiCarlo EF, Bullough PG. The biologic responses to orthopedic implants and their wear debris. *Clinical Materials* 1992;9:235–60.
- [40] Black J. Biological Performance of Materials. CRC Press; 2005.
- [41] Lewis CG, Sunderman FW Jr. Metal carcinogenesis in total joint arthroplasty: animal models. *Clinical Orthopaedics and Related ...* 1996.
- [42] Okazaki Y, Gotoh E. Metal release from stainless steel, Co–Cr–Mo–Ni–Fe and Ni–Ti alloys in vascular implants. *Corros. Sci.* 2008;50:3429–38.
- [43] Clarke B, Carroll W, Rochev Y, Hynes M, Bradley D, Plumley D. Influence of Nitinol wire surface treatment on oxide thickness and composition and its subsequent effect on corrosion resistance and nickel ion release. *J. Biomed. Mater. Res.* 2006;79A:61–70.
- [44] Shabalovskaya SA, Tian H, Anderegg JW, Schryvers DU, Carroll WU, Van Humbeeck J. The influence of surface oxides on the distribution and release of nickel from Nitinol wires. *Biomaterials* 2009;30:468–77.
- [45] Cui ZD, Man HC, Yang XJ. The corrosion and nickel release behavior of laser surface-melted NiTi shape memory alloy in Hanks' solution. *Surf. Coat. Tech.* 2005;192:347–53.
- [46] Shabalovskaya S, Anderegg J. Surface spectroscopic characterization of TiNi nearly equiatomic shape memory alloys for implants. *J. Vac. Sci. Technol. A* 1995;13:2624–32.
- [47] Cissé O, Savadogo O, Wu M, Yahia L. Effect of surface treatment of NiTi alloy on its corrosion behavior in Hanks' solution. *J. Biomed. Mater. Res.* 2002;61:339–45.
- [48] Valiev RZ, Estrin Y, Horita Z, Langdon TG, Zechetbauer MJ, Zhu YT. Producing bulk ultrafine-grained materials by severe plastic deformation. *Jom* 2006;58:33–9.
- [49] Lee S-H, Sakai T, Saito Y, Utsunomiya H, Tsuji N. Strengthening of sheath-rolled aluminum

- based MMC by the ARB process. *Mater. Trans. JIM* 1999;40:1422–8.
- [50] Salishchev G, Zaripova R, Galeev R. Nanocrystalline structure formation during severe plastic deformation in metals and their deformation behaviour. *Nanostructured ...* 1995.
- [51] Zhilyaev AP, Langdon TG. Using high-pressure torsion for metal processing: Fundamentals and applications. *Prog. Mater. Sci.* 2008;53:893–979.
- [52] Zhilyaev AP, McNelley TR, Langdon TG. Evolution of microstructure and microtexture in fcc metals during high-pressure torsion. *J Mater Sci* 2006;42:1517–28.
- [53] Kuznetsov RI, Bykov VI, Chernyshov EG, Pilyugin VP, Yefremov NA, Posheyev VV. Plastic deformation of solid bodies under pressure. *Sverdlovsk, IFM UNTS RAN* 1985;4:85.
- [54] Valiev R, Gunderov D, Prokofiev E, Pushin V, Zhu Y. Nanostructuring of TiNi Alloy by SPD Processing for Advanced Properties. *Mater. Trans. JIM* 2008;49:97–101.
- [55] Sergueeva AV, Song C, Valiev RZ, Mukherjee AK. Structure and properties of amorphous and nanocrystalline NiTi prepared by severe plastic deformation and annealing. *Mater. Sci. Eng. A* 2003;339:159–65.
- [56] Tsuchiya K, Inuzuka M, Tomus D, Hosokawa A, Nakayama H, Morii K, Todaka Y, Umemoto M. Martensitic transformation in nanostructured TiNi shape memory alloy formed via severe plastic deformation. *Mater. Sci. Eng. A* 2006;438–440:643–8.
- [57] Tsuchiya K, Hada Y, Koyano T, Nakajima K, Ohnuma M, Koike T, Todaka Y, Umemoto M. Production of TiNi amorphous/nanocrystalline wires with high strength and elastic modulus by severe cold drawing. *Scripta Mater.* 2009;60:749–52.
- [58] Tsuchiya K, Ohnuma M, Nakajima K, Koike T, Hada Y, Todaka Y, Umemoto M. Microstructures and Enhanced Properties of SPD-processed TiNi Shape Memory Alloy. *Mater. Res. Soc. Symp. Proc.* 2009;1129.
- [59] Hu T, Xin YC, Wu SL, Chu CL, Lu J, Guan L, Chen HM, Hung TF, Yeung KWK, Chu PK, Yeung KWK. Corrosion behavior on orthopedic NiTi alloy with nanocrystalline/amorphous surface. *Mater. Chem. Phys.* 2011;126:102–7.



## **Chapter 2 Phase Analysis and Mechanical Properties Characterization of TiNi Deformed by High Pressure Torsion**

### **2.1 Introduction**

TiNi alloys is well known to be susceptible to amorphization and has been observed as results in various techniques such as ball milling [1], cold rolling [2,3], shot peening [4] and cold wire drawing [5]. However, in recent years, many works have been published regarding production of nanostructured TiNi *via* severe plastic deformation (SPD) process [6-9]. During SPD processing, high strain is imposed on the samples leading to introduction of high densities of lattice defects, which is necessary for grain refinement[10].

High-pressure torsion (HPT) is one of the SPD methods that have been used to produce bulk amorphous and nanostructured materials [11]. During deformation by HPT, a sample is subjected to shear straining under a high quasi-hydrostatic pressure between two anvils, leading to grain refinement and amorphization of the sample, producing nanostructured material with improved mechanical properties. Heavy straining imposed during HPT deformation process introduced high dislocation density leading to formation of nanocrystalline and amorphous structure in TiNi alloys.

In this chapter, we examined the effect of HPT deformation on the structural changes and its consequences on the mechanical properties of TiNi alloys.

## 2.2 Experimental Procedures

### 2.2.1 Material preparation

Two kinds of TiNi alloys having composition of Ti-50mol%Ni and Ti-50.9mol%Ni (nominal) were used in this study. The analyzed composition of the ingots was Ti-49.8mol%Ni for Ti-50mol%Ni alloy and Ti-50.8mol%Ni for Ti-50.9mol%Ni alloy. The oxygen content was less than 400 ppm. An ingot was produced by cold-crucible levitation melting. The ingot was forged and hot- and cold-rolled into a plate of about 1 mm thickness. Disk samples with 10 mm in diameter were cut from the plate using a wire electric discharge machine. The disks were heat-treated at 900°C for 1 hour in vacuum and then water quenched at room temperature. They were then ground to a thickness of 0.85 mm. The disks were then subjected to deformation by high-pressure torsion apparatus (REP-HPT-60-05, Riken Enterprise Co. Ltd) under compressive pressure of 5 GPa at room temperature to various number of rotations,  $N = 0.25, 0.5, 1, 5$  and 10 at a rotation speed of 1 rpm. The deformed samples were then mechanically polished on wet metallographic polishing silicon carbide (SiC) papers consecutively from #220 down to #1000, then finished with 9-, 3-, and 1-  $\mu\text{m}$  diamond paste in order to obtain a mirror-like surface. The polished samples were then cleaned ultrasonically for 15 minutes in acetone.

### 2.2.2 Material characterization

X-ray diffraction (XRD) analysis was performed on a diffractometer (MiniFlex2, Rigaku, Co.) operated at 30 kV-15 mA, with Cu-K $\alpha$  for the diffraction angle in the range from 20° to 100°. Micro Vickers (HMV-2, Shimadzu Co.) hardness measurements were done with diamond pyramidal indenter mm with an applied load of 20gf for 15s. The indentation was done across the surface of the disks for 15 points at an interval of 0.5mm, as shown in Fig. 2.1. Forty-five experimental values were determined from each sample. The average value for each distance were then determined as the arithmetic mean.

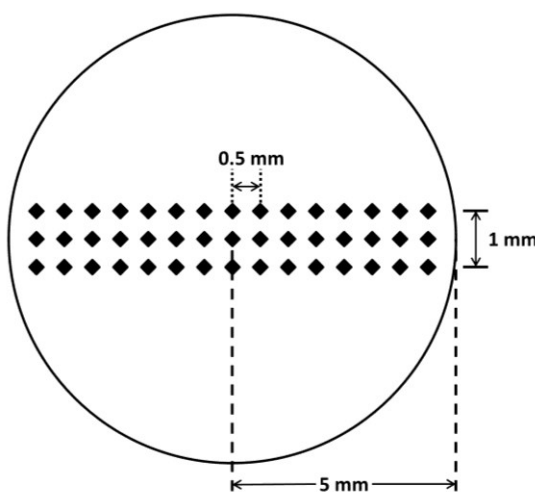


Fig. 2.1 Schematic illustration of microhardness testing along the radial of the sample.

## 2.3 Results

### 2.3.1 Structural Evolution

Fig. 2.2 (a) shows a series of XRD pattern of Ti-50mol%Ni before (BHPT) and after HPT deformation. The XRD pattern of the BHPT sample shows the sample is composed of the austenitic B2 phase and the martensitic B19' phase. However, after subjected to the deformation by HPT at  $N = 0.25$ , significant peak broadening and a decrease in the peak intensity was observed. Further straining ( $N = 0.5$ ) led to the appearance of halo centered at around  $2\theta \sim 42^\circ$ , which corresponds to the formation of amorphous phase. The XRD patterns appear almost unchanged by further straining. Fig. 2.2(b) shows the corresponding full width at half maximum (FWHM) of  $2\theta = 42^\circ$  (corresponding to austenite B2 (110) peak) of TiNi.

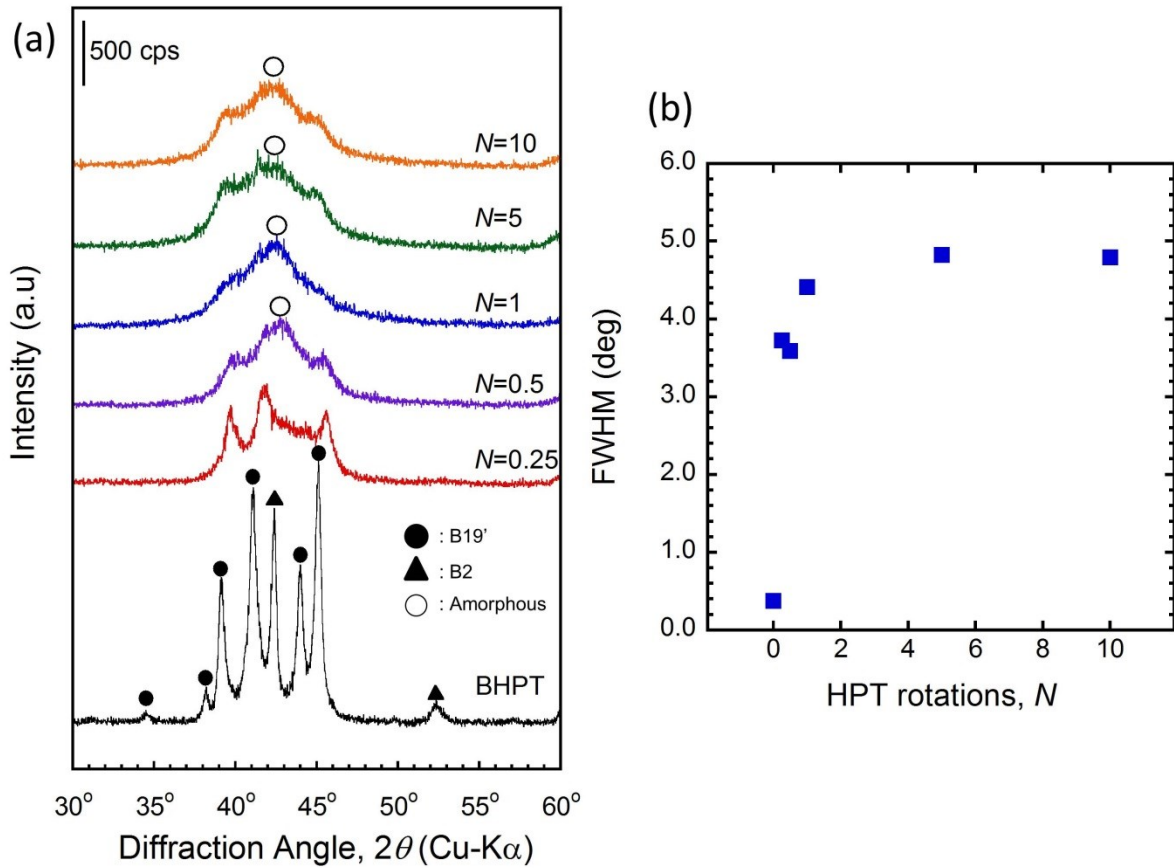


Fig. 2.2 (a) X-ray diffraction patterns of Ti-50mol%Ni before and after HPT deformation and (b) its corresponding FWHM at  $2\theta \sim 42^\circ$ .

XRD patterns for Ti-50.9mol%Ni before and after HPT deformation is shown in Fig. 2.3(a). The XRD pattern of the BHPT sample shows the main peak at  $2\theta \sim 42^\circ$ , corresponding to the (110) austenitic B2

phase. After HPT deformation of  $N = 0.25$ , the peak intensity of (110) decreases and peak broadening was observed. Small peaks seen on the shoulder of the (110) peaks of B2 phase correspond to (002) reflection of B19' martensite phase, which may be due to stress-induced martensitic transformation during HPT deformation. At  $N = 1$ , the intensity of (110) peaks with substantial broadening were observed to be slightly pronounced. Further straining at  $N = 5$  shows the (110) peak is more distinct in comparison to lower number of rotations. The corresponding  $N = 5$  sample's FWHM of  $42^\circ$  shown in Fig. 2.3(b) slightly decreases. This observation may be attributed to the higher fraction of B2 nanograin. Further straining led to a halo centered at  $20 \sim 42^\circ$  which corresponds to the formation of amorphous phase. This observation indicates the grain refinement and phase transformation due to the accumulation of dislocations during HPT deformation.

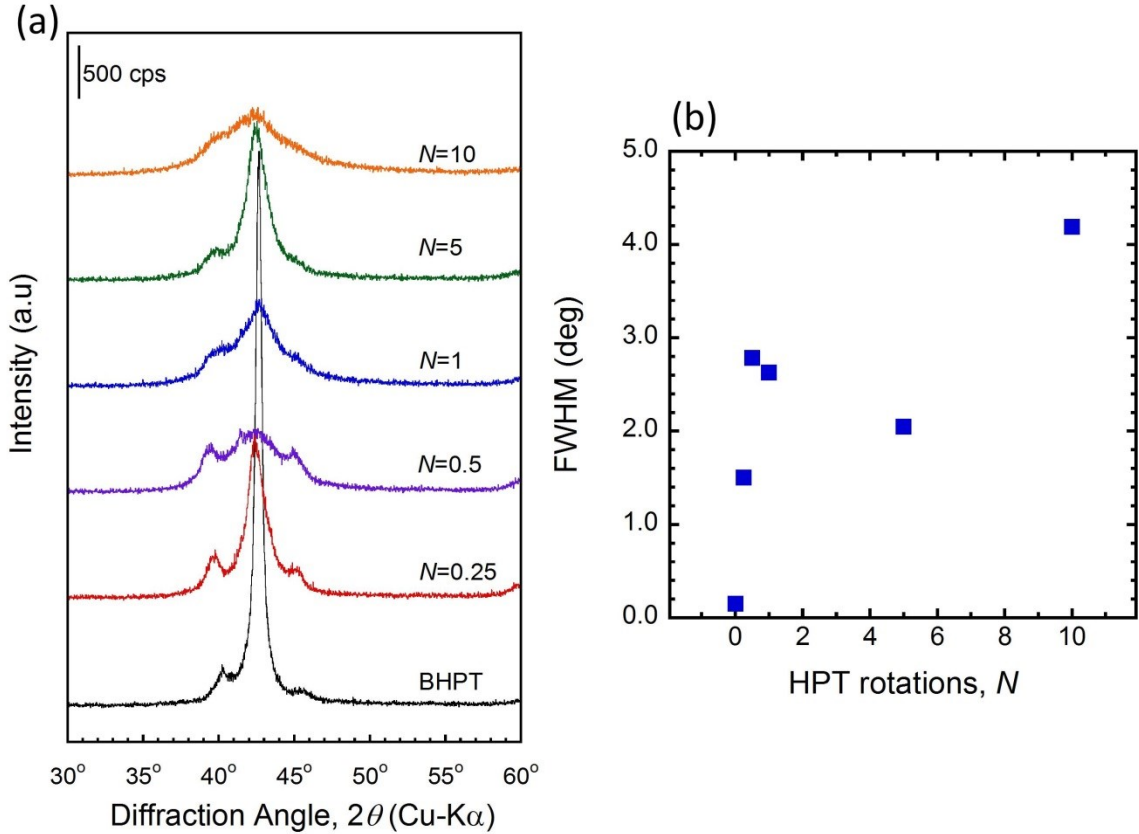


Fig. 2.3 (a) X-ray diffraction patterns of Ti-50.9mol%Ni before and after HPT deformation and (b) its corresponding FWHM at  $20 \sim 42^\circ$ .

### 2.3.2 Mechanical properties

Micro-hardness measurements were done to confirm the change in the structure in the TiNi alloys due to HPT deformation. Fig. 2.4 shows the Vickers micro-hardness as the function of the distance from the disk center. For Ti-50mol%Ni alloys (Fig. 2.4(a)), the hardness of BHPT sample was found to be at 220 Hv. The average hardness of the samples increases two-folds after HPT-deformation of  $N = 0.25$ . At the low number of turns, the edges of the samples possess higher hardness compared to the center of the same disk. Strain hardening caused by HPT increase the hardness in the sample. This is a typical behavior of the materials subjected to HPT processing.

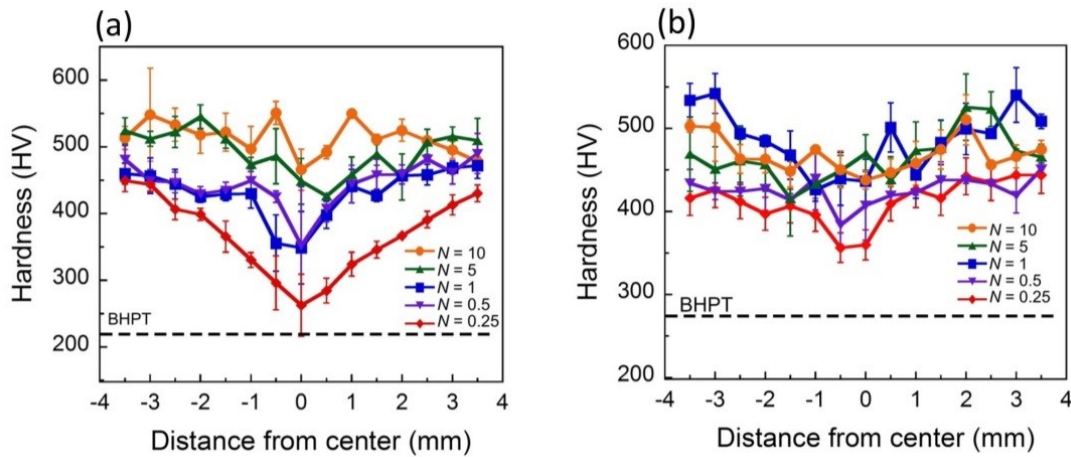


Fig. 2.4 Micro-hardness of (a) Ti-50mol%Ni and (b) Ti-50.9mol%Ni before and after deformation with different turns as a function of distance from the disk center.

## 2.4 Discussion

SPD methods are regarded as attractive processing technique due to its ability to achieve grain refinement in a fully dense, bulk material. In HPT technique, high degree of straining is imposed on the samples. Table 2.1 shows the determined degree of torsional deformation of each samples calculated at the edge of samples based on Eqn 1.2, Eqn 1.5 and Eqn 1.6 as discussed in Section 1.3.

Table 2.1 Degree of torsional deformation with different number of revolutions (edge of sample)

Number of rotation, N	True accumulated strain, $\epsilon$	Shear strain, $\gamma$	Equivalent Von Mises strain, $\epsilon_{\text{equiv}}$
0.25	2.22	9.24	5.33
0.5	2.92	18.48	10.67
1	3.61	36.96	21.34
5	5.22	184.80	106.69
10	5.91	369.60	213.39

The large strain imposed leads to the phase changes as observed in Fig. 2.2 and Fig. 2.3 for Ti-50mol%Ni and Ti-50.9mol%Ni, respectively. The only stark difference between this two alloys is the initial austenitic B2 phase of Ti-50.9 mol% Ni is more stable and less susceptible to amorphization. The tendency to form the amorphous structure under HPT conditions is at the strongest when the samples were in stable martensitic state [12]. This is due to relatively higher degree of imperfection on the crystal lattice if slightly Ni-rich Ti-50.9 mol% Ni [12].

The phase transformation observed from XRD pattern can be summarized as follows. When subjected to a low number of rotation ( $N = 0.25$  and  $0.5$ ), decrease in B2 intensity and emergence of B19' martensite peaks indicate the deformation-induced martensitic transformation. The original B2 austenite is transformed into self-accommodated martensite with various variants. With further deformation, the martensites are subjected to reorientation and turn into same orientation in a definite grain. When the deformation increases, the high density of dislocation lead to formation of dislocation cell in the grain, forming a nanocrystalline grains. Peak broadening on XRD suggests the mixed subgrain formation of B2 and B19' [13]. Decreasing grain size with further deformation stabilized the B2 austenite and suppressed the martensitic deformation [14]. This translated into a slightly increased in peak intensity and reduced FWHM value at  $2\theta \sim 42^\circ$  of  $N = 5$  sample of Ti-50.9mol%Ni indicating increased in amount of B2 nanocrystal. With further deformation, the B19' martensite transforms into the fragmented grain [13]. Further rotation at  $N = 10$  finally produced amorphous structure with embedded nano-scale debris of B2 phase. After subjected to large plastic strain, high density of defects were induced and destroy the periodicity of the atomic arrangement, thus leads to the formation of amorphous phase amongst the retained nanocrystalline grains[15].

This results agrees with previous TEM observations of HPT-deformed TiNi [3,7,8,16]. It should be emphasized that the amorphization is very heterogeneous process [6]. Preferential sites for amorphization may be dislocation tangles, martensite twin boundaries and grain boundaries. Amorphization in the form of shear bands was also observed as shown in Fig. 2.5 [17].

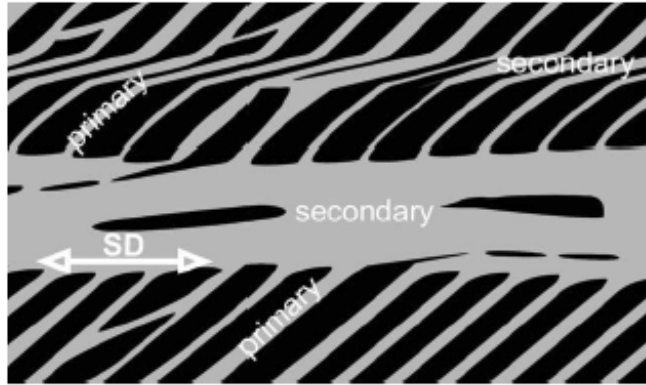


Fig. 2.5 Schematic illustration of the nanostructures of HPT deformed TiNi as observed by TEM showing the nanograins (black) and amorphous (gray)region [17].

One of the drawbacks in HPT is that the variation of the imposed strain across the radial distance as shown in the hardness profile in Fig. 2.4. Inspection of Eqn. 1.12 suggests that processing by HPT will introduce a very significant inhomogeneity into the material, so that both the microstructure will be extremely inhomogeneous. However, this study demonstrated a gradual evolution towards a homogeneous structure in the HPT deformed samples with this evolution occurring by increasing the total number of rotations. In both TiNi alloys, at low rotation, lower hardness is observed in the central region of the disk. However, the hardness values in the centers gradually increase with increasing  $N$ . As the rotational number increases, the hardness becomes more homogeneous across the disks due to excessive strain accumulation introduced by extra rotation [3]. The hardness difference between the center and the edge tends to become relatively small as the number of rotation increases resulting in the overall increase in the micro hardness level. This result confirms the development of a gradual evolution in hardness across the disk diameters with increasing torsional straining.

## 2.5 Conclusion

In this chapter, we have demonstrated the gradual changes in structural and mechanical properties of TiNi alloys after subjected to HPT at various number of rotations. The study on the X-ray diffraction and microhardness of TiNi alloys after subjected to HPT deformation systematically confirms the change in the microstructure and mechanical properties. XRD patterns examination revealed that phase transformation from martensite to austenitic occurs in both TiNi alloys, with martensite suppression due to grain refinement. Microhardness characterization shows an evolution towards hardness homogeneity with increasing numbers of turns in HPT processing.

## 2.6 References

- [1] Yamada K, Koch CC. The influence of mill energy and temperature on the structure of the TiNi intermetallic after mechanical attrition. *J. Mater. Res.* 1993;8:1317–26.
- [2] Koike J, Parkin D, Nastasi M. Crystal-to-amorphous transformation of NiTi induced by cold rolling. *J. Mater. Res.* 1990;5:1414–8.
- [3] Tsuchiya K, Inuzuka M, Tomus D, Hosokawa A, Nakayama H, Morii K, Todaka Y, Umemoto M. Martensitic transformation in nanostructured TiNi shape memory alloy formed via severe plastic deformation. *Mater. Sci. Eng. A* 2006;438–440:643–8.
- [4] Green S, Grant D, Wood J. XPS characterisation of surface modified Ni-Ti shape memory alloy. *Mater. Sci. Eng. A* 1997;224:21–6.
- [5] Tsuchiya K, Hada Y, Koyano T, Nakajima K, Ohnuma M, Koike T, Todaka Y, Umemoto M. Production of TiNi amorphous/nanocrystalline wires with high strength and elastic modulus by severe cold drawing. *Scripta Mater.* 2009;60:749–52.
- [6] Sergueeva AV, Song C, Valiev RZ, Mukherjee AK. Structure and properties of amorphous and nanocrystalline NiTi prepared by severe plastic deformation and annealing. *Mater. Sci. Eng. A* 2003;339:159–65.
- [7] Tsuchiya K, Cao QF, Hosokawa A, Katahira M, Todaka Y, Umemoto M. Nanostructured Shape Memory Alloys for Biomedical Applications. *Mater. Sci. Forum* 2007;539–543:505–10.
- [8] Peterlechner M, Waitz T, Karnthaler HP. Nanocrystallization of NiTi shape memory alloys made amorphous by high-pressure torsion. *Scripta Mater.* 2008;59:566–9.
- [9] Mahesh KK, Braz Fernandes FM, Gurau G. Phase Transformation in Ni-Ti Shape Memory and Superelastic Alloys Subjected to High Pressure Torsion. *Amr* 2010;123–125:1007–10.
- [10] Valiev RZ, Estrin Y, Horita Z, Langdon TG, Zechetbauer MJ, Zhu YT. Producing bulk ultrafine-grained materials by severe plastic deformation. *Jom* 2006;58:33–9.
- [11] Zhilyaev AP, Langdon TG. Using high-pressure torsion for metal processing: Fundamentals and applications. *Prog. Mater. Sci.* 2008;53:893–979.
- [12] Prokoshkin SD, Khmelevskaya IY, Dobatkin SV, Trubitsyna IB, Tatyannin EV, Stolyarov VV, Prokofiev EA. Alloy composition, deformation temperature, pressure and post-deformation annealing effects in severely deformed Ti–Ni based shape memory alloys. *Acta Mater.* 2005;53:2703–14.
- [13] Pushin VG, Valiev RZ, Valiev EZ, Kourov NI, Kuranova NN, Makarov VV, Pushin AV, Uksusnikov AN. Phase and structural transformations in the Ti49.5Ni50.5 alloy with a shape-memory effect during torsion under high pressure. *Phys. Metals Metallogr.* 2012;113:256–70.
- [14] Waitz T, Kazykhanov V, Karnthaler HP. Martensitic phase transformations in nanocrystalline NiTi studied by TEM. *Acta Mater.* 2004;52:137–47.
- [15] Zhang Y, Jiang S, Hu L, Liang Y. Deformation mechanism of NiTi shape memory alloy subjected to severe plastic deformation at low temperature. *Mater. Sci. Eng. A* 2012.
- [16] Tsuchiya K, Ohnuma M, Nakajima K, Koike T, Hada Y, Todaka Y, Umemoto M. Microstructures and Enhanced Properties of SPD-processed TiNi Shape Memory Alloy. *Mater. Res. Soc. Symp. Proc.* 2009;1129.
- [17] Peterlechner M, Waitz T, Karnthaler HP. Nanoscale amorphization of severely deformed NiTi shape memory alloys. *Scripta Mater.* 2009;60:1137–40.

## **Chapter 3 Biocompatibility of Nanostructured TiNi Processed by High-Pressure Torsion**

### **3.1 Introduction**

Surface chemistry plays an important role in determining the stability of a metal *in vitro* and *in vivo*, which influences its biocompatibility via protein adsorption behavior and following cell attachment[1]. For metallic materials currently used in the biomedical field such as TiNi, titanium alloys and stainless steel, their biocompatibility is heavily dependent on the stable formation of a protective oxide layer on their surfaces. *In vitro* testing on a mechanically polished TiNi sample reveals a high amount of Ni ion release from it due to the metallic Ni existing on its surface [2]. Thus, various researches have been done on surface modification process of TiNi alloys, focusing on the increase in the thickness of the oxide layer via heat treatment [3,4], chemical modification [2,5] or ion implantation [6,7]. Although thicker oxide layer has been shown beneficial in preventing harmful Ni ion release, it has a problem with mechanical stability especially when it undergoes pseudo-elastic transformation [8,9]. Various surface modification processes such as oxidation and coating have also been proven beneficial to improve the biocompatibility of TiNi alloys. However, emergence of miniature devices such as guide wires and pneumatic valves (in cardiovascular application) makes bare TiNi alloys still an attractive option for such application from the viewpoint of process and cost reduction. Thus, the processing of bare TiNi alloys is crucial to ensure their stability for long term use.

In this chapter, we investigated the effect of HPT deformation on biocompatibility of TiNi alloys by examining their cytocompatibility, protein adsorption behavior and Ni ion release.

## 3.2 Experimental Procedures

### 3.2.1 Material preparation

The samples were prepared and polished as described in Section 2.2.1. The polished samples were then cleaned ultrasonically for 15 min in acetone. The sample disks were sterilized using ethylene oxide gas (EOG) for 23 hrs. at 44 °C.

### 3.2.2 Cell cultures

The cells used in this study was murine fibroblast L929. The L929 were maintained in Eagle's minimal essential medium (Nissui Pharmaceutical Co., Ltd, Japan) supplemented with 10% (v/v) fetal bovine serum (FBS), abbreviated as EMEM+FBS. The supplemented essential cell culture medium is henceforth referred to as "cell culture medium". L929 were cultured in cell culture medium at 37°C under 5% CO<sub>2</sub> in a humidified air incubator prior to use. The cells were grown in a 25 cm<sup>2</sup> cell culture flask. Prior to cell passage, the cell culture medium in the flask was discarded and the cells were washed once with sterile phosphate buffered saline. Cell were then exposed to trypsin solution and incubated at 37°C for 3 minutes until the cell monolayer had dislodged from the flask. A single cell suspension was generated by pipetting and centrifuged for 3 minutes. The supernatant was removed and the pellet containing the cells was re-suspended in 10ml of cell culture medium. Cells were then counted using a haemocytometer. The average of four different counts was used to calculate cell numbers in a 10 ml suspension.

### 3.2.3 Cytocompatibility Evaluation

Cytocompatibility evaluation was performed following the Japanese guidance on cytotoxicity test methods for biological safety evaluation of medical devices as a direct contact method [15]. Then the samples were separately located into the bottom of 24-well microplates. Murine fibroblast L929 was cultured onto each disk at the concentration of 80 cells/well in 1 mL of the culture medium, Eagle's minimum essential medium, E-MEM+FBS. The same number of cells was seeded into the well without a sample disk as a control. The cells were incubated at 37°C under 5 vol.% CO<sub>2</sub> in humidified air for 7 days. After the incubation, the cells were fixed with 25 vol.% glutaraldehyde solution for 10 min and stained with 10 vol.% Giemsa's staining solution for 15 min. Fig. 3.1 shows the surface of the samples with Giemsa's stained colony. The stained colonies were observed by an optical microscope and their images were captured via a CCD camera. Then, relative plating efficiency (PE) was determined as follows:

$$PE = [(N_s / A_s) / (N_c / A_c)] \quad \text{Eqn. 3.1}$$

where N<sub>s</sub> and N<sub>c</sub> indicate the average numbers of colonies on the sample top surface and in the control well, respectively. A<sub>s</sub> and A<sub>c</sub> indicate the sample top surface area and the well bottom area, respectively.

These experiments were performed in triplicate. Obtained PE data was statistically analyzed by paired Student's t-test.

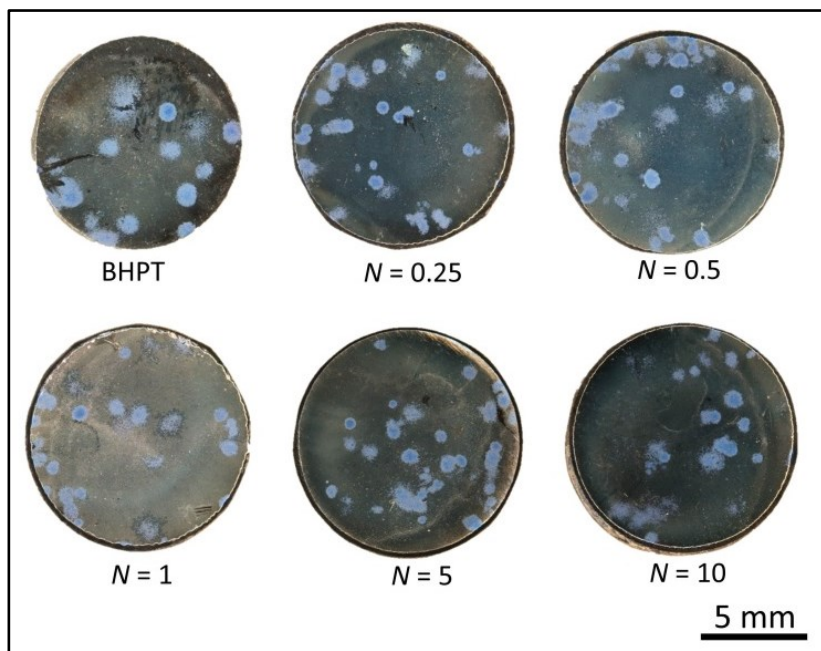


Fig. 3.1 Giemsa-stained samples showing the colony on the Ti-50mol%Ni samples surfaces.

### 3.2.4 Nickel ion release

Ni ion release from the sample into E-MEM+FBS during cell culture was analyzed. After 7 days of cell culture, the culture media for three samples were separately collected and mixed for the measurement of Ni ion concentration in the media by inductively coupled plasma mass spectrometry (ICP-MS) at Biko Chemical Company Ltd. under the optimum condition.

### 3.2.5 Protein adsorption analysis

Protein adsorption analysis was performed for albumin and vitronectin by using silver-enhanced immunogold technique. This technique allows for visualization of surface markers by scanning electron microscope. After the EOG sterilization, the samples were placed in the 24-well microplates and immersed into 0.5 mL of E-MEM+FBS. The samples were placed in a CO<sub>2</sub> incubator for 24 hrs. Then, the samples were rinsed with Dulbecco's phosphate buffered saline [PBS(-)] and fixed immediately using 10 vol.% formalin-methanol solution (Mildform® 10NM, WAKO Pure Chemical Industries, Ltd.) for 15 min at room temperature. The samples were washed 3 times in 10 nM glycine in PBS(-), followed by blocking in 5 vol.% Goat Serum in PBS(-) for 15 min. Then the samples were incubated with a primary antibody (Anti albumin, bovine (rabbit), Cosmo Bio Ltd LB-1027, 1:2000 dilution, or Anti vitronectin, bovine (rabbit), Cosmo Bio Ltd., LB-2007, 1:2000 dilution) for 1 hr at room temperature. After the

incubation with the primary antibody, the samples were washed 3 times in 1 vol.% Goat Serum in PBS(-). The samples were then incubated with a gold-labeled secondary antibody (Anti IgG, rabbit (goat), labeled with gold 10nm, Sigma-Aldrich Co. Ltd, Sigma-G7402, 1:50 dilution) for 1 hr at room temperature. The samples were rinsed 3 times in 1 vol.% Goat serum in PBS(-) prior to fixing with 2.5 vol.% glutaraldehyde solution in PBS(-) for 10 min. The samples were washed in ultrapure water three times. Then, silver-enhancement was performed following the instruction given with the kit (Sigma Aldrich Co Ltd, silver-enhancer kit, SE-100). A negative control sample was prepared similarly, except the primary antibody step was omitted. A positive control samples was also prepared similarly except the samples were immersed in the 5% bovine serum albumin in PBS(-) for 24hr in CO<sub>2</sub> incubator. Fig. 3.2 shows the typical micrograph of the antibodies negative and positive control.

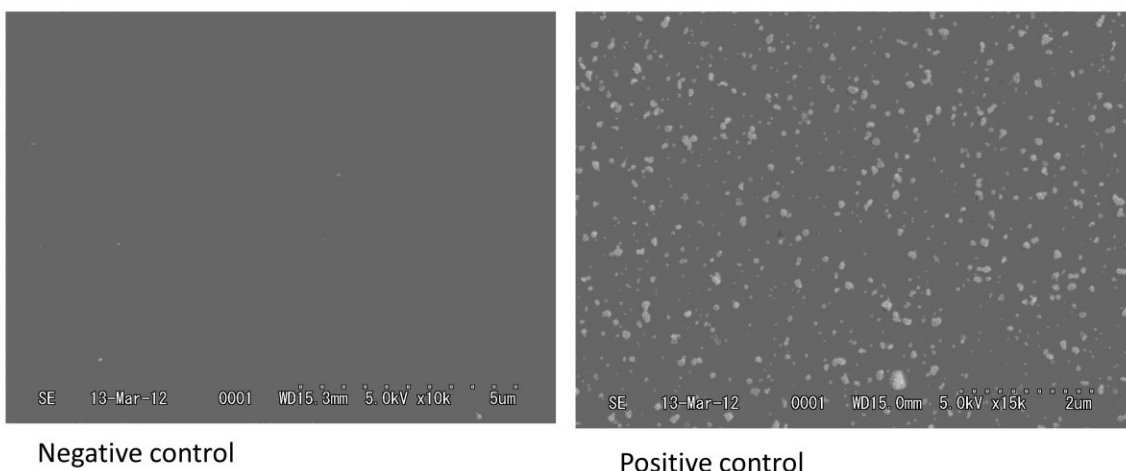


Fig. 3.2 SEM images of BHPT Ti-50mol% showing the negative and positive control.

All samples were visualized using the secondary electron mode (magnification: 10,000x, accelerating voltage: 5kV) of the field-emission scanning electron microscope (FE-SEM; Hitachi S-4300, Hitachi Co., Ltd., Japan). Particle area fraction was calculated based on gray scale, threshold FE-SEM images using the ImageJ software [17]. Five images with the view size of 12.5 μm × 8.5 μm were analyzed for each sample. The obtained data were then statistically analyzed by paired Student's t-test.

### 3.3 Results

#### 3.3.1 Colony formation and morphology

Fig. 3.3 and Fig. 3.4 shows the typical microscopic images of the colony morphology formed on the surface of Ti-50mol%Ni and Ti-50.9mol%Ni respectively. As shown in Fig. 3.3(a), the colonies on BHPT samples have loose appearances with slightly bigger size of each cell. The colonies on  $N = 0.25, 0.5$  and  $1$  samples are more packed with smaller cells as shown in Fig. 3.3 (b)-(d). This may be due to the faster cell growth on the HPT-deformed samples. In high rotation samples ( $N = 5$  and  $N = 10$ ), the colonies formed on the surface are the mixture of tight-packed and loose ones though only the latter is shown in Fig. 3.4(e)-(f). In Fig. 3.4(a) the colonies on the BHPT sample have loose appearances with slightly bigger size of each cell. However, the morphology of colonies formed on HPT deformed samples are more packed with smaller cells as shown in Fig. 3.4 (b)-(f).

The PE of L929 cultured on the HPT-deformed samples is summarized in Fig. 3.5. For all samples, PE was higher than 1, indicating better plating efficiency on TiNi samples than the tissue culture polystyrene. Fig. 3.5(a) shows the plating efficiency of Ti-50mol%Ni samples. In comparison with the samples before HPT (BHPT), PE increased gradually with the number of HPT rotation until it reached maximum at  $N = 1$  though no statistically significant difference was observed. Then, PE slightly decreased at  $N = 5$  and  $N = 10$ . In Ti-50.9mol%Ni, as shown in Fig. 3.5 (b), PE increased gradually with the number of HPT rotation up to  $N = 0.5$ , and then, slightly decreased at  $N = 1$  and  $5$  before it increased again at  $N = 10$ . However, there is no significant difference in the PE among the samples.

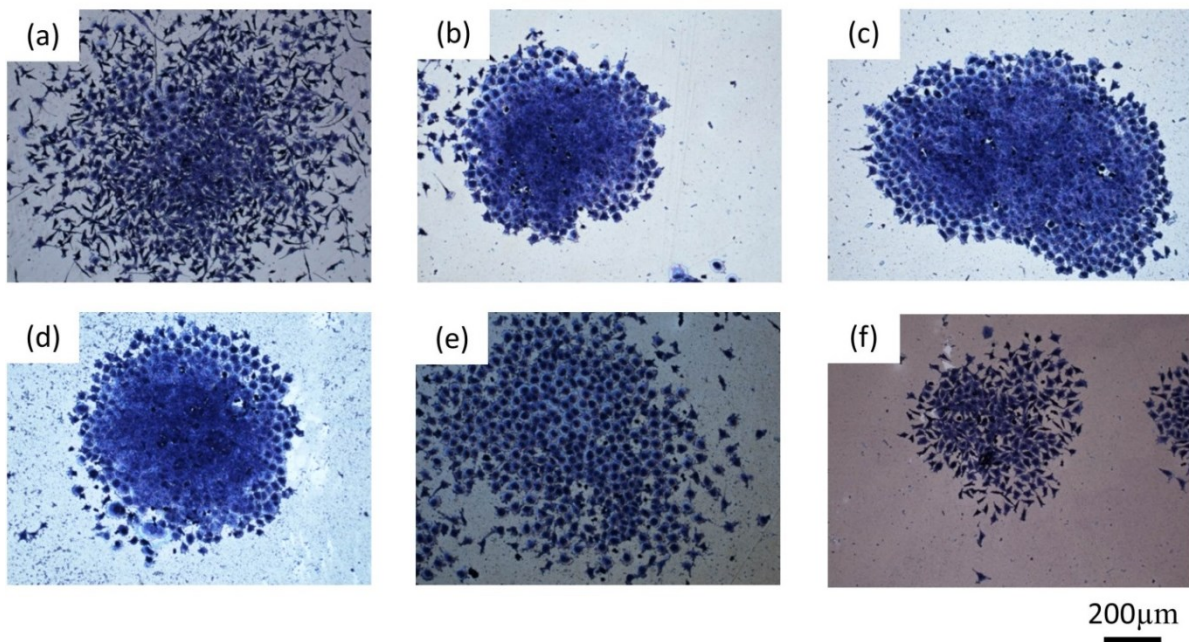


Fig. 3.3 Representative image showing colony morphology formed on the surface of (a) BHPT (b)  $N = 0.25$  (c)  $N = 0.5$ , (d)  $N = 1$ , (e)  $N = 5$  and (f)  $N = 10$  Ti-50mol%Ni samples

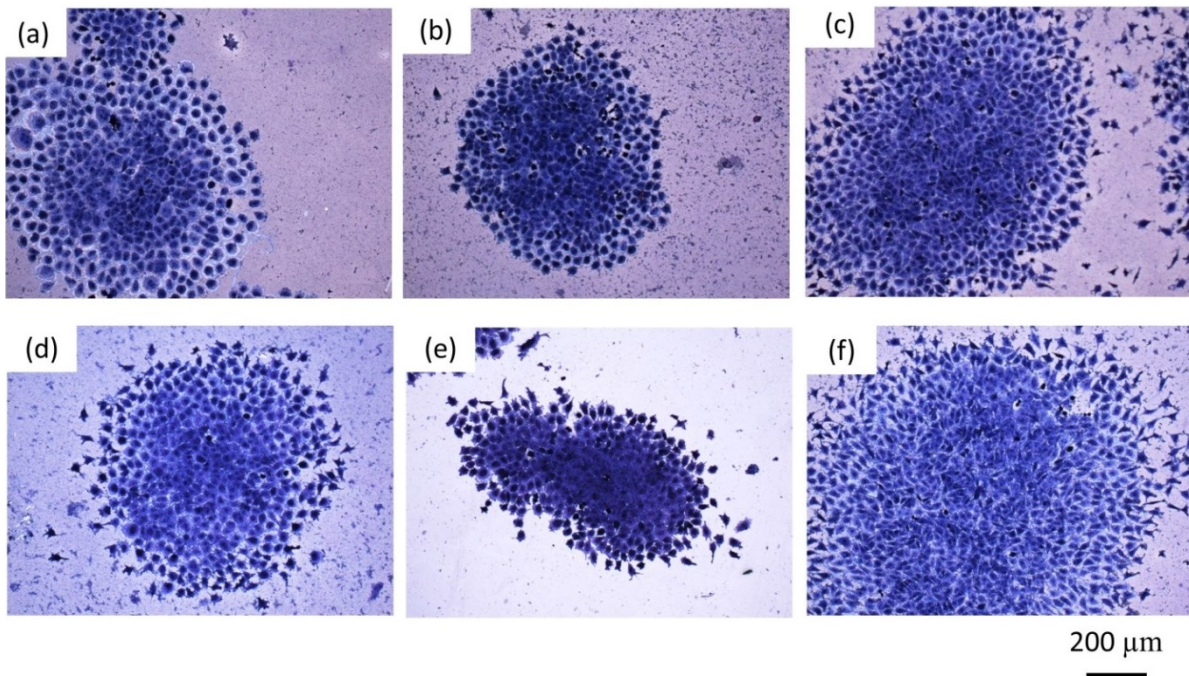


Fig. 3.4 Representative image showing colony morphology formed on the surface of (a) BHPT (b)  $N = 0.25$  (c)  $N = 0.5$ , (d)  $N = 1$ , (e)  $N = 5$  and (f)  $N = 10$  Ti-50.9mol%Ni samples

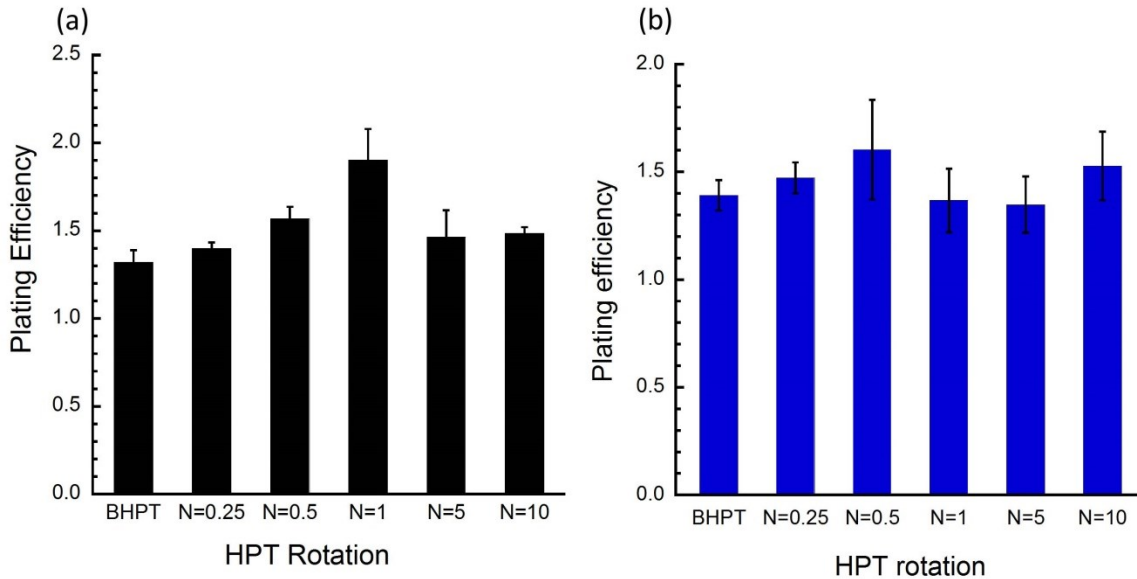


Fig. 3.5 Plating efficiency of (a) Ti-50mol%Ni and (b) Ti-50.9mol%Ni.

### 3.3.2 Ni ion release

Nickel ion release in the cell culture medium after 7 day of cell culture is shown in Fig. 3.6. In Ti-50mol%Ni (Fig. 3.6 (a)), the BHPT samples have the highest Ni ion release of  $42.9 \text{ ng ml}^{-1} \text{ cm}^{-2}$ . By the rotation of  $N = 0.25$ , the amount of released Ni ion was reduced to  $12.1 \text{ ng ml}^{-1} \text{ cm}^{-2}$ . The Ni ion release for  $N = 0.5, 1, 5$  and  $10$  samples were  $3.74, 9.67, 3.32$  and  $3.14 \text{ ng ml}^{-1} \text{ cm}^{-2}$  respectively. Fig. 3.6 (b) shows the Ni ion release from Ti-50.9mol%Ni. The BHPT sample has the highest Ni ion release at  $23.0 \text{ ng ml}^{-1} \text{ cm}^{-2}$ . By the rotation of  $N = 0.25$ , the amount of released Ni ion was reduced more than 5 folds at  $4.23 \text{ ng ml}^{-1} \text{ cm}^{-2}$ . The Ni ion release of deformed samples was peaked at  $N = 0.5$  at  $7.86 \text{ ng ml}^{-1} \text{ cm}^{-2}$ , and the lowest is at  $N = 5$  as  $3.14 \text{ ng ml}^{-1} \text{ cm}^{-2}$ .

### 3.3.3 Protein adsorption behavior

Protein adsorption on the sample surfaces was investigated for albumin and vitronectin in the cell culture condition. Fig. 3.7(a) shows the albumin absorption on the Ti-50mol%Ni samples. BHPT has the lowest albumin absorption on the surface whereas  $N = 0.25$  has the highest amount of absorbed albumin. For the samples with  $N = 0.25$  and higher rotations, the amount of absorbed albumin started to decrease with the number of rotation. Fig. 3.7(b) shows the vitronectin absorption on the Ti-50mol%Ni sample surfaces. Vitronectin adsorption onto BHPT and HPT-deformed samples was relatively higher than albumin to these samples. Vitronectin adsorption was the highest at  $N = 1$  samples, followed by BHPT.

HPT- deformed samples at low rotation ( $N = 0.25, 0.5$ , and  $1$ ) have higher vitronectin adsorption compared to those of the samples at high rotation ( $N = 5, 10$ ).

Fig. 3.8 (a) shows the variation in albumin absorption on the Ti-50.9mol%Ni samples. The albumin adsorption was found to gradually increase from BHPT to  $N = 0.5$  and to decrease up to  $N = 5$  before it increased again at  $N = 10$ . Fig. 3.8(b) shows the vitronectin absorption on the Ti-50.9mol%Ni sample surfaces. Vitronectin adsorption had the similar trend to that of albumin adsorption; it was higher on the low rotation samples being maximum at  $N = 0.5$  than BHPT, while those on high rotation samples ( $N = 5$  and  $N = 10$ ) did not show any significant difference to that on BHPT. As same as Ti-50mol%Ni, the vitronectin adsorption was higher than albumin adsorption on all samples.

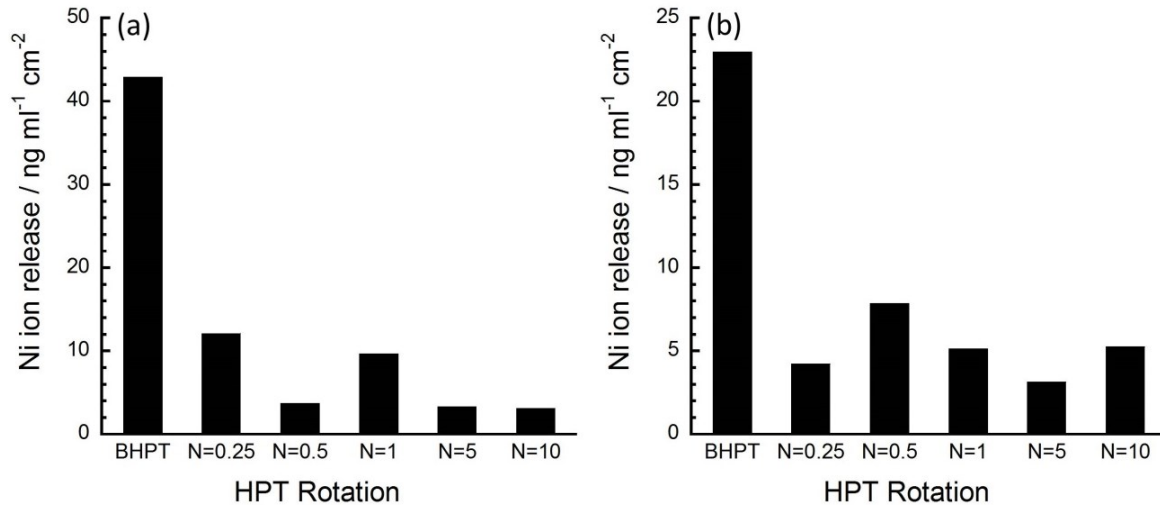


Fig. 3.6 Ni ion release from (a) Ti-50mol% Ni and (b) Ti-50.9mol%Ni as a function of HPT rotation.

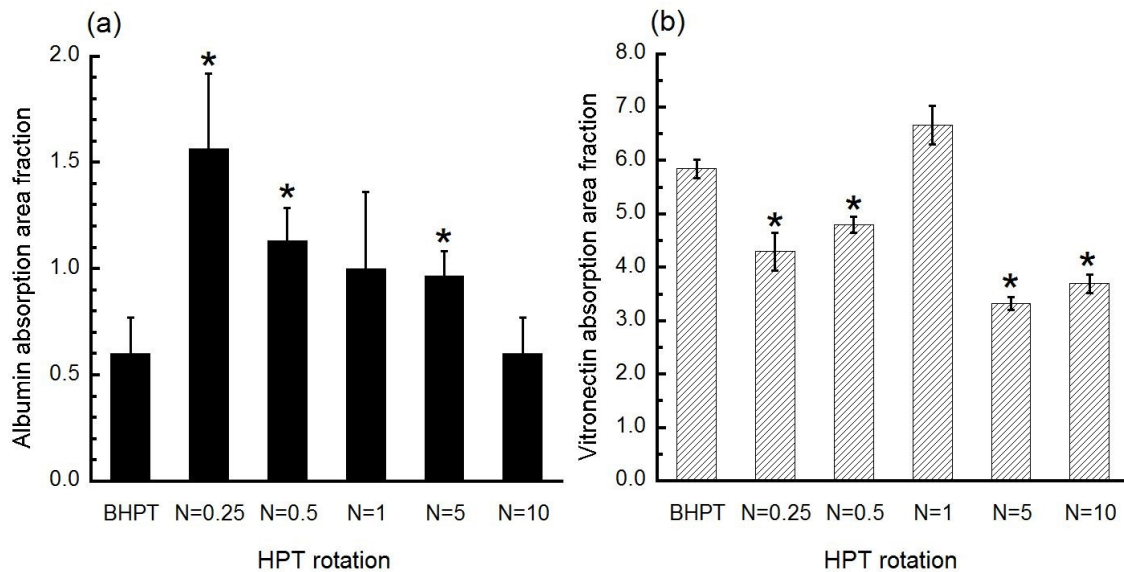


Fig. 3.7 (a) Albumin and (b) vitronectin adsorption on Ti-50mol%Ni as function of HPT rotation.

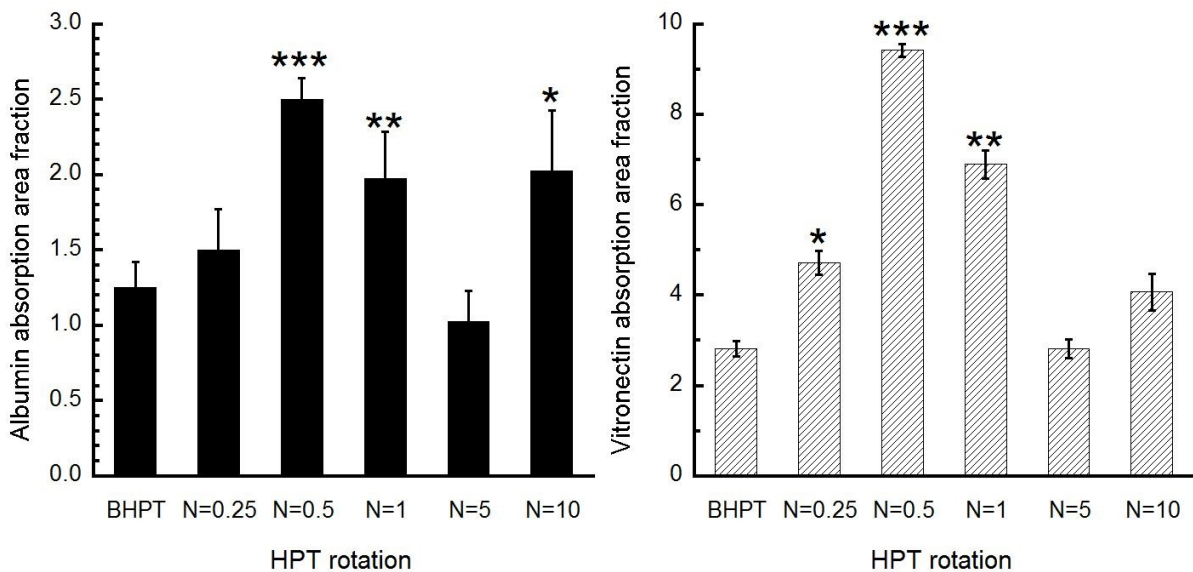


Fig. 3.8 (a) Albumin and (b) vitronectin adsorption on Ti-50.9mol%Ni as function of HPT rotation.

### 3.4 Discussion

#### 3.4.1 Effect of HPT on the colony formation behavior

Cell growth behavior on the sample surface is used to evaluate the effect of HPT deformation on the cytocompatibility of TiNi samples. Colony formation on the samples with and without HPT deformation shows a slight increase in the average colony number especially around  $N = 1$ , even though there is no significant difference among the samples. The average colony number was the lowest on the BHPT samples and peaked at  $N = 1$  sample in Ti-50mol%Ni and  $N = 0.5$  in Ti-50.9mol%Ni, indicating the improvement in TiNi cytocompatibility by HPT deformation. It is noted that the trend of PE (peaked at  $N = 1$  for Ti-50mol%Ni and  $N = 0.5$  for Ti-50.9mol%Ni) agreed with the trend of FWHM shown in Fig 2.2(b) and Fig. 2.3(b), respectively. The colony morphology on the samples was also observed to change depending on the HPT rotations. In Ti-50mol%Ni, the colony morphology on BHPT was loose whereas those on low rotation samples ( $N = 0.25, 0.5$  and  $1$ ) were tight and dense. On high rotation samples ( $N = 5$  and  $10$ ), those were the mixture of close and loose packs. The same behavior was observed in Ti-50.9mol%Ni in which the colony formed on the HPT deformed samples were denser in comparison to BHPT sample. Few damaged cells were also observed on the BHPT samples, indicating the sign of cytotoxicity. The changes in the colony morphology suggest the difference in protein adsorption behavior and cell-material interaction on BHPT and HPT-deformed samples. The close packed colony is associated with the improved cell integration [10] and good cell-cell interaction.

Surface characteristics of materials, such as their topography, chemistry or surface energy, play an essential part in cell adhesion on biomaterials. The attachment, adhesion and spreading of cell during first phase of cell and material interactions influence the cell's capacity to proliferate or differentiate on contact with the implant. As demonstrated in Chapter 4, the surface chemistry of the TiNi alloys show changes after HPT deformation. Increase in the dislocation density increased the reactivity of the surface, and this might influence the cell growth behavior. High density of the surface charges leads to dense arrangement of attached cells [11].

#### 3.4.2 Suppression of Ni ion release by HPT deformation

One of the causes for improvement in cell-cell integration as discussed in section 3.4.1 is the suppression of Ni ion release from the HPT-deformed samples into the culture medium during cell culture (see Fig. 3.6). The suppression of Ni ion release was also reported for ultrafine-grained TiNi prepared by ECAP [12]. In case of a TiNi alloy, suppression of cell growth is reported due to the presence of Ni ion in the cell culture medium. The presence of metallic Ni in the cell culture medium was found to be [1,13].

The Ni ion release has drastically reduced only with a quarter turn of HPT, but has a slight increase at  $N = 1$ . The XRD pattern of  $N = 1$  sample obtained indicates the least peak intensity of martensitic phase (B19') which slightly increased on  $N = 5$  and  $N = 10$  sample surfaces. This microstructural change may influence the passive film formation kinetics and thus, influences Ni ion release. The slight increase in  $\text{Ni}^{[\text{Me}]}/\text{Ti}^{[\text{Me}]}$  at  $N = 1$  and its good correlation to the Ni ion release (Fig.3) support above hypothesis.

The slight increase in cell growth, cell integration and drastic decrease in Ni ion release will be beneficial for biomedical application of TiNi alloys, since the biocompatibility of metallic biomaterials depends on their stability in biological condition and surface physicochemical properties. The former directly decides the released amounts of degradation products, whereas the latter controls protein adsorption behavior and following cellular response. For metallic biomaterials currently applied to implant devices, the former is more important since the effect of released metal ions or debris is crucial on cell survival.

### 3.4.3 Effect of HPT on the protein adsorption behavior

Protein adsorption on a material surface is important since it determines cellular response on the surface. Adsorbed proteins coordinate to receptors on cell membranes, leading to cellular adhesion to material surface [14,15]. Therefore, the protein adsorption was examined by immune reaction for specific types of proteins, namely albumin and vitronectin. In this study, vitronectin adsorption is relatively high than that of albumin even though the concentration of albumin in FBS is much higher than that of vitronectin. Vitronectin is one of the abundant glycoprotein present in plasma that helps promote cell adhesion and reorganization of the actin microfilaments [19], which is an important process for cell motility and growth.

In Ti-50mol%Ni albumin adsorption was found to be higher on the HPT-deformed samples, and decreased along the increase in the HPT rotations. Meanwhile the vitronectin adsorption was the highest at the  $N = 1$  samples, followed by the BHPT samples. For the samples with low HPT rotations ( $N = 0.25$ , 0.5, and 1), increased along the increase in the HPT rotation whereas it decreased for the samples over  $N = 5$ . This might be due to the good affinity of vitronectin with  $\text{TiO}_2$  [20]. In Ti-50.9mol%Ni, the adsorption of both albumin and vitronectin onto TiNi surface also had the similar trend to each other; it increased by the HPT deformation up to  $N = 0.5$ , decreased to  $N = 5$ , and increased again at  $N = 10$ . It is interesting to note that the trend of PE shown in Fig. 3.5 followed the behavior of vitronectin adsorption. This may be attributed to the higher affinity of vitronectin to the substrate surface leading to its function as cell adhesive molecules.

Although it is not clearly understood, this observation suggests the correlation between the bioperformance and the phase changes in the samples due to HPT deformation. Low rotation samples ( $N = 0.25$ , and  $0.5$ ) were mainly in mixture of nanocrystalline B2 and martensitic B19' phases, and the latter was substituted by the B2 phase with further HPT deformation at  $N = 1$  and  $5$ . A. Michiardi et al. reported that the martensitic TiNi has higher albumin adsorption than the austenitic one [21], which suggests that the appearance and area fraction of the martensitic phase causes the increase in protein adsorption in the present study. The increase of deformation-induced martensites also increases the complexity of the sample microstructure, which probably gives more surface active sites such as grain boundaries. These active sites are considered to be effective to accelerate the adsorption of organic molecules including proteins.

### **3.5 Conclusion**

In this chapter, we have demonstrated the effect of HPT deformation on the cell growth, protein adsorption and Ni ion release behavior of TiNi alloys. The phase and microstructural changes due to HPT deformation was found to alter the protein adsorption behavior on the surface. Ni ion release as well as protein adsorption behavior influences L929 cell growth and colony morphologies on the TiNi alloys surface. The Ni ion release was also found to decrease with the HPT deformation. The results obtained suggest the possibility of controlling biocompatibility of TiNi alloys by HPT deformation via their stability in biological condition and protein adsorption behavior onto their surfaces, which can contribute to widen the application of bare TiNi alloys in the biomedical field.

### 3.7 References:

- [1] Ratner B, Ren X. Biomaterials: where we have been and where we are going. *Annu. Rev. Biomed. Eng.* 2004.
- [2] Trepanier C, Venugopalan R, Pelton A. Corrosion resistance and biocompatibility of passivated NiTi. In: Yahia LH, editor. *Shape memory implants*, Shape memory implants. Berlin: Springer; 2000, pp. 35–45.
- [3] Firstov GS, Vitchev RG, Kumar H, Blanpain B, Van Humbeeck J. Surface oxidation of NiTi shape memory alloy. *Biomaterials* 2002;23:4863–71.
- [4] Michiardi A, Aparicio C, Planell JA, Gil FJ. Electrochemical behaviour of oxidized NiTi shape memory alloys for biomedical applications. *Surface and Coatings Technology* 2007;201:6484–8.
- [5] Cissé O, Savadogo O, Wu M, Yahia L. Effect of surface treatment of NiTi alloy on its corrosion behavior in Hanks' solution. *J. Biomed. Mater. Res.* 2002;61:339–45.
- [6] Yeung KWK, Poon RWY, Liu XY, Ho JPY, Chung CY, Chu PK, Lu WW, Chan D, Cheung KMC. Corrosion resistance, surface mechanical properties, and cytocompatibility of plasma immersion ion implantation-treated nickel-titanium shape memory alloys. *J. Biomed. Mater. Res.* 2005;75A:256–67.
- [7] Pelletier H, Muller D, Mille P, Grob J. Structural and mechanical characterisation of boron and nitrogen implanted NiTi shape memory alloy. *Surf. Coat. Tech.* 2002;158:309–17.
- [8] Undisz A, Schrempel F, Wesch W, Rettenmayr M. In situobservation of surface oxide layers on medical grade Ni-Ti alloy during straining. *J. Biomed. Mater. Res.* 2009;88A:1000–9.
- [9] Shabalovskaya SA, Tian H, Anderegg JW, Schryvers DU, Carroll WU, Van Humbeeck J. The influence of surface oxides on the distribution and release of nickel from Nitinol wires. *Biomaterials* 2009;30:468–77.
- [10] Furuhashi A, Ayukawa Y, Atsuta I, Okawachi H, Koyano K. The difference of fibroblast behavior on titanium substrata with different surface characteristics. *Odontology* 2012;100:199–205.
- [11] Feng B, Chen JY, Qi SK, He L, Zhao JZ, Zhang XD. Characterization of surface oxide films on titanium and bioactivity. *J Mater Sci Mater Med* 2002;13:457–64.
- [12] Zheng CY, Nie FL, Zheng YF, Cheng Y, Wei SC, Valiev RZ. Enhanced in vitro biocompatibility of ultrafine-grained biomedical NiTi alloy with microporous surface. *App. Surf. Sci* 2011;1–8.
- [13] Gu YW, Li H, Tay BY, Lim CS, Yong MS, Khor KA. In vitro bioactivity and osteoblast response of porous NiTi synthesized by SHS using nanocrystalline Ni-Ti reaction agent. *J. Biomed. Mater. Res.* 2006;78:316–23.
- [14] Ratner BD, Hoffman AS, Schoen FJ, Lemons JE, editors. *Biomaterials Science: An Introduction to Materials in Medicine*. 2nd ed. Elsevier Academic Press; 2004.
- [15] Breme J, Kirkpatrick CJ, Thull R, editors. *Metallic Biomaterial Interfaces*. 1st ed. Wiley-VCH; 2008.
- [16] Clarke B, Kingshott P, Hou X, Rochev Y, Gorelov A, Carroll W. Effect of nitinol wire surface properties on albumin adsorption. *Acta Biomater* 2007;3:103–11.
- [17] Martins MCL, Wang D, Ji J, Feng L, Barbosa MA. Albumin and fibrinogen adsorption on PU-PHEMA surfaces. *Biomaterials* 2003;24:2067–76.
- [18] Underwood PA, Bennett FA. A comparison of the biological activities of the cell-adhesive proteins vitronectin and fibronectin. *J. Cell. Sci.* 1989;93 ( Pt 4):641–9.
- [19] Degasne I, Basle MF, Demais V, Hure G, Lesourd M, Grolleau B, Mercier L, Chappard D. Effects of Roughness, Fibronectin and Vitronectin on Attachment, Spreading, and Proliferation of Human Osteoblast-Like Cells (Saos-2) on Titanium Surfaces. *Calcif. Tissue Int.* 1999;64:499–507.
- [20] Zhang H, Bremmell K, Kumar S, Smart RSC. Vitronectin adsorption on surfaces visualized by tapping mode atomic force microscopy. *J. Biomed. Mater. Res.* 2004;68:479–88.

*Chapter 3*

- [21] Michiardi A, Aparicio C, Ratner BD, Planell JA, Gil J. The influence of surface energy on competitive protein adsorption on oxidized NiTi surfaces. *Biomaterials* 2007;28:586–94.

## **Chapter 4 Surface characterization of HPT deformed TiNi alloys**

### **4.1 Introduction**

When a material contacts with physiological environment, change in the surface physical properties and chemistry might occur. Enhanced mobility and higher reactivity of surface atoms, in comparison to bulk, leads to change in phase transformation, crystallization or dissolution (corrosion) process. Surface characteristic plays an important factor in determining the biocompatibility of an alloy.

Thus, in order to understand the difference of surface and bulk properties, a study on the chemical composition and atomic arrangement is crucial. In Chapter 2 and 3, it was shown that the HPT deformation suppressed the Ni ion release into the cell culture medium. The metal ion release was primarily dictated by the surface of an alloy. In a passive metal such as TiNi alloys, the naturally occurred passive film protects the metal going into active dissolution.

This study is primarily aimed at a better understanding on the composition of the passive film in the TiNi alloys before and after HPT deformation. The change in surface characteristics after the cell culture was also investigated to shed some light in the change of surface after cell culture. The experimental works focuses on the elemental analysis of the surface chemistry and their changes. The systematic X-ray photoelectron spectroscopic study of TiNi alloys before and after cell culture is reported.

## 4.2 Experimental method

### 4.2.1 Sample preparation

TiNi alloys prepared as in Section 2.2.1 were cleaned and sterilized by EOG to mimic the surface condition of the TiNi alloys prior to cell culture. For the investigation after cell culture, samples were rinsed with PBS(-), trypsinized for 3 min to remove adhering cells on the surface, and rinsed in the ultrapure water in the ultrasonic bath.

### 4.2.2 X-ray photoelectron spectroscopy

X-ray photoelectron spectroscopy (XPS) was used to characterize the surface of the samples. The XPS spectra were obtained by an XPS system (K-Alpha, Thermo Fisher Scientific Inc.) with a monochromatic Al-K $\alpha$  (energy=1486.71 eV). Samples were positioned at the electron take-off angle normal to the surface with respect to the analyzer. Survey spectra in the range 0-1400 eV were recorded for each samples followed by high resolution XPS peaks for Ti 2p, Ni 2p, O-1s and C 1s. For the analysis, all peaks were referenced relative to the main C-1s peak at 285.0 eV. Peak deconvolution and elemental atomic quantification were determined from the high resolution spectrum using XPS peak-fitting software (XPS Peak 4.1). To estimate the photoelectron peak intensities, the background was subtracted from the measured spectrum according to Shirley's method. The quantitative determination of the chemical compositions of the surface oxide were calculated using a published method [1]. Corrections were made for the transmission function of the spectrometer supplied by the manufacturer. The inelastic mean free-path of the electrons was assumed to scale with their kinetic energy  $E$  as  $E^{0.6}$ .

The XPS depth profiles were recorded using Ar+ ion bombardment at 3 kV energy, with a raster size of 4 × 4 mm. The thickness of the surface oxide was estimated as the point at which the oxygen peak reached half of its maximum concentration. The sputtering rate of 2.72 nm/min was determined against SiO<sub>2</sub> standard and also checked by the crater depth.

### **4.3 Results**

#### **4.3.1 Surface characterization of Ti-50mol%Ni**

Overall survey and high resolution spectra of major elements were measured and recorded. Fig. 4.1 shows a typical survey spectrum from BHPT TiNi alloys before the cell culture. The major elements detected are carbon, oxygen, titanium and nickel. High resolution spectra of each element were used to investigate the effect of HPT processing on the formation of the passive film. Chemical compositions of the passive films on the TiNi sample surface before and after HPT prior to cell culture as obtained from XPS spectra are presented in Table 4.1.

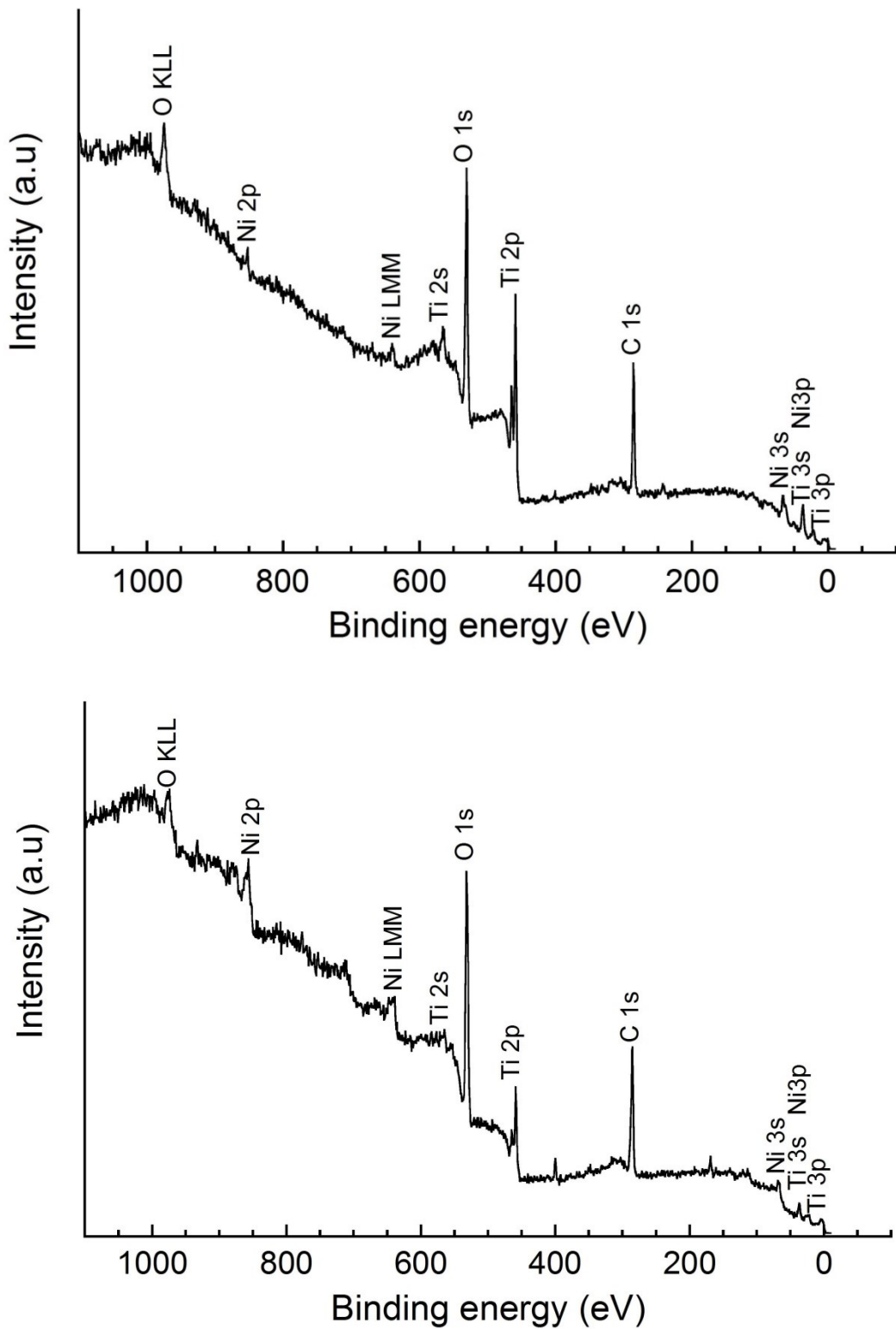


Fig. 4.1 A representative survey XPS spectrum of (a) BHPT Ti-50mol% Ni and (b) BHPT Ti-50.9mol%Ni.

Table 4.1 Chemical composition of the Ti-50 mol%Ni surface samples as measured by XPS

Sample	Atomic concentration (at%)				$\text{Ni}^{[\text{Me}]}/\text{Ti}^{[\text{Me}]}$
	C1s	Ti2p	O1s	Ni2p	
BHPT	31.83	19.06	46.87	2.24	3.96
$N = 0.25$	33.7	19.65	44.87	1.78	1.38
$N = 0.5$	49.6	9.97	37.47	2.96	1.15
$N = 1$	58.31	6.26	31.34	4.09	1.22
$N = 5$	60.54	3.91	32.79	2.76	1.00
$N = 10$	63.78	5.85	28.77	1.61	1.01

Table 4.2 Chemical composition of the Ti-50 mol%Ni surface samples as measured by XPS after cell culture

Sample	Atomic concentration (at%)					Ti/Ni	$\text{O}^{2-}/\text{OH}^-$
	C1s	Ti2p	O1s	Ni2p	N1s		
BHPT	56.44	7.84	30.14	0.57	5.01	13.75	0.44
$N = 0.25$	47.1	12.05	37.36	0.32	3.17	37.66	1.13
$N = 0.5$	53.33	8.57	32.66	0.8	4.63	10.71	0.62
$N = 1$	52	6.88	30.72	0.54	9.86	12.74	0.64
$N = 5$	64.86	1.87	19.92	0.16	13.19	11.69	1.20
$N = 10$	67.47	3	22.52	0.4	6.62	7.50	1.08

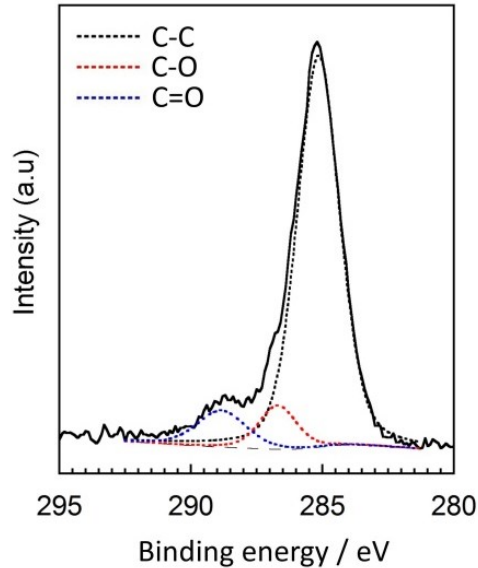


Fig. 4.2 Deconvolution of C1s peak on Ti-50mol% BHPT sample.

*C 1s spectra.* The C 1s peak obtained from all the samples were further deconvoluted into 3 peaks: 285 eV (C-C, C=C or C-H), 286.5 eV (C-O single bond) and 288.4 eV (carboxyl or amide group) [2-5] as shown in Fig. 4.2. Fig. 4.3(a) shows the series of C1s peaks obtained from the XPS prior to cell culture. Since none of the carbon peaks were detected at higher energy binding region, it was concluded that the carbon on the surface originated from contaminant carbon [6-8]. Furthermore, after sputtering for 50s this carbon peak disappears indicates that the carbon peak arises from contamination. Fig. 4.3(b) shows the C 1s peak obtained from all the samples after cell culture, which were also can be further deconvoluted into 3 peaks at energies of 285, 286.5 and 288.4 eV. In comparison to the XPS spectra of the sample before cell culture, the C 1s peaks after cell culture shows some increase in the latter two peaks. These two peaks were considered to be originated to the adsorption of organic compounds, but some of them occurred before the samples are employed to the cell culture [9]. The peak at the highest binding energy (288.4 eV) corresponds to carboxyl or amide groups. All of these peaks may come from the adsorbed organic compounds such as proteins, amino acids, and carbohydrates during the cell culture[3,10].

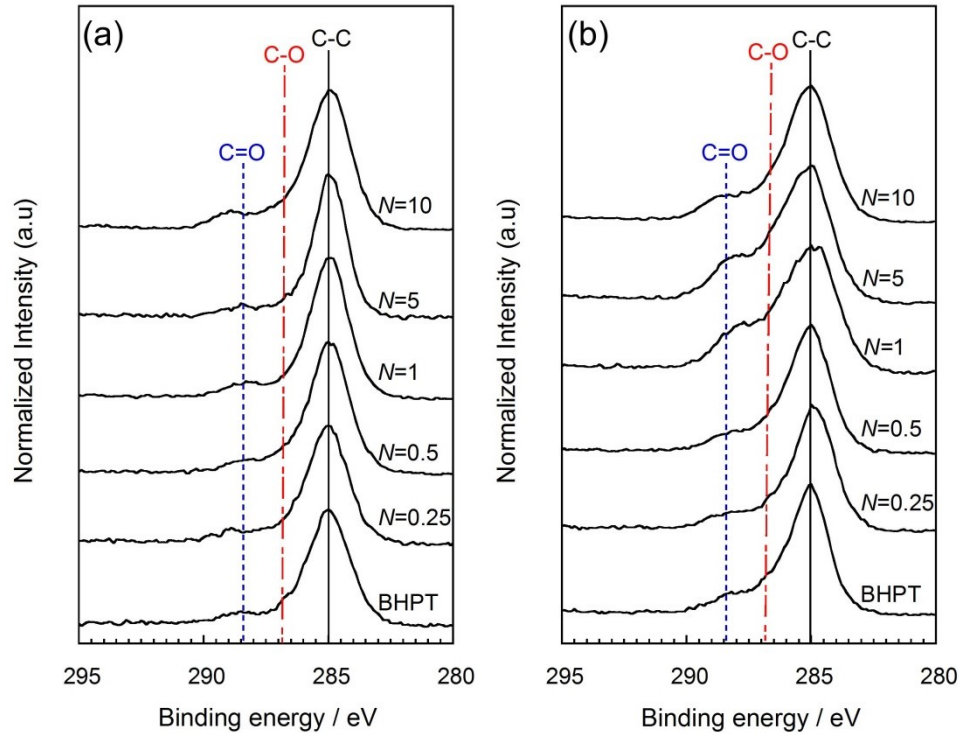


Fig. 4.3 Series of C1s peak of Ti-50mol%Ni (a) before and (b) after cell culture.

*Ti 2p spectra.* High resolution XPS of the Ti 2p spectra (Fig. 4.4) shows the major peaks at binding energies at 459 eV and 465 eV, which corresponds to Ti 2p<sub>3/2</sub> and Ti 2p<sub>1/2</sub> states of the stoichiometric TiO<sub>2</sub> (Ti<sup>4+</sup>). Further deconvoluted peaks show a doublet at 454.2 eV (Ti 2p<sub>3/2</sub>) and 460.4 eV (Ti 2p<sub>1/2</sub>) which correspond to metallic Ti (Ti<sup>[Me]</sup>) in the substrate [11,12]. It is expected to detect Ti<sup>[Me]</sup> originated from the substrate since passive film formation at room temperature for TiNi typically reaches the equilibrium at around 3 nm [13].

High resolution XPS of the Ti 2p region shows the major peaks at the binding energies of 459 and 465 eV, which correspond to Ti 2p<sub>3/2</sub> and Ti 2p<sub>1/2</sub> states of the stoichiometric TiO<sub>2</sub> (Ti<sup>4+</sup>), respectively. The surface is completely covered by TiO<sub>2</sub> as there is no metallic Ti (Ti<sup>[Me]</sup>) was detected from the XPS spectra. Ti/Ni ratio in Table I shows that all sample surfaces are highly enriched in titanium.

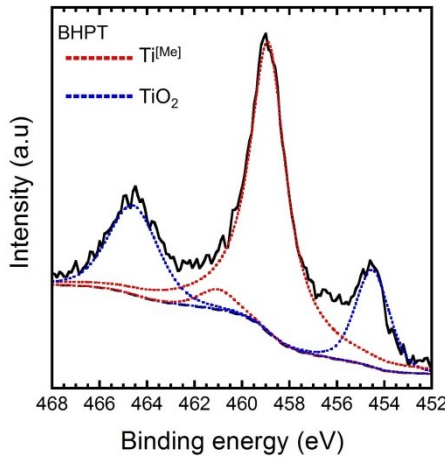


Fig. 4.4 Deconvoluted spectra of Ti 2p region of Ti-50mol%Ni BHPT sample.

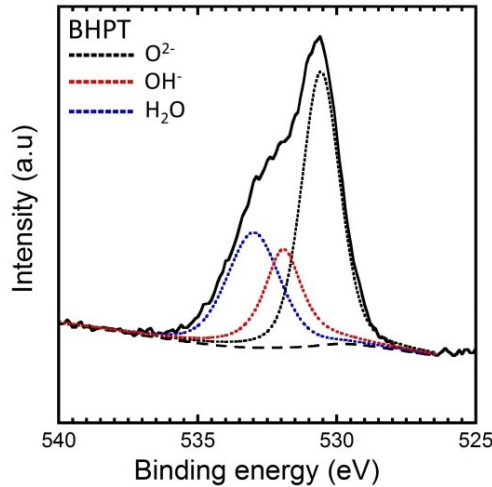


Fig. 4.5 Deconvolution spectra of O 1s region of Ti-50mol%Ni BHPT sample.

*O 1s spectra.* The typical three-peak structure was used to fit the O 1s spectra as shown in Fig. 4.5. The primary peak with binding energy at 530.4 eV is associated with the metal oxide bond (O<sup>2-</sup>), which mainly corresponds to TiO<sub>2</sub>. The other two peaks, having binding energies at 531.5 eV and 533.2 eV, are associated with hydroxyl bond (OH<sup>-</sup>) and chemisorbed water H<sub>2</sub>O, respectively [25].

The TiO<sub>2</sub> enrichment of the TiNi surface was supported by the O 1s spectra as shown in Fig. 4.6 (a). The main peak of O 1s in all samples prior to cell culture was at 530.4 eV. However, as the number of rotations increases, the OH<sup>-</sup> and H<sub>2</sub>O peaks started to rise indicating changes in the chemical composition of formed passive films. In comparison to the spectra for the BHPT and  $N = 0.25$  samples, OH<sup>-</sup> and chemisorbed H<sub>2</sub>O peaks are obvious in the spectra for the samples after  $N = 0.5$ . Table 4.1 shows the

relative fraction of oxide component in O 1s spectra and the ratio of  $[\text{OH}]/[\text{O}^{2-}]$  on the surface films. With an exception for  $N = 0.25$ ,  $[\text{OH}]/[\text{O}^{2-}]$  ratio in deformed samples is higher than those of BHPT, indicating the increase in the amount of  $\text{OH}^-$ .

Fig. 4.6(b) shows the normalized O 1s spectra of Ti-50mol%Ni after the cell culture. The major peak at  $\text{O}^{2-}$  was observed on the BHPT and  $N = 0.25$  samples. However, the main peak started to shift to the position of  $\text{OH}^-$  for the samples with higher rotation over  $N = 0.5$ .

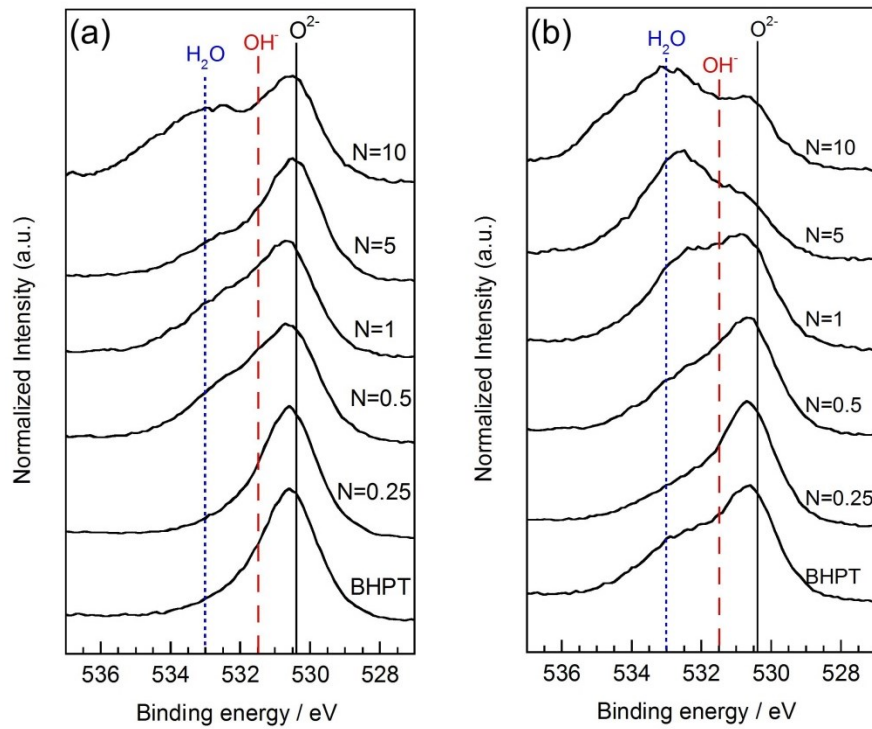


Fig. 4.6 Series of O1s peaks of Ti-50mol%Ni (a) before and (b) after cell culture.

*Ni 2p spectra.* Fig. 4.7 shows a series of Ni 2p<sub>3/2</sub> core-level high resolution spectrum. In BHPT and  $N = 0.25$  samples, a peak is observed at 852.7 eV which is associated with metallic Ni ( $\text{Ni}^{[\text{Me}]}$ ). The NiO is observed as a shoulder peak at 854.3 eV [14]. However, starting at  $N = 0.5$ , the binding energy shifted to higher energy with a major peak at 856.3 eV, which can be attributed to either  $\text{Ni}_2\text{O}_3$  or  $\text{Ni}(\text{OH})_2$ , but probably to the latter since  $\text{Ni}_2\text{O}_3$  is unstable compared to  $\text{Ni}(\text{OH})_2$  [11,13]. The broad peak observed at 862.3 eV is the satellite of  $\text{Ni}(\text{OH})_2$  [15].

Fig. 4.7 shows a series of Ni 2p<sub>3/2</sub> core-level high resolution spectrum before and after cell culture. Before cell culture, for BHPT and  $N = 0.25$ , the main peak was observed at 852.7 eV, which is associated with metallic Ni ( $\text{Ni}^{[\text{Me}]}$ ) [14]. However, another peak at 856.3 eV was observed for the samples with higher rotation over  $N = 0.5$ . This peak can be attributed to either  $\text{Ni}_2\text{O}_3$  or  $\text{Ni}(\text{OH})_2$ , but probably to the latter since  $\text{Ni}_2\text{O}_3$  is unstable compared to  $\text{Ni}(\text{OH})_2$ [11,13]. The broad peak observed at 862.3 eV is the satellite of  $\text{Ni}(\text{OH})_2$ [15].

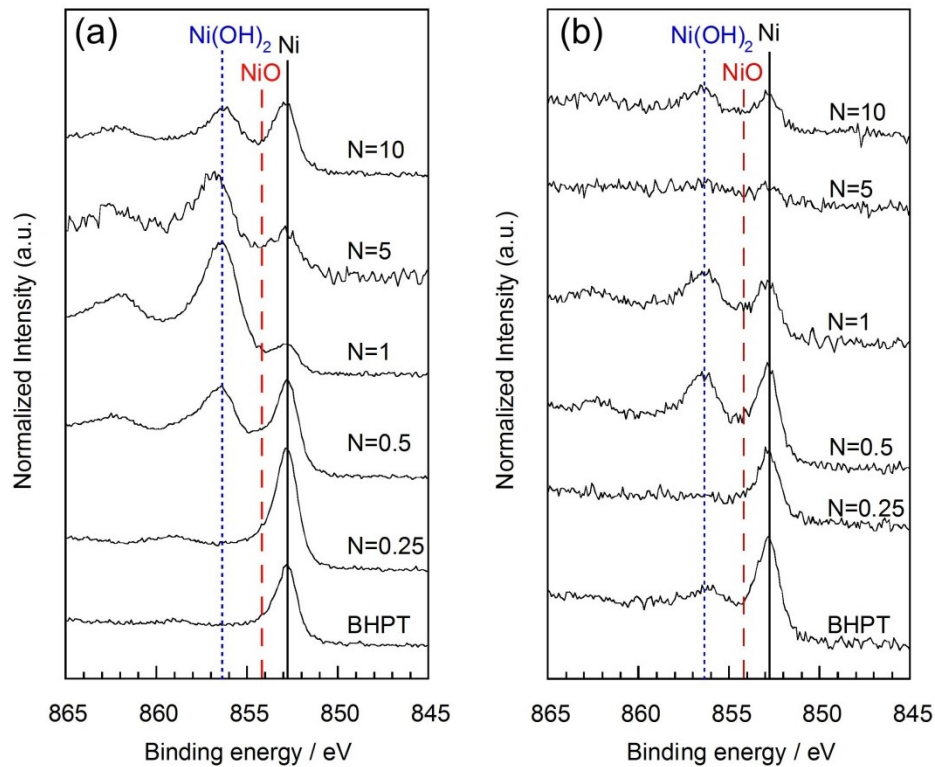


Fig. 4.7 Series of Ni 2p peaks of Ti-50mol%Ni (a) before and (b) after cell culture.

The ratio of the metallic-state to the oxide-state intensity of the XPS spectrum,  $\text{Ti}^{[\text{Me}]}/\text{Ti}^{[\text{Ox}]}$  for titanium and  $\text{Ni}^{[\text{Me}]}/\text{Ni}^{[\text{Ox}]}$  for nickel are presented in Fig. 4.8. The  $\text{Ni}^{[\text{Me}]}/\text{Ni}^{[\text{Ox}]}$  ratio is generally much larger than  $\text{Ti}^{[\text{Me}]}/\text{Ti}^{[\text{Ox}]}$ , as the formation of nickel oxide is thermodynamically less favorable than that of titanium oxides. Fig. 4.8(a) reveals a tendency of increase in  $\text{Ti}^{[\text{Me}]}/\text{Ti}^{[\text{Ox}]}$  with the number of turns in HPT ( $N$ ) except  $N = 1$ . As seen in Fig. 4.8(b), the  $\text{Ni}^{[\text{Me}]}/\text{Ni}^{[\text{Ox}]}$  value for the BHPT sample is 2 times larger than that of  $N = 0.25$  sample.  $\text{Ni}^{[\text{Me}]}/\text{Ni}^{[\text{Ox}]}$  value continued to decrease and stayed below 1 with further rotations. This shows that the metallic Ni on the surface of the sample decreases as more Ni is oxidized with increasing  $N$ .

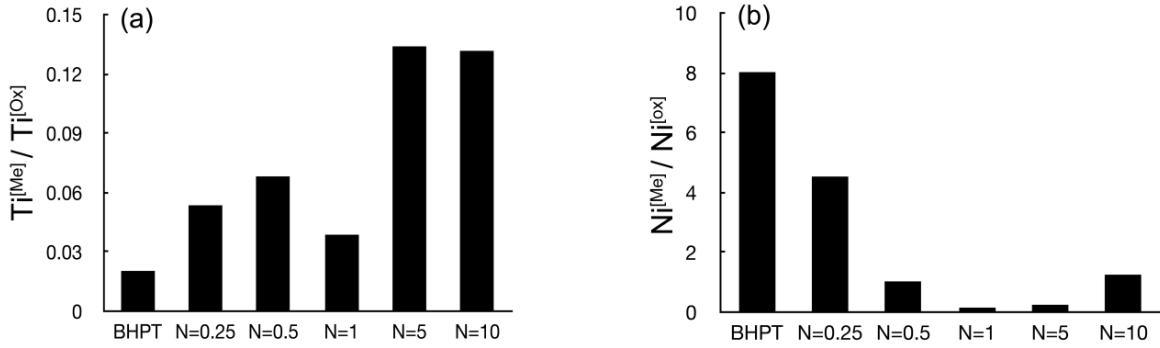


Fig. 4.8 Ratio of (a) $\text{Ti}^{[\text{Me}]} / \text{Ti}^{[\text{Ox}]}$  and (b)  $\text{Ni}^{[\text{Me}]} / \text{Ni}^{[\text{Ox}]}$  as function of HPT rotation of Ti-50mol%Ni .

Fig. 4.9 shows the N 1s peaks obtained from all the samples, which somewhat indicate protein adsorption since no N 1s peaks were detected on the surface before the cell culture[9]. The N 1s peak recorded at 400 eV is typical to nitrogen in organic matrix. Atomic fraction of nitrogen from the XPS gives the indication on the amount of protein adsorbed on the surface[16]. The detected amount of nitrogen is higher on the high rotation samples ( $N = 1, 5$  and  $10$ ) than BHPT and low rotation samples ( $N = 0.25$  and  $0.5$ ).

Table 4.3 Summary of contribution for each species from Ti-50mol% O1s and C1s spectra before and after cell culture

Sample	Percentage of species from O1s spectra						Percentage of species from C1s spectra					
	Before cell culture			After cell culture			Before cell culture			After cell culture		
	O <sup>2-</sup>	OH <sup>-</sup>	H <sub>2</sub> O	O <sup>2-</sup>	OH <sup>-</sup>	H <sub>2</sub> O	C-O	C=O	COOH	C-O	C=O	COOH
BHPT	63.51	27.41	9.08	49.34	21.64	29.02	82.72	8.26	9.02	72.69	19.54	7.77
<i>N</i> = 0.25	81.01	12.10	6.90	39.55	44.89	15.56	77.61	11.95	10.44	78.18	12.16	9.66
<i>N</i> = 0.5	28.51	30.11	41.38	46.89	28.93	24.18	79.55	14.30	6.15	61.64	30.85	7.52
<i>N</i> = 1	47.88	30.67	21.45	44.48	28.55	26.97	71.94	20.72	7.34	55.46	28.39	16.15
<i>N</i> = 5	13.60	31.75	54.65	34.16	40.93	24.91	80.33	12.38	7.29	56.41	28.96	14.63
<i>N</i> = 10	49.95	42.30	7.75	32.64	35.39	31.97	60.20	31.61	8.19	60.10	28.69	11.21

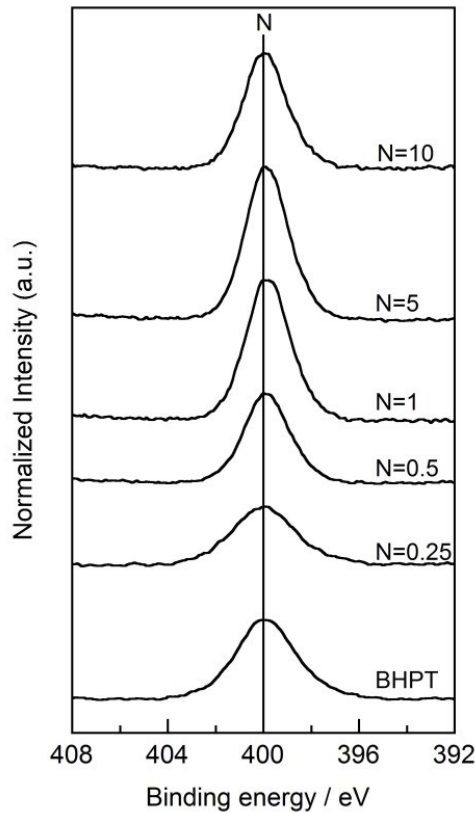


Fig. 4.9 Series of N 1s peaks of Ti-50mol%Ni after cell culture.

*Depth profiles analysis.* Depth profiles of BHPT,  $N = 0.25$  and  $N = 5$  samples prior to cell culture are shown in Fig. 4.10. For all the samples, titanium concentration was around 30 at% in steady-state due to the preferential sputtering of titanium while nickel concentration was around 50 at%. The oxygen concentration was at the maximum at the surface and steadily decreased with the depth from the surface. For the BHPT sample (Fig. 4.10(a)), the passive film thickness was found to be 5 nm. For  $N = 0.25$  (Fig. 4.10(b)), the passive film thickness was found to be 12.65 nm. The plateaus of the O and Ti profiles near the surface indicate that protective  $\text{TiO}_2$  covered the surface of the sample. For  $N = 5$  (Fig. 4.10(c)), the passive film thickness was found to be 9 nm. The oxygen profile shows the maximum at the surface and a slight stepwise change until 150 s of sputtering before a steady decrease in concentration. The Ni depth profile shows a plateau from the surface until 150 s of sputtering before a steady increase to a steady state.

Fig. 4.11 shows the depth profile of BHPT,  $N = 0.25$  and  $N = 5$  samples after to cell culture. For BHPT and  $N = 0.25$ , the depth did not change much. This may be due to the protectiveness of the  $\text{TiO}_2$  form initially on the surface. However, increase in the thickness of the surface oxide of the  $N = 5$  sample after cell culture was observed.

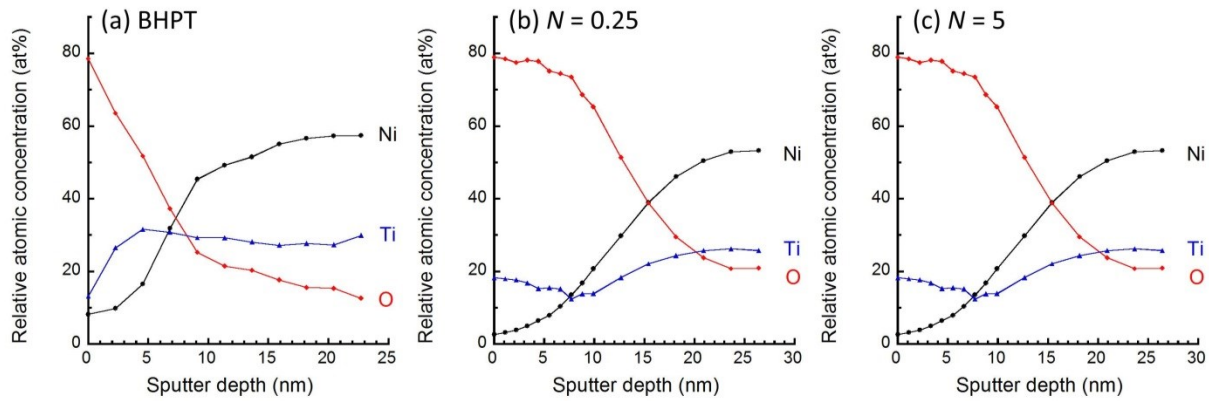


Fig. 4.10 Depth profile for (a) BHPT, (b)  $N = 0.25$  and (c)  $N = 0.25$  before cell culture.

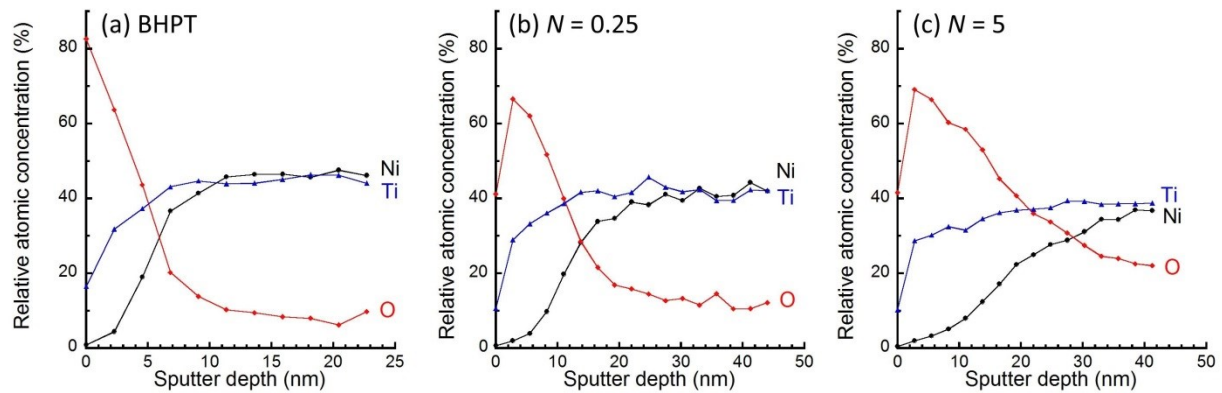


Fig. 4.11 Depth profile for (a) BHPT, (b)  $N = 0.25$  and (c)  $N = 0.25$  after cell culture.

### 4.3.2 Surface characterization of Ti-50.9mol%Ni

Chemical compositions of the passive films on the TiNi sample surfaces before the cell culture were obtained from XPS spectra, as presented in Table 4.4. The major elements detected are carbon, oxygen, titanium, and nickel. The samples were dominated by carbon and oxygen. The range of total Ti/Ni ratio was 2.32-11.64, which indicates highly enriched titanium at the surface. Further examination of metallic Ni to metallic Ti ratio shows excess of metallic Ni in all samples except  $N = 10$ . This is expected since the composition of the alloys used is slightly rich in Ni as Ti-50.9 mol%Ni.

Table 4.5 shows the elemental compositions on the surface after the cell culture. Additional element, nitrogen, was detected besides the four elements shown in Table 1. The increase in the total Ti/Ni ratio is observed in all samples after the cell culture. This observation can be attributed to the enrichment of Ti on the surface, but high resolution spectra of Ni 2p after the cell culture is too weak to properly quantify the Ti/Ni ratio.

Table 4.4 Chemical composition of the Ti-50.9mol%Ni surface samples as measured by XPS

Sample	Atomic concentration (at%)				$\text{Ni}^{[\text{Me}]}/\text{Ti}^{[\text{Me}]}$	Ti/Ni
	C1s	Ti2p	O1s	Ni2p		
BHPT	58.29	2.28	38.68	0.75	1.60	3.05
$N = 0.25$	68.54	2.53	27.83	1.09	1.52	2.32
$N = 0.5$	51.37	5.45	42.72	0.47	1.49	11.64
$N = 1$	56.32	1.96	40.89	0.82	1.48	2.38
$N = 5$	31.07	6.24	60.77	1.92	1.92	3.25
$N = 10$	49.63	3.51	45.54	1.33	1.07	2.64

Table 4.5 Chemical composition of the Ti-50.9mol%Ni surface samples after cell culture as measured by XPS

Sample	Atomic concentration (at%)					Ti/Ni
	C1s	Ti2p	O1s	Ni2p	N1s	
BHPT	51.70	3.03	34.37	0.22	10.68	13.66
$N = 0.25$	60.91	1.14	28.66	0.26	9.04	4.43
$N = 0.5$	57.56	2.30	34.90	0.37	4.87	6.14
$N = 1$	52.42	2.34	34.57	0.37	10.30	6.32
$N = 5$	54.13	2.44	31.86	0.38	11.19	6.45
$N = 10$	67.86	0.60	21.84	0.21	9.49	2.81

*C 1s spectra.* The C 1s peak obtained from all the samples before and after the cell culture was shown in Fig. 4.12 (a) and (b), respectively. The spectra were further deconvoluted into 3 peaks: 285 eV (C-C, C=C or C-H), 286.5 eV (C-O or C-N) and 288.4 eV (carboxyl or amide group) [5]. Since none of the carbon peaks were detected at the higher energy binding region, it was concluded that the carbon on the surface originated from not chemically bind but physically adsorbed organic molecules as contaminants [6-8]. Even after the cell culture, the C 1s spectrum is still dominated by the peak at 285 eV but there is observable increase at the highest binding energy (288.4 eV) which corresponds to carboxyl or amide groups. This increase suggests the adsorbed organic compounds such as proteins, amino acids, and carbohydrates during the cell culture [3,10].

Fig. 4.13 shows the series of normalized O 1s spectra with three peaks at 530, 531.5, and 533.2 eV, which correspond to oxide group ( $O^{2-}$ ), hydroxyl group (OH), and chemisorbed water  $H_2O$ , respectively. Before the cell culture (Fig. 4.13(a)), broad O 1s peaks were observed in all samples except  $N = 0.5$  and 5, which had a strong peak at the binding energy corresponding to  $O^{2-}$ . After the cell culture (Fig. 4.13(b)), only BHPT samples show a strong peak corresponding to  $O^{2-}$ . The HPT deformed samples show peak shifting toward the higher binding energy.  $N = 0.25$  and 10 showed a strong peak at the energy corresponding to the chemisorbed  $H_2O$ .

*Ti 2p spectra.* High resolution XPS of the Ti 2p spectra reveals the major peaks at binding energies at 459 eV and 465 eV, which corresponds to Ti 2p<sub>3/2</sub> and Ti 2p<sub>1/2</sub> states of the stoichiometric  $TiO_2$  ( $Ti^{4+}$ ). Further deconvoluted peaks show a doublet at 454.8 eV (Ti 2p<sub>3/2</sub>) and 460.4 eV (Ti 2p<sub>1/2</sub>) which correspond to metallic Ti ( $Ti^{[Me]}$ ) in the substrate [11,12]. It is expected to detect  $Ti^{[Me]}$  originated from the substrate since passive film formation at room temperature for TiNi typically reaches the equilibrium at around 3 nm [13]. Examination of the high resolution spectra of the Ti 2p region after the cell culture shows the major peak at  $Ti^{4+}$ . The surface is completely covered by  $TiO_2$  as there is no metallic Ti ( $Ti^{[Me]}$ ) detected from the XPS spectra.

*Ni 2p spectra.* Fig. 4.14 (a) and (b) shows a series of Ni 2p spectra before and after the cell culture, respectively. In Fig. 4 (a), two main peaks at 853 eV and 856.3 eV, which correspond to the metallic Ni ( $Ni^{[Me]}$ ) and  $Ni(OH)_2$  [11,13,14], were detected on all surfaces. After the cell culture, only BHPT sample shows a strong peak of  $Ni^{[Me]}$  while in deformed samples, the main peak has shifted to higher binding energy corresponding to  $Ni(OH)_2$ .

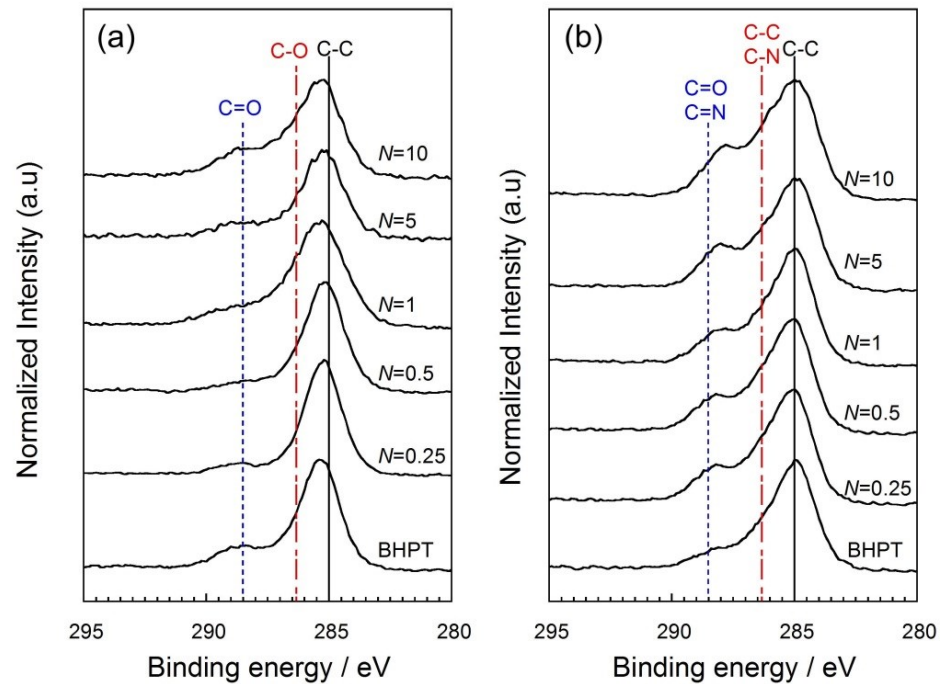


Fig. 4.12 Series of C 1s peaks of Ti-50.9mol%Ni (a) before and (b) after cell culture.

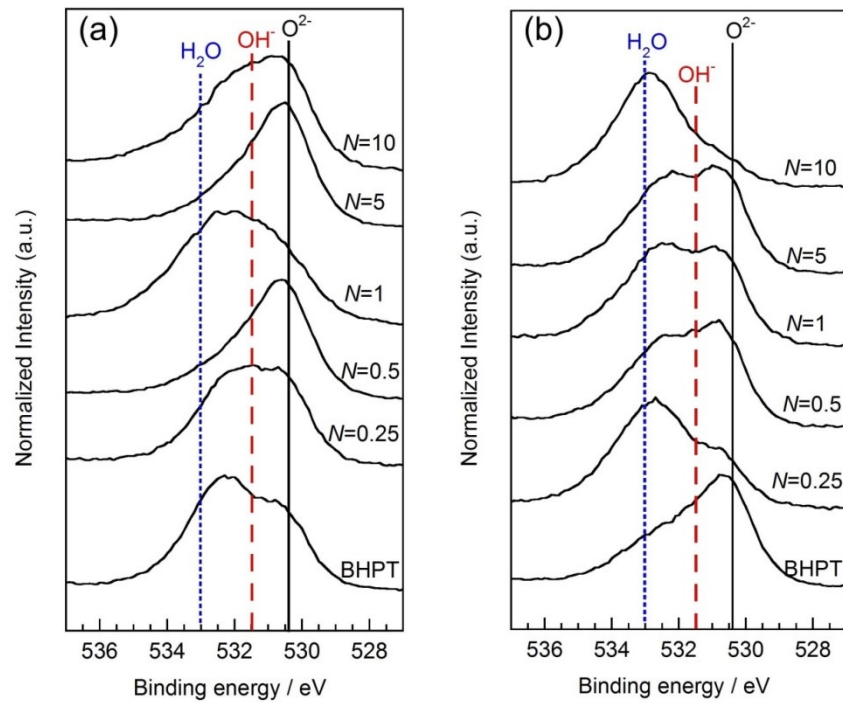


Fig. 4.13 Series of O1s peaks of Ti-50.9mol%Ni (a) before and (b) after cell culture.

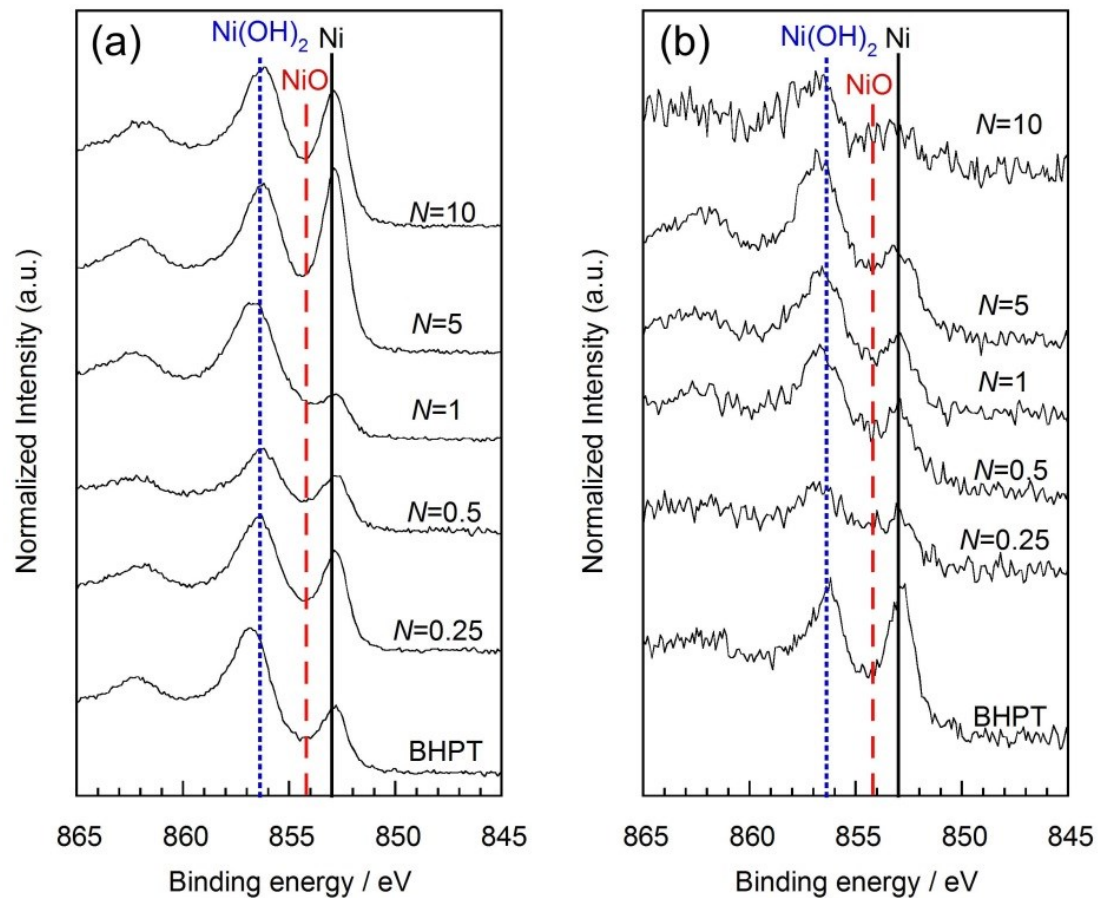


Fig. 4.14 Series of Ni 2p peaks of Ti-50.9mol%Ni (a) before and (b) after cell culture.

Table 4.6 Summary of contribution for each species from Ti-50mol% O1s and C1s spectra before and after cell culture

Sample	Percentage of species from O1s spectra						Percentage of species from C1s spectra					
	Before cell culture			After cell culture			Before cell culture			After cell culture		
	O <sup>2-</sup>	OH <sup>-</sup>	H <sub>2</sub> O	O <sup>2-</sup>	OH <sup>-</sup>	H <sub>2</sub> O	C-O	C=O	COOH	C-O	C=O	COOH
BHPT	40.91	37.59	21.50	47.35	29.39	23.26	58.00	26.10	15.90	72.69	19.54	7.77
N = 0.25	53.22	31.62	15.16	28.18	47.63	24.19	67.49	24.67	7.83	78.18	12.16	9.66
N = 0.5	57.90	24.25	17.85	27.07	41.12	31.82	53.81	39.08	7.12	58.70	33.21	8.09
N = 1	33.91	37.02	29.06	42.84	32.55	24.60	55.52	29.57	14.91	49.90	33.11	16.98
N = 5	56.89	28.25	14.87	45.53	31.94	22.52	74.90	13.40	11.70	53.35	30.99	15.66
N = 10	47.04	34.14	18.82	27.90	49.74	22.36	69.99	14.06	15.95	57.00	30.92	12.08

*N 1s spectra.* The N 1s peaks obtained from all the surface of Ti-50.9mol%Ni after the cell culture is shown in Fig. 4.15 are originated from the adsorbed biomolecules since no N 1s peaks were detected on the surface before the cell culture. The N 1s peak recorded at 400 eV is typical to nitrogen in organic matrix [16].

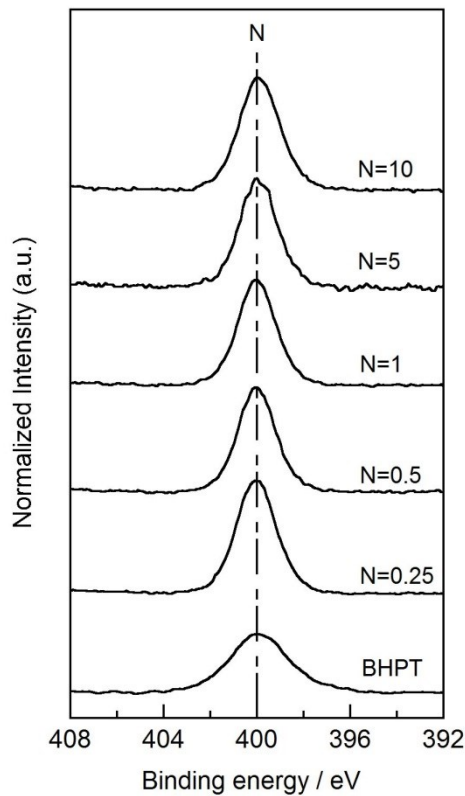


Fig. 4.15 Series of N 1s peaks of Ti-50.9mol%Ni after cell culture.

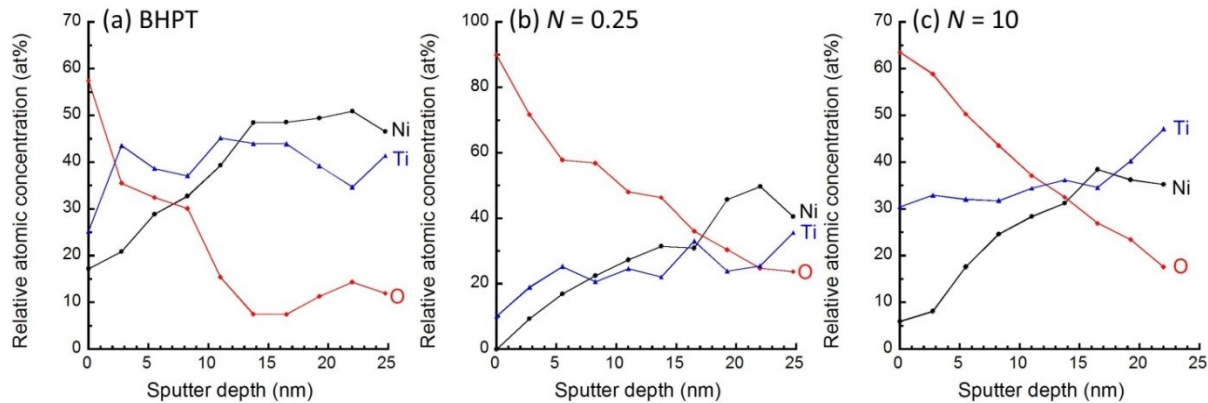


Fig. 4.16 Depth profile of Ti-50.9 mol%Ni for (a) BHPT, (b)  $N = 0.25$  and (c)  $N = 0.25$  before cell culture.

*Depth profiles analysis.* Depth profiles of BHPT,  $N = 0.25$  and  $N = 10$  samples prior to cell culture are shown in Fig. 4.16. For all the samples, titanium concentration was around 30 at% in steady-state due to the preferential sputtering of titanium while nickel concentration was around 50 at%. The oxygen concentration was at the maximum at the surface and steadily decreased with the depth from the surface. For the BHPT sample (Fig. 4.16 (a)), the passive film thickness was found to be 9 nm. For  $N = 0.25$  and  $N=10$ , as shown in Fig. 4.16 (b) and (c) respectively, the passive film thickness was found to be at 14 nm.

## 4.4 Discussion

### 4.4.1 Effect of HPT on the surface composition of TiNi

The corrosion behavior and ion release from TiNi are dependent on the surface conditions. Although TiNi contains a high amount of Ni, its good biocompatibility is mainly due to the protective inert Ti oxides on the surface as well as strong bonding between Ti and Ni atoms. Spontaneous formation of  $\text{TiO}_2$  on the surface of TiNi is driven by the higher formation energy of  $\text{TiO}_2$  (-956 kJ mol<sup>-1</sup> [17]), compared to that of  $\text{Ni(OH)}_2$  (-529.7 kJ mol<sup>-1</sup> [18]) and  $\text{NiO}$  (-241 kJ mol<sup>-1</sup> [17]). The formation of  $\text{TiO}_2$  is accommodated by oxygen migration towards NiTi substrates and Ni migration towards the surface. As the oxidation progresses, O atoms diffuse inwards [19].

Several studies on the oxidation of TiNi by heat treatment or by chemical surface treatment revealed that the preferential formation of  $\text{TiO}_2$  on TiNi surface caused Ni enrichment underneath the surface oxide layer, resulting in the increased Ni ion release [20,21].

A high density of dislocations, grain refinement and amorphization induced by HPT in TiNi influences the formation of passive film on TiNi. Investigation of passive films formed on the Ti-50mol%Ni surface showed a change in the chemical composition of the films. Most striking observation in the XPS data was the continuous decrease of metallic Ni enrichment in the passive film with HPT rotation. Further analysis of the ratio of proportion of metallic Ni to metallic Ti on Ti-50mol%Ni surface prior to cell culture, as shown in Fig. 4.17, supports this observation. As the metallic component is expected to come from the substrate, this ratio should be 1. However, in BHPT, the ratio of  $\text{Ni}^{[\text{Me}]}/\text{Ti}^{[\text{Me}]}$  is 3.96, indicating an enrichment of Ni on the sample surface. HPT samples show decrease in the  $\text{Ni}^{[\text{Me}]}/\text{Ti}^{[\text{Me}]}$  ratio along HPT rotation, showing almost no Ni enrichment on the surface. The atomic concentration of metallic Ni obtained from XPS peak intensities also decreases with the number of HPT rotations as shown in Fig. 4.7(a).

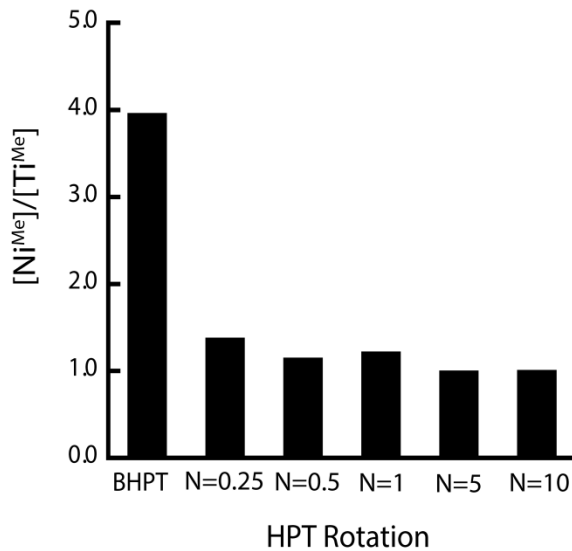


Fig. 4.17 Ratio of proportion of the metallic Ni to metallic Ti on the film oxide of Ti-50mol%Ni as the function of HPT rotation.

#### 4.4.2 Effect of HPT on the TiNi passive film formation

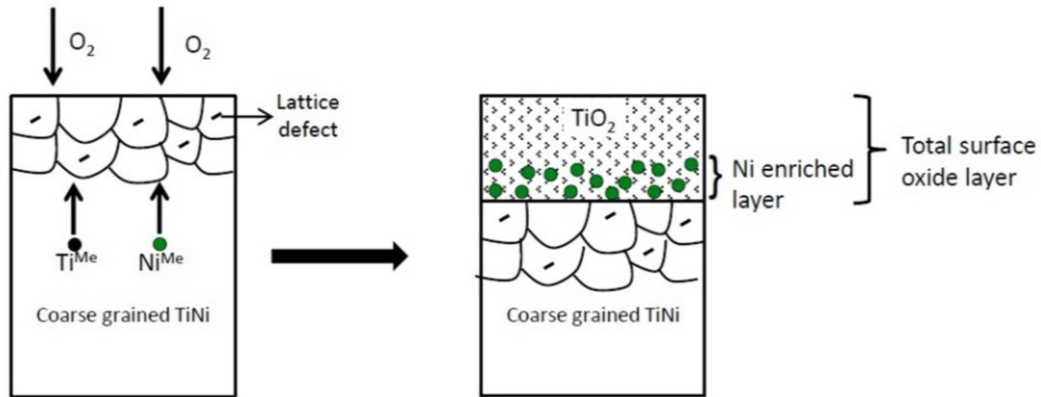
Another interesting observation was even though the atomic concentration of the HPT deformed samples did not vary much to BHPT sample, the constituent of the passive film of HPT deformed is not only composed of  $\text{TiO}_2$  but also  $\text{Ni(OH)}_2$ . A study by Qin et. al have found out that XPS examination on nanocrystalline Ni passive film shows the passive layer mainly composed of stable and continuous  $\text{Ni(OH)}_2$ , leading to better corrosion resistance in comparison to coarse grain Ni [22]. Formation of high

fraction of passive layer is due to the higher grain boundary density, which increase the electrochemical reactivity during the corrosion process.

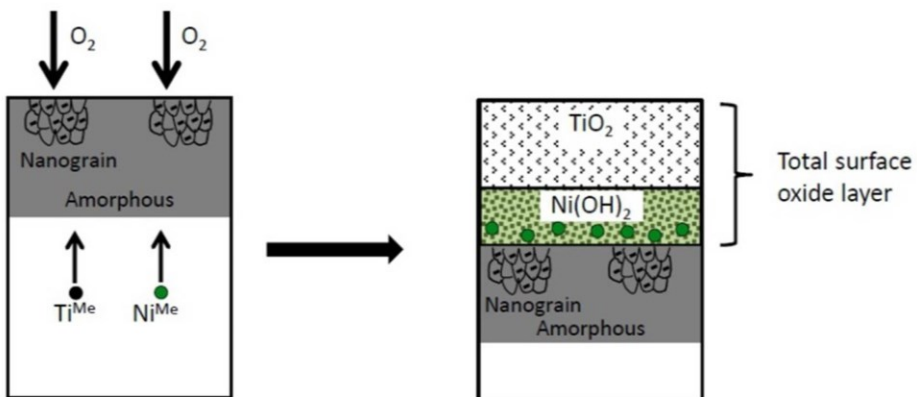
Schematic illustrations of passive film formation on the surface of BHPT and HPT deformed samples are shown in Fig. 4.18. In BHPT TiNi (Fig. 4.18(a)), the preferential oxidation of Ti has left behind metallic Ni underneath the oxide layer, forming a Ni enriched layer. The Ni enriched layer retarded further oxidation of Ti as it acts as a diffusion barrier for Ti in the substrate leading to a thin oxide layer (Fig. 7(a)) [23] and the high Ni content underneath the thin oxide layer (Fig. 5(b)). The Ni enrichment is detrimental to the biocompatibility of the TiNi since it may act as a reservoir for the continuous Ni ion release especially when the TiNi was immersed in a body fluid. Furthermore, as the size of Ni atom is smaller than that of Ti underneath the surface oxide, this Ni may readily diffuse out from the defective oxide layer [24].

Fig. 4.18 (b) and (c) shows a schematic illustration of passive film formation on the HPT deformed samples consisting of a mixture of nanocrystalline and amorphous structure. The decrease in Ni enrichment and the increase in the passive film thickness in HPT deformed TiNi can be explained as follows. The increase in dislocation density and nanocrystallization by HPT helps to eliminate the Ni enrichment layer by changing the kinetics of passive film formation. In smaller HPT rotation ( $N = 0.25$  and  $0.5$ ), high density of dislocations and nanocrystalline grains are major constituents of the microstructures. Increasing the density of dislocations allows the formation of thicker protective  $\text{TiO}_2$  layer on the sample surface as evidenced in Fig. 4.18 (b). As the number of rotation increases, the volume fractions of the amorphous phase increases, leading to thinner layer of  $\text{TiO}_2$  than smaller HPT rotation. However, the passive film thickness on high rotation samples still increased when compared to BHPT due to formation of  $\text{Ni(OH)}_2$  beneath the  $\text{TiO}_2$  layer. Appearance of new peak in  $\text{Ni } 2\text{p}_{3/2}$  and  $\text{O } 1\text{s}$  spectra were observed, indicating the change of Ni oxidation states in the passive film from metallic Ni to  $\text{Ni(OH)}_2$ . High defect density and structural/chemical disorder in the amorphous region allow faster transport of point defects, which accelerate the passive film formation kinetics [25] and facilitate the formation of an uniform passive oxide layer. Defects also allow the increase in Ni and Ti cations to compensate excess vacancies on the surface layer [14]. The high defect density also increases the diffusivity of metal Ni into the passive film, where metallic Ni reacts with O to produce  $\text{NiO}$  and  $\text{Ni(OH)}_2$ . Furthermore, an increase in the defect density makes the surface more reactive, which encourages the chemisorption of the water and hydroxide, as shown in Table 2 as a general tendency [17]. Continuous supply of metal vacancies by the defects in HPT deformed samples explains the continuous oxidation during passive film formation, hence the thicker passive film [26,27]. All of these behaviors contribute to increase passive film thickness and to decrease Ni enrichment beneath the surface in HPT samples.

(a) Before HPT



(b) After HPT (low rotation)



(c) After HPT (high rotation)

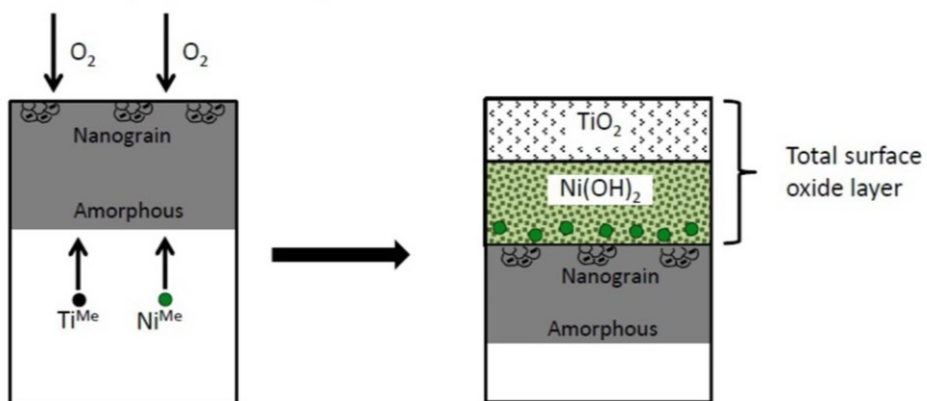


Fig. 4.18 Schematic illustration of passive film formation.

#### 4.4.3 Effect of cell culture to the passive film in TiNi

Although metal has been used as an implant material, there is some concern regarding its usage for long term usage as it will undergoes corrosion or generate particulate debris from abrasion. The corrosion of the metal in the host also cause premature structural failure and accelerated releases of metal particles and ions. Metal ion release may lead to hypoallergenic and carcinogenic effect. The concern in metal usage as an implant is due to the corrosion of the metal inside the body due to the interaction between the physiological fluid and cell with the metal surface. Since surface phenomena play a critical role in biological performance, thus the behavior of TiNi surfaces in the biological environment needs to be critically evaluated.

After cell culture, relative concentration of each species in C 1s, Ni 2p and O 1s spectra was observed to change, an indication of a dynamic surface. The changes were more prominent in the HPT deformed samples. In both alloys, the C 1s spectra shows increase in the C=O and carboxyl group peaks. The increase in these two components may be attributed to the adsorption of organic constituents [28]. In the O 1s spectra, the shift of binding energy from O<sup>2-</sup> to higher binding energy (OH<sup>-</sup> and H<sub>2</sub>O) was observed with more distinct change in sample undergoes higher rotation.

### **4.5 Conclusion**

The decrease in Ni enrichment in HPT samples suggests suppression of Ni ion release when it is implanted in the human body. The thicker oxide film formation on the HPT samples is also a positive factor for the improvement of corrosion resistance in the biological fluid. Changes in the chemical composition in the passive oxide film of HPT samples also suggest the possibility to influence the cellular response on the sample surface since cellular reaction depends on the kind, amount and conformation of adsorbed proteins onto materials surface. Therefore Ni release, corrosion resistance, cellular response and protein adsorption behavior is another important field for investigation.

#### 4.6 References:

- [1] Briggs D, Seah MP. Practical surface analysis by Auger and X-ray photoelectron spectroscopy. D. Briggs, & M. P. Seah,(Editors), John Wiley & Sons, Chichester 1983, xiv+ 533; 1983.
- [2] Nie FL, Zheng YF, Cheng Y, Wei SC, Valiev RZ. In vitro corrosion and cytotoxicity on microcrystalline, nanocrystalline and amorphous NiTi alloy fabricated by high pressure torsion. Mater. Lett. 2010;64:983–6.
- [3] Hang R, Ma S, Ji V, Chu PK. Corrosion behavior of NiTi alloy in fetal bovine serum. Electrochim. Acta 2010;55:5551–60.
- [4] Shabalovskaya SA, Tian H, Anderegg JW, Schryvers DU, Carroll WU, Van Humbeeck J. The influence of surface oxides on the distribution and release of nickel from Nitinol wires. Biomaterials 2009;30:468–77.
- [5] Ithurbide A, Frateur I, Galtayries A, Marcus P. XPS and flow-cell EQCM study of albumin adsorption on passivated chromium surfaces: Influence of potential and pH. Electrochim. Acta 2007;53:1336–45.
- [6] Faghihi S, Azari F, Zhilyaev AP, Szpunar J, Vali H, Tabrizian M. Cellular and molecular interactions between MC3T3-E1 pre-osteoblasts and nanostructured titanium produced by high-pressure torsion. Biomaterials 2007;28:3887–95.
- [7] Hanawa T, Hiromoto S, Asami K, Okuno O, Asaoka K. Surface oxide films on titanium alloys regenerated in Hanks' solution. Mater. Trans. JIM 2002;43:3000–4.
- [8] Hiromoto S, Kano K, Suzuki Y, Asami K, Chiba A, Hanawa T. Surface characterization and anodic polarization of nitrogen-ion-implanted nickel-free Co-Cr-Mo alloy. Mater. Trans. JIM 2005;46:1627–32.
- [9] Awang Shri DN, Tsuchiya K, Yamamoto A. Surface characterization of TiNi deformed by high-pressure torsion. App. Surf. Sci. 2014;289:338–44.
- [10] Deligianni DD, Katsala N, Ladas S, Sotiropoulou D, Amedee J, Missirlis YF. Effect of surface roughness of the titanium alloy Ti-6Al-4V on human bone marrow cell response and on protein adsorption. Biomaterials 2001;22:1241–51.
- [11] Asami K, Chen SC, Habazaki H, Hashimoto K. The surface characterization of titanium and titanium-nickel alloys in sulfuric acid. Corros. Sci. 1993;35:43–9.
- [12] Trepanier C, Pelton AR. Effect of strain on the corrosion resistance of nitinol and stainless steel in simulated physiological environment. Medical Device Materials: Proceedings From the Materials & Processes for Medical Devices Conference 2003, 8-10 September 2003, Anaheim, California 2004:176.
- [13] Armitage DA, Grant DM. Characterisation of surface-modified nickel titanium alloys. Mater. Sci. Eng. A 2003;349:89–97.
- [14] Rofaghah R, Splinter SJ, Erb U, McIntyre NS. XPS characterization of the passive films formed on nanocrystalline nickel in sulphuric acid. Nanostruct. Mater. 1994;4:69–78.
- [15] Luo PF, Kuwana T, Paul DK, Sherwood PM. Electrochemical and XPS Study of the Nickel-Titanium Electrode Surface. Anal. Chem. 1996;68:3330–7.
- [16] Ray S, Shard AG. Quantitative Analysis of Adsorbed Proteins by X-ray Photoelectron Spectroscopy. Anal. Chem. 2011;83:8659–66.
- [17] Green S, Grant D, Wood J. XPS characterisation of surface modified Ni-Ti shape memory alloy. Mater. Sci. Eng. A 1997;224:21–6.
- [18] Wagman DD, Evans WH, Parker VB, Schumm RH, Halow I. The NBS tables of chemical thermodynamic properties. Selected values for inorganic and C1 and C2 organic substances in SI units 1982.
- [19] Milošev I, Kapun B. The corrosion resistance of Nitinol alloy in simulated physiological solution Part 1: The effect of surface preparation. Mater. Sci. Eng. C 2011.
- [20] Tian H, Schryvers D, Shabalovskaya S, Van Humbeeck J. Microstructure of Surface and Subsurface Layers of a Ni-Ti Shape Memory Microwire. Mam 2009;15:62.

- [21] Chan CM, Trigwell S, Duerig T. Oxidation of an NiTi alloy. *Surf. Interface Anal.* 1990;15:349–54.
- [22] QIN L-Y, LIAN J-S, Jiang Q. Effect of grain size on corrosion behavior of electrodeposited bulk nanocrystalline Ni. *Transactions of Nonferrous Metals Society of China* 2010;20:82–9.
- [23] Firstov GS, Vitchev RG, Kumar H, Blanpain B, Van Humbeeck J. Surface oxidation of NiTi shape memory alloy. *Biomaterials* 2002;23:4863–71.
- [24] Schroeder V. Evolution of the passive film on mechanically damaged nitinol. *J. Biomed. Mater. Res.* 2009;90A:1–17.
- [25] Macdonald DD. The point defect model for the passive state. *J. Electrochem. Soc.* 1992;139:3434–49.
- [26] Yamamoto T, Fushimi K, Miura S, Konno H. Effect of Cold Rolling on Passive Film on Pure Iron in pH 8.4 Borate Buffer Solution. *ECS Transactions* 2010;25:3–15.
- [27] Liu L, Li Y, Wang FH. Electrochemical corrosion behavior of nanocrystalline materials-a review. *J. Mater. Process. Tech.* 2010;26:1–14.
- [28] Hanawa T, Hiromoto S, Yamamoto A, Kuroda D, Asami K. XPS characterization of the surface oxide film of 316L stainless steel samples that were located in quasi-biological environments. *Mater. Trans. JIM* 2002;43:3088–92.



## **Chapter 5 Electrochemical Characterization of TiNi alloys Deformed by High Pressure Torsion**

### **5.1 Introduction**

Biocompatibility of a metal heavily depends on its corrosion resistance. Corrosion of a TiNi implant is highly concern because of the Ni ion release that has negative effect on the surrounding tissue, inducing allergic response and carcinogenesis. The mechanical failures of implants also might happen as a result of corrosion.

On the study of surface modification being proven to reduce the Ni ion release, it has been established that the uniformity, not thickness, of the passive oxide layer is more important to prevent TiNi from corrosion [1,2]. HPT deformation produced nanostructured materials consists of nanograins and amorphous region. The change in the structure (small grain size and high-volume fraction of grain boundaries) of the material may result in the different corrosion behavior from that of the coarse-grained material. Although TiNi has a good corrosion resistance due to the protective passive film which primarily composed of  $\text{TiO}_2$ , the change in the microstructure may influence the corrosion behavior of TiNi.

Potentiodynamic test in a physiological fluid provides a fast overview in understanding the general corrosion behavior of metallic biomaterials [3]. As most of metallic biomaterials are passivating alloys, the corrosion behavior of the alloy can be predicted based on the its polarization curve.

In this section, the focus is on the electrochemical behavior of TiNi alloys when they are exposed to the cell culture medium. Electrochemical measurements were done to understand the corrosion behavior of TiNi alloys before and after HPT deformation. The changes in the corrosion resistance of the samples and the changes in passive behavior are discussed.

## **5.2 Experimental Methods**

### **5.2.1 Sample preparation**

The samples were prepared and polished as described in Section 2.2.1. The polished samples were then cleaned ultrasonically for 15 min in acetone. The sample disks were sterilized using ethylene oxide gas (EOG) for 23 hrs. at 44 °C.

### **5.2.2 Electrochemical measurements**

Electrochemical measurements were carried out using a standard three electrode setup (a sample as a working electrode; a platinum wire as a counter electrode and a silver/silver chloride in saturated KCl as a reference electrode with the surface area of 26.42 mm<sup>2</sup> exposed to the cell culture medium, EMEM+FBS. Fig. 5.1 shows the corrosion cell set up used in the potentiodynamic test. The measurements were performed in an incubator with controlled environment at 37°C and 5% CO<sub>2</sub>, a cell culture incubation condition. The cell culture medium is settled in the CO<sub>2</sub> incubator for 24 hours prior to the measurement to adjust its pH by dissolving and dissociation of CO<sub>2</sub>. The potential of the specimen was monitored over 1 hour, and the stabilized potential was used as the open-circuit potential (OCP). Potentiodynamic curves were scanned in the potential range from -0.5 V to 1.5 V relative to the OCP, at a rate of 0.5 mV/s. The potentiodynamic test were done using a VersaSTAT potentiostat, with running VersaStudio software (Princeton Applied Research, Oak Ridge, USA). Potentiodynamic polarization plots were used to calculate the corrosion potential ( $E_{corr}$ ) and corrosion current density ( $i_{corr}$ ) for all the samples using the Tafel extrapolation method. Other corrosion parameter relating to the passive behavior of the samples such as passive current density ( $i_{pass}$ ), primary passive potential ( $E_p$ ), and the critical current density ( $i_c$ ) at  $E_p$  can be extracted from the curve.

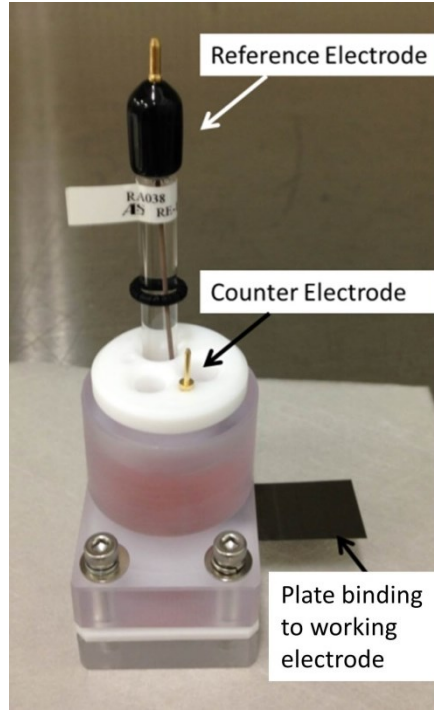


Fig. 5.1 Electrochemical cell setup used in this experiment.

### 5.3 Results

#### 5.3.1 OCP Measurement

The result of OCP-time measurement done in the cell culture medium is shown in Fig. 5.2(a) and Fig. 5.2(b) for Ti-50 mol%Ni and Ti-50.9 mol%Ni respectively. It can be seen that for alloys, the OCP of HPT-deformed samples shifts towards to more positive rather than that of BHPT samples. In Ti-50mol%Ni, the BHPT sample shows some decrease in OCP before finally stabilized at around 750s, indicating active dissolution of the passive film in cell culture media. The HPT deformed samples, on the other hand, stabilized almost immediately upon immersion. The OCP of deformed Ti-50mol%Ni samples were ennobled to more than +70 mV. In Ti-50.9mol%Ni, the OCP of BHPT sample decreases before stabilized after 800 s. The observed decrease in OCP may be due to the attenuation of the air-formed passive film upon immersion in cell culture medium. On the other hand, the OCP of N=1 and N=5 samples shows some increase in potential before stabilized, indicating the formation and growth of further passive film upon immersion in cell culture medium. The other HPT-deformed samples stabilized almost immediately. The OCP of deformed samples ennobled to more than +200 mV for Ti-50.9 mol%Ni. The shift of OCP towards the nobler direction indicates the passive nature of native oxides formed on the surface of the samples.

### 5.3.2 Polarization curves

The potentiodynamic polarization curves for Ti-50 mol%Ni and Ti-50.9 mol%Ni are shown in Fig. 5.3(a) and Fig. 5.3(b) respectively. All samples show the typical passive behavior. HPT-deformed samples of both TiNi alloys have a nobler corrosion potential ( $E_{corr}$ ) and a lower corrosion current ( $i_{corr}$ ) than BHPT samples. These results suggest that the corrosion resistance of TiNi alloys is improved after HPT deformation. Several important parameters, such as steady state passive current density ( $i_{ss}$ ) and the breakdown potential ( $E_{bd}$ ) are extracted from the curves and shown in Table 5.1 and Table 5.2 for Ti-50mol%Ni and Ti-50.9mol%Ni respectively. The steady state passive current density is marks as  $i_{ss}$  while the potential at which the passive film starts to breakdown is denoted as  $E_{bd}$ .

For Ti-50 mol%Ni, a current plateau established spontaneously in the BHPT samples at around 0.3 V indicating the presence of passive region in the solution. The  $i_{ss}$  of BHPT was found to be the highest. The HPT deformation was found to shift down the passive region to nobler region, suggesting the higher activity of the sample surface in the cell culture medium. In the HPT-deformed samples, more pronounced anodic peak corresponds to the start of active-passive transition was observed. The passive range in the deformed samples were slightly inclined until it reached constant between 0.6-0.8 V indicating further passive film formation in the cell culture medium. The passive region current density is found to be lower than that of the BHPT, suggesting the passive film formed on the surface of HPT-deformed samples is more protective than that of the BHPT sample. A sudden increase in current density around 1-1.2 V denotes the breakdown of the passive range and the initiation of localized pitting corrosion. However, the pitting potential of all samples are almost identical, suggesting that the pitting resistance of TiNi does not change after HPT deformation. Nonetheless, the pitting potential occur more than 1 V from their open circuit potential, suggesting that the spontaneous pitting corrosion will not happen in the cell culture medium. The corrosion behavior of Ti-50.9 mol%Ni shown in Fig. 5.3(b) denotes the same trend observed in Ti-50 mol%Ni. The passive range of HPT deformed Ti-50.9 mol%Ni tended to be smaller than those of Ti-50mol%Ni.

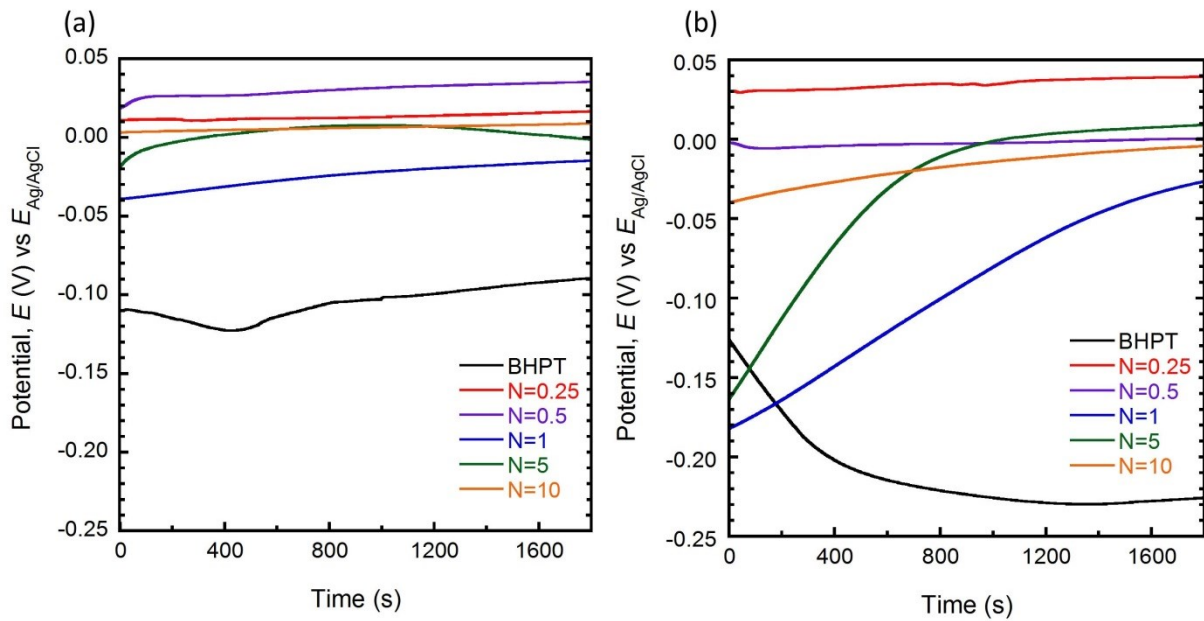


Fig. 5.2 Open circuit potential of (a) Ti-50mol%Ni and (b) Ti-50.9 mol%Ni in cell culture media.

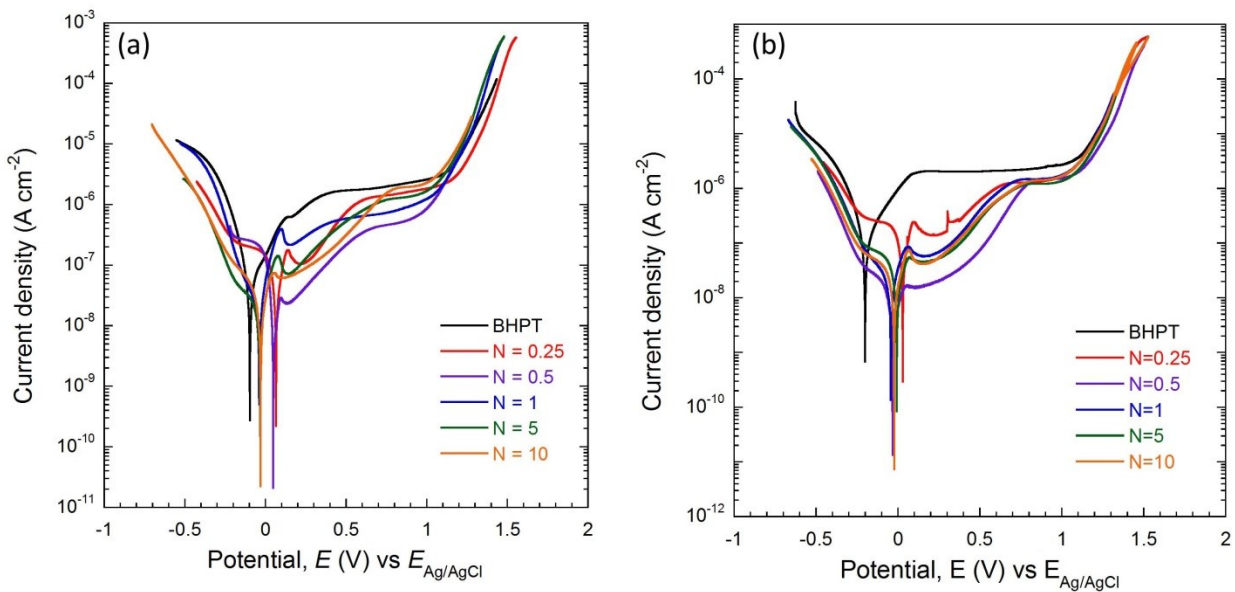


Fig. 5.3 The potentiodynamic polarization of (a) Ti-50mol%Ni and (b) Ti-50.9 mol%Ni in cell culture media.

Table 5.1 Corrosion parameter of Ti-50mol%Ni

	OCP (mV)	$E_{corr}$ (mV)	$I_{corr}$ (nA·cm <sup>2</sup> )	$I_{ss}$ (nA·cm <sup>2</sup> )	$E_{bd}$ (V)
BHPT	-73.92	-139.84	71.23	1638.24	1.07
N=0.25	22.08	68.95	50.76	1275.58	1.14
N=0.5	40.79	48.63	5.16	418.96	0.95
N=1	-8.59	-40.69	21.31	518.99	1.03
N=5	-26.38	-36.15	13.84	927.55	1.04
N=10	83.42	-29.99	46.07	1593.43	1.00

Table 5.2 Corrosion parameter of Ti-50.9mol%Ni

	OCP (mV)	$E_{corr}$ (mV)	$I_{corr}$ (nA·cm <sup>2</sup> )	$I_{ss}$ (nA·cm <sup>2</sup> )	$E_{bd}$ (V)
BHPT	-125.75	-199.77	160.43	2055.47	0.96
N=0.25	30.512	29.25	201.67	1246.78	0.96
N=0.5	-31.96	-36.72	8.922	1488.95	1.11
N=1	-40.93	-42.23	50.64	1482.22	1.01
N=5	-6.32	-6.52	74.93	1092.39	1.03
N=10	-23.57	-23.00	16.77	1351.73	1.02

## 5.4 Discussions

Nanocrystallization and amorphization induced by severe plastic deformation is shown to change the corrosion behavior of TiNi alloys. Investigation on open circuit potential reveals HPT deformation shifts the OCP of TiNi samples to more positive value in comparison to those of BHPT samples in both TiNi alloys. The shift towards more noble potential indicates the higher protectiveness of the passive film formed prior to immersion in the cell culture medium. The OCP for HPT samples also stabilized immediately or increase to higher potential signaling the stability of the passive film.

The results of potentiodynamic test revealed that the samples after HPT deformation have more stable and protective oxide film on the surface. The higher passive current density of BHPT samples in both alloys than those of HPT-deformed samples indicates the defective nature of the passive film[4]. Slight incline in the beginning of the passive range in the HPT deformed samples indicates the passive film still continues to increase before finally reaching stable state. This behavior agrees with the XPS observation as discussed in Section 4.4.

Passive film formed on TiNi alloys serves as strong barriers between TiNi alloys and the physiological environment. As discussed in Chapter 4, the passive film formed on TiNi alloys is comprised of  $\text{TiO}_2$ ,  $\text{NiO}$  and  $\text{Ni(OH)}_2$ . However, after subjected to HPT deformation, the amount and composition of the passive films varies depending on the HPT rotations. It was concluded from the XPS observation in Section 4.4 that the thickness of the passive layer in HPT deformed samples equal or higher than that of BHPT sample. However, thicker passive film has been shown not necessarily advantageous [5]. Thick passive film, such as formed during oxidation process, might deteriorate the mechanical properties of the bulk layer. Thick oxide layers also susceptible to cracking [6]. The defective passive film allows for the elemental Ni to diffuse through and released to the surrounding environment.

Although in general thicker passive films improve the corrosion resistance, the thickness is not the only factor influencing corrosion behavior of an alloy. Other factors, such as oxide structure, adherence to the substrate, presence of defect, and chemical composition, also play role in determining the corrosion rate. The uniformity and stability of the oxide is most important to protect the materials from corrosion [1]. Few works have been done in the investigation of the effect of nanocrystallization and amorphization on the corrosion resistance of TiNi. Amorphous TiNi alloys prepared by melt spinning also shows improvement in corrosion resistance. Mathur et. al. attributed the corrosion resistance of amorphous TiNi alloys are due to the different oxide species on the surface oxide [7]. Recently, the effect of SPD process on the corrosion behavior of TiNi was also examined. Early work by Trepanier et. al. has shown that straining up to 10% did not affect the corrosion resistance of TiNi alloys [8]. Tsuchiya et. al. reported

that corrosion current density of Ti-50.9mol%Ni in 1M HNO<sub>3</sub> decreases after shot-peened with Fe-C at 0.6 MPa even though the surface area increases due to surface roughness [9]. Electrochemical investigation using physiological fluid on nanocrystalline TiNi alloys also has been reported. Amorphous and nanocrystalline Ti-50.2mol%Ni fabricated via HPT deformation process has been subjected to corrosion test in artificial saliva and Hank's solution by Nie et. al. [10]. The amorphous and nanocrystalline TiNi shows better pitting resistance in comparison to microcrystalline TiNi. SEM images of the surface, as shown in Fig. 5.4, revealed the pitting damages in TiNi were less severe after subjected to HPT. Another works by Hu et.al. also shows corrosion resistance of Ti-50.8mol%Ni in 0.9% NaCl was enhanced after SMAT process due to readily protective formed passive film on the surface [11]. The enhanced corrosion resistance on other SPD-deformed passive alloys such as titanium and stainless steel also has been reported. Ultrafine grained Ti produced by ECAP had better corrosion resistance than coarse grain Ti in HCl and H<sub>2</sub>SO<sub>4</sub> solutions [12]. Nanocrystalline 302 stainless steel prepared by ECAP also shows better corrosion resistance due to improvement in compactness and stability of the passive films [13].

Despite the enhanced corrosion resistance of nanocrystalline and amorphous TiNi in various mediums, it is important to point out that the cell culture medium as used in this study is more complex as it contains not only inorganic species but also organic giant molecules such as serum proteins. Hang et. al. compared the corrosion behavior of TiNi in PBS and FBS. It was found that the presence of FBS accelerates the corrosion of TiNi alloy as the passive film formed on TiNi exposed to FBS was thinner and porous. Adsorption of proteins and organic compounds such as amino acids on the surface of TiNi might contributes to this behavior [14]. Hiromoto et. al also found that the average pitting potentials of 316L steel decreases when subjected to MEM+FBS as the adsorbed biomolecules prevents the diffusion of dissolved oxygen at the interface on 316L steel [15]. The addition of L929 cells to the corrosion medium further decreased the corrosion resistance of 316L steel [15]. However, to this date, no works has been done in comparing the effect of HPT deformation to the corrosion behavior of TiNi or other metallic biomaterials in the EMEM+FBS as demonstrated in this study.

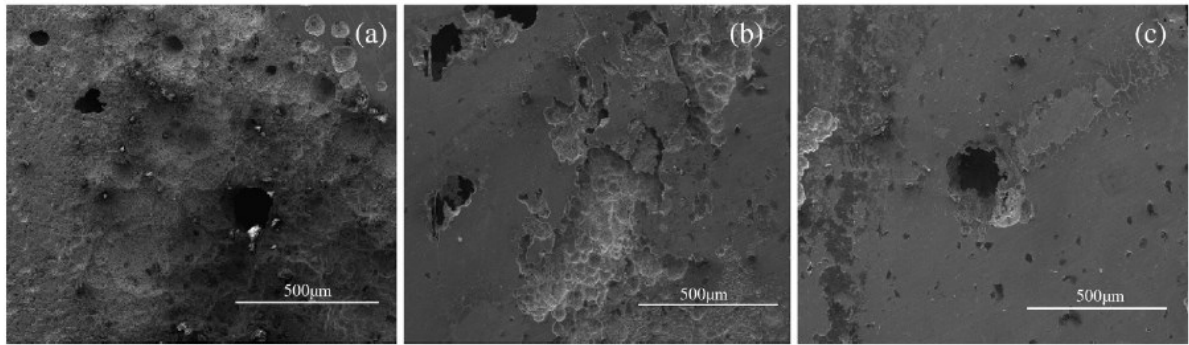


Fig. 5.4 Surface morphologies of (a) microcystalline (b) amorphous and (c) nanocrystalline Ti-50.2mol%Ni after corrosion in Hank's solution [10].

The structural changes induced in TiNi alloys after HPT deformation allow the formation of more uniform passive film. The stability of the passive film depends on the structural properties such as film compactness and defect density [16]. Improved corrosion resistance of TiNi as observed in this study may be attributed to the nanocrystallization and amorphization induced by HPT deformation. Enhanced corrosion resistance of nanostructured alloys is attributed to the high density of grain boundaries and defects that provides fast diffusion paths of oxygen, titanium and nickel atoms [17]. As the corrosion activation occurs primarily at the surface defects, such as grain boundaries and dislocations, small grain sizes promote uniform Ni and Ti distribution, which facilitates rapid formation of oxide layer. High densities of dislocation and grain boundary cause the drive to achieve energy equilibrium state through fast passivation and homogeneous corrosion[12]. The higher energies stored in the non-equilibrium grain boundaries and high internal stress generated during HPT resulting in formation of uniform passive film [18]. Dislocations created during deformation reduced the energy barrier for electrochemical reactions. Nanocrystallization was found to change the surface condition of the alloys, but also effectively increase the activity of metallic atoms and accelerate the corrosion rate [19]. The activation barrier to dissolution from nanocrystalline Ni surfaces is higher compared to bulk Ni, thereby resulting in improved corrosion resistance for nanostructured surfaces compared to bulk surfaces. This may be related to the observation that nanocrystalline Ni showed lower tendency for localized grain boundary corrosion while in polycrystalline Ni, this can result in failures [4].

## **5.5 Conclusion**

The effect of HPT deformation on electrochemical behavior of TiNi alloys was compared in this chapter. The shift in OCP to the more positive potential in HPT deformed samples indicates the ennoblement of the samples surface upon immersion in cell culture medium. The passive current density of the HPT deformed samples also were found to be lower in comparison to the BHPT sample in both alloys, indicating the passive film formed is more protective. This study concluded the beneficial effects of HPT deformation on the corrosion resistance of TiNi alloys in the cell culture medium due to formation of more stable and protective passive film on the TiNi alloys after HPT deformation.

## 5.6 Reference

- [1] Duerig T, Pelton A, Stöckel D. An overview of nitinol medical applications. *Mater. Sci. Eng. A* 1999;273:149–60.
- [2] Vojtěch D, Fojt J, Joska L, Novák P. Surface treatment of NiTi shape memory alloy and its influence on corrosion behavior. *Surf. Coat. Tech.* 2010;204:3895–901.
- [3] Pourbaix M. Electrochemical corrosion of metallic biomaterials. *Biomaterials* 1984;5:122–34.
- [4] Mishra R, Balasubramaniam R. Effect of nanocrystalline grain size on the electrochemical and corrosion behavior of nickel. *Corros. Sci.* 2004;46:3019–29.
- [5] Trepanier C, Tabrizian M, Yahia L. Effect of modification of oxide layer on NiTi stent corrosion resistance. *Journal of Biomedical* 1998.
- [6] Shabalovskaya S, Anderegg J, Van Humbeeck J. Critical overview of Nitinol surfaces and their modifications for medical applications. *Acta Biomater.* 2008;4:447–67.
- [7] Mathur S, Vyas R, Sachdev K, Sharma SK. XPS characterization of corrosion films formed on the crystalline, amorphous and nanocrystalline states of the alloy Ti60Ni40. *Journal of Non-Crystalline Solids* 2011;357:1632–5.
- [8] Trepanier C, Pelton AR. Effect of strain on the corrosion resistance of nitinol and stainless steel in simulated physiological environment. *Medical Device Materials: Proceedings From the Materials & Processes for Medical Devices Conference 2003*, 8-10 September 2003, Anaheim, California 2004:176.
- [9] Tsuchiya K, Cao QF, Hosokawa A, Katahira M, Todaka Y, Umemoto M. Nanostructured Shape Memory Alloys for Biomedical Applications. *Mater. Sci. Forum* 2007;539–543:505–10.
- [10] Nie FL, Zheng YF, Cheng Y, Wei SC, Valiev RZ. In vitro corrosion and cytotoxicity on microcrystalline, nanocrystalline and amorphous NiTi alloy fabricated by high pressure torsion. *Mater. Lett.* 2010;64:983–6.
- [11] Hu T, Xin YC, Wu SL, Chu CL, Lu J, Guan L, Chen HM, Hung TF, Yeung KWK, Chu PK, Yeung KWK. Corrosion behavior on orthopedic NiTi alloy with nanocrystalline/amorphous surface. *Mater. Chem. Phys.* 2011;126:102–7.
- [12] Balyanov A, Kutnyakova J, Amirkhanova NA. Corrosion resistance of ultra fine-grained Ti. *Scripta Mater.* 2004.
- [13] Zheng ZJ, Gao Y, Gui Y, Zhu M. Corrosion behaviour of nanocrystalline 304 stainless steel prepared by equal channel angular pressing. *Corros. Sci.* 2012.
- [14] Hang R, Ma S, Ji V, Chu PK. Corrosion behavior of NiTi alloy in fetal bovine serum. *Electrochim. Acta* 2010;55:5551–60.
- [15] Hiromoto S, Hanawa T. Electrochemical properties of 316L stainless steel with culturing L929 fibroblasts. *Journal of the Royal Society Interface* 2005;3:495–505.
- [16] Wang Y, Jiang SL, Zheng YG, Ke W, Sun WH, Wang JQ. Electrochemical behaviour of Fe-based metallic glasses in acidic and neutral solutions. *Corros. Sci.* 2012;63:159–73.
- [17] Saji VS, Thomas J. Nanomaterials for corrosion control. *Curr Sci* 2007;92:51–5.
- [18] Dolega Ł, Adamczyk-Cieślak B, Mizera J, Kurzydłowski KJ. Corrosion resistance of model ultrafine-grained Al–Li alloys produced by severe plastic deformation. *J Mater Sci* 2011;47:3026–33.
- [19] Liu L, Li Y, Wang FH. Electrochemical corrosion behavior of nanocrystalline materials-a review. *J. Mater. Process. Tech.* 2010;26:1–14.



## Chapter 6 Conclusions

This work presents the effect of high pressure torsion (HPT) deformation on the phase, mechanical properties and surface properties of two different TiNi alloys. The biocompatibility of the TiNi alloys before and after HPT deformation was also analyzed. In addition, the electrochemical studies of the TiNi alloys in cell culture medium were also investigated. The main findings are summarized as follows:

1. In this study, bulk nanostructured of TiNi alloys with two different compositions have been produced by using HPT, a severe plastic deformation process. The alloys were subjected to various degree of deformation by varying the number of HPT rotations. The results from X-ray diffraction (XRD) shows that increasing strain imposed on the TiNi alloys leads to the phase and microstructural change. Grain refinement and amorphization of the TiNi alloys observed from the XRD patterns is attributed to the increase in the dislocation density. Microhardness characterization shows the HPT deformation increase the hardness of TiNi alloys with the number of rotation. Furthermore, an evolution towards hardness homogeneity with increasing numbers of turns in HPT processing was also observed.
2. Biocompatibility test shows the microstructural changes due to HPT deformation did not induced any cytotoxic effect to the L929 cells. The cell growth and protein adsorption were also improved especially on the low rotation samples. Most importantly, HPT deformation was shown to be beneficial as it was able to suppress the Ni ion released into cell culture media.
3. The microstructural changes due to HPT influence the surface chemistry of TiNi alloys as observed by X-ray photoelectron spectroscopy (XPS). High dislocation density due to HPT deformation was found to modify the passive film properties of TiNi alloys. Metallic Ni enrichment on the surface was eliminated and the passive film thickness increased after the HPT deformation, suggesting the changes in the passive film formation kinetic.

## Chapter 6

4. Electrochemical studies on the TiNi in the cell culture environment further helps us to understand the effect of HPT deformation on the Ni ion release and passive film formation phenomenon in the TiNi alloys. HPT deformed TiNi alloys were found to have better corrosion resistance as the passive films formed on the deformed samples were found to be more stable and protective.